Morphologies of Semiflexible Polymers in Bulk and Spherical Confinement

Der Fakultät für Physik und Geowissenschaften
der Universität Leipzig genehmigte
DISSERTATION
zur Erlangung des akademischen Grades
doctor rerum naturalium
(Dr. rer. nat.)

vorgelegt
von
Martin Marenz

1. Gutachter: Prof. Dr. Wolfhard Janke
2. Gutachter: PD. Dr. Peter Virnau
Tag der Verleihung: 18.06.2018

Contents

List of Figures

List of Tables

1. Foreword

I have split my dissertation into two separated parts, one concerning the implementation of the Metropolis Monte Carlo algorithms and the other centered around the actual simulations of coarse-grained polymers. The usual approach would be to present the simulation techniques in the methods section of the dissertation. However, a colleague of mine, Johannes Zierenberg, and me have implemented different Monte Carlo algorithms in a generic and reusable framework which is an important part of this thesis on its own. A substantial part of my work has gone into the design and implementation of the framework itself. The framework should not only satisfy the needs of our work, instead we tried to design it to be useful for a broad spectrum of applications. Therefore, I want to present the framework in its own part. Nevertheless, the focus in this technical part lies on the algorithm used for the results presented int the result sections. The simulations and the development of the framework are indeed not separable, both were created and improved continuously at the same time.

Part I.

Morphology of a Semiflexible Polymer

2. Introduction

Synthetic polymers are one basic building block of the industrial production of our modern society. Most of the things we use in our everyday life consists of plastic, which itself is just a kind of polymer. It starts by trivial things like plastic bags, over cases for smartphones, to such elementary things like buttons. Almost every button is made of plastic, the one we push to switch on the light when the day starts, the one we push to start the PC when the office-work begins, or nowadays even the button which switches on the engine of a car. On the other side, the nature uses different kind of polymers as its own basic building blocks. Biopolymers are one of the materials the life is build up upon: fibres, proteins, and first of all DNA, the carrier of the building plan of the life itself, all necessary for every type of life as we know it.

The knowledge of what polymers are, and therefore the start of their modern scientific investigation, is almost 100 years old. The fundamental work was done by Staudinger in 1920 [100] who showed that polymers are long chains consisting of repeating monomers connected by covalent bonds. In the first half of the last century people like Werner Kuhn, Paul Flory, or Walter H. Stockmayer laid the foundation of the theoretical polymer physics. In the second half of the 20th century, others like Rouse, Zimm, de Gennes, Edwards, or Khokhlov extended our knowledge vastly, so that nowadays we have a good theoretical description of what a polymer is and how it behaves.

Today, state-of-the-art experiments can give a very detailed insight in the structure and behavior of real polymers. Employing scanning tunneling microscopy it is even possible to measure polymers consisting of down two 20 monomers [33]. However, this detailed experimental knowledge of a polymer, with all its chemical details, is not easily treatable from a theoretical point of view. The involved microscopic details are hard to treat mathematically and may mask the sight on the generic aspects of some problems. Although it is possible to simulate such polymers in very detail, even modern computers are not capable to investigate realistic microscopic models over a large parameter range, time scale, or length scale. For this purpose it is necessary to go a step back and use so called coarse-grained models which intentionally not incorporate all chemical details, but can provide a fundamental insight into the structural behavior of polymers.

Coarse-grained models featuring self-avoidance and attraction lead to the formulation of Θ-polymers exhibiting at least a collapse transition. There exist many varying studies of flexible Θ-polymers. For instance, already lattice polymers, modeled as self-avoiding walks with a nearest-neighbor attraction [9, 85, 113] exhibit solid, collapsed, and frozen phases. Going away from the lattice by using off-lattice models, such as the bead-stick or bead-spring polymer, one can study various aspects, such as the phase diagram of flexible polymers [10, 96, 98] or use them as toy models for protein folding [50, 102]. With the help of even simpler models, such as the extraordinary successful wormlike-chain (WLC) model [65], one can investigate the influence of stiffness on the structure of polymers. The WLC has very successfully proven to be able to describe DNA or other complex biopolymers on a coarse-grained level.

However, studies combining stiffness and self-attraction/self-repulsion are less frequent. Some recent studies investigate the relationship between intra-polymer self-interaction and bending stiffness along the polymer backbone, either by mean-field calculations [25], with lattice polymers [38, 47, 51], or even more complex models like the tube-like polymer model [74, 114]. The model of choice of this thesis is the so called bead-stick model. Within the bead-stick model the monomers are treated as single particles (beads) connected with fixed length bonds (sticks). A very similar model is the bead-spring model, where the fixed bonds are replaced by elastic springs. Both models were recently used, e.g., to determine the ground-state structure [44], analyze the low-density behavior of polymer aggregation [122], or to construct the stiffness dependent phase diagram of a single semiflexible polymer [79, 97].

Although the influence of the stiffness on the structure of a polymer is the main topic of this thesis, its origin lies somewhere else. It is possible to incorporate the details of all 21 amino acids into coarse-grained protein models. These kinds of models can be used to investigate various problems centered around the behavior of proteins. One of such problems is the influence of a confinement on the stability of proteins. Works like [45, 80, 90, 91] show that a three-dimensional closed confinement may stabilize the structure of proteins. This thesis originated by trying to understand this behavior on a generic level. Employing the bead-stick model, I tried to mimic the behavior observed for proteins. However, I realised soon that one factor to understand this effect lies in the stiffness of the polymer. To understand how confinement influences a semiflexible bead-stick polymer, one first have to understand how stiffness influences its bulk behavior. So this thesis starts by investigating the phase-diagram of the bead-stick polymer as a generic model for a semiflexible homopolymer in the following way:

- The second chapter gives a very brief introduction into some basic concepts of polymer physics. It introduces the wormlike-chain model and some fundamental measurements to characterize polymers.

- In the third chapter the bead-stick model is explained in quite detail, as well as the definitions of all measured observables and analysis methods used to investigate the structural behavior of the polymer.

- The fourth chapter gives an overview of how stiffness influences the phase-diagram of a single free homopolymer. The results of the simulation of the bead-stick model over the complete range of stiffnesses are presented. Specifically, it shows that a new kind of pseudo-phase emerges: for intermediate stiffness and low temperatures I found thermodynamically stable knotted conformations.

- The fifths chapter goes back to where this thesis originated. It concerns with the stabilizing and destabilizing effects a spherical confinement has on the pseudophases of a semiflexible bead-stick homopolymer.

3. Basic Concepts in Polymer Physics

First a brief introduction into the basic concepts of polymer physics in the thermodynamic equilibrium is given such that the later results can be placed in the appropriate context. A detailed description of all these aspects can be found in standard literature [23, 88].

3.1. Ideal Chains

The most simple model for a polymer is probably the random walk (RW), respectively the freely-jointed chain (FJC), where the term “random walk” is often used if one considers it on a lattice and “freely-jointed” chain in the case of the free space. The polymer consists of N steps of identically step length b. Therefore, the position $\vec{r}_n$ after each step is treated as monomer and the vector between two steps $\vec{b}_n = \vec{r}_{n+1} - \vec{r}_n$ as the bond connecting the nth and $(n+1)$th monomer. Since there is no interaction between the individual monomers or bonds, the monomer positions $\vec{r}_n$ are completely uncorrelated $\left(\left\langle \vec{b}_n \right\rangle = 0\right)$, thus the statistical properties of the RW/FJC can be easily calculated. For example, the average end-to-end distance vanishes in the statistical average:

$$\langle R_{ee} \rangle = \left\langle \sum_{n=1}^{N} \vec{b}_n \right\rangle = 0. \tag{3.1}$$

However, the squared end-to-end distances scales with the number of monomers N:

$$\begin{aligned} \left\langle R_{ee}^2 \right\rangle &= \left\langle \sum_{m=1}^{N-1} \sum_{n=1}^{N-1} \vec{b}_m \vec{b}_n \right\rangle = \sum_{m=1}^{N} \sum_{n=1}^{N-1} \left\langle \vec{b}_m \vec{b}_n \right\rangle & (3.2) \\ &= \sum_{m=1}^{N} \sum_{n=1}^{N-1} \delta_{nm} b^2 = N b^2. & (3.3) \end{aligned}$$

For all polymer models with uncorrelated bonds the size of the polymer is considered to scale with the squared end-to-end distance, hence the size of the polymer scales with the number of monomers as

$$\left\langle R_{ee}^2 \right\rangle^{\frac{1}{2}} \propto N^{\nu} \quad \text{with } \nu = \frac{1}{2}. \tag{3.4}$$

ν is called a critical exponent and differs from $1/2$ as soon as different physical properties introduce long range correlations between the bonds of the polymers.

Another measure for the size of the polymer is the squared radius of gyration

$$\left\langle R_g^2 \right\rangle = \left\langle \frac{1}{N+1} \sum_{n=1}^{N} (\vec{r}_n - r_{\text{mean}}) \right\rangle, \tag{3.5}$$

with $r_{\text{mean}} = \frac{1}{N+1} \sum_{n=1}^{N} \vec{r}_n$ being the mean position of all monomers. The squared radius of gyration is a measurement of the mean size of the polymer. It scales with N as

$$\begin{aligned} \left\langle R_g^2 \right\rangle &= \left\langle \frac{1}{N+1} \sum_{n=1}^{N} (\vec{r}_n - r_{\text{mean}}) \right\rangle & (3.6) \\ &= \frac{1}{2(N+1)^2} \sum_{n=1}^{N} \sum_{m=1}^{N} \left\langle (\vec{r}_n - \vec{r}_m)^2 \right\rangle . & (3.7) \end{aligned}$$

Since $\langle(\vec{r}_n \vec{r}_m)\rangle$ is the squared end-to-end distance from n to m (3.2), the squared radius of gyration can be written as

$$\begin{aligned} \left\langle R_g^2 \right\rangle &= \frac{1}{2(N+1)^2} \sum_{n=1}^{N} \sum_{m=1}^{N} b^2 |n-m| & (3.8) \\ &= \frac{1}{N+1} \sum_{k=1}^{N} (1 - \frac{k}{N}) k & (3.9) \\ &= \frac{b^2}{6} \frac{N^2-1}{N} \overset{N>>1}{=} \frac{Nb^2}{6}. & (3.10) \end{aligned}$$

Thus, the squared radius of gyration can be rewritten in terms of the squared end-to-end distance

$$\left\langle R_g^2 \right\rangle = \frac{\langle R_{ee}^2 \rangle}{6}. \tag{3.11}$$

For a typical polymer the correlation between bond vectors is not zero $\left\langle \vec{b}_m \vec{b}_n \right\rangle \neq 0$. However, the exponent $\nu = 1/2$ is preserved as long as there are no correlations for distant bond vectors:

$$\lim_{|n-m|>>1} \left\langle \vec{b}_m \vec{b}_n \right\rangle = 0. \tag{3.12}$$

From this assumption the equivalent freely-jointed chain can be constructed by combining several monomers to an effective repeating unit N_k with freely jointed effective bonds of length l_k. The squared end-to-end distance scales now as

$$\left\langle R_{ee}^2 \right\rangle = N_k l_k^2. \tag{3.13}$$

l_k is called *Kuhn length* and measures the size of the segment length which is effectively statistical uncorrelated. This is only valid as long as $N >> N_k$. To describe the stiffness of a polymer often the correlation length ξ instead of the Kuhn length is given. The correlation length measures the distance over which the tangent vectors get statistically uncorrelated. For ideal chains the correlation length is half the Kuhn length $\xi = l_k/2$.

3.1.1. Worm-Like Chain Model

There exists many more ideal chain models which do not incorporate self interactions between monomers, but fur the purpose of this thesis I will only introduce one more – the worm-like chain model [65]. It explicitly describes the effect of bending stiffness, which will play an important role later in this thesis. The worm-like chain, also known as Kratky-Porod model, is especially useful to describe stiffer polymers. The original version of the worm-like chain model is discrete and defined by the following Hamiltonian

$$\mathcal{H} = \sum_k \kappa \left(1 - \cos\theta_k\right). \tag{3.14}$$

Often it is more convenient to go to a continuum representation for which some mathematical calculations are easier to obtain. The continuum worm-like chain is a model for a polymer with non-vanishing persistence length and a constant contour length L. Its Hamiltonian is given by

$$\mathcal{H} = \frac{\kappa}{2}\int_0^L ds \left(\frac{\partial^2 R(s)}{\partial s^2}\right)^2, \tag{3.15}$$

with $R(s)$ being the curve describing the polymer and κ the bending stiffness. The squared end-to-end distance can be calculated via

$$R_{ee}^2 = 2l_pL - 2l_p^2\left(1 - \exp\left(-\frac{R_{\max}}{l_p}\right)\right). \tag{3.16}$$

For the limit of flexible polymers ($L >> l_p$) this gives an equivalent scaling as (3.13)

$$\left\langle R_{ee}^2 \right\rangle \approx 2l_pL = l_kL. \tag{3.17}$$

In case of a rod-like polymer ($L << l_p$) the end-to-end distance is equivalent to the contour length

$$\left\langle R_{ee}^2 \right\rangle \approx L^2. \tag{3.18}$$

As long as the polymer is so stiff that it does not self interact, or the self-interaction can be neglected, the worm-like chain model is a very good approximation and able to capture the behavior of real polymers very well. It was successfully applied to biopolymers, such as DNA, RNA, actin filaments, or microtubles.

3.2. Self-Avoidance and Attraction

Taking the self-avoidance and attraction into account, which is apparently necessary to study collapse or aggregation phenomena, the worm-like chain, as well as all other ideal chain models, cannot longer properly describe structural properties of polymers. In order to model polymers in which monomers cannot overlap each other, as forbidden by the Pauli principle, it is necessary to introduce self-avoidance as it was first done by Flory [30]. For that purpose the number of monomer-monomer contacts can be estimated by the probability that a monomer overlaps with another monomer in a mean-field approach[1]. This probability is given by the overlap volume fraction Θ^* which is the product of the monomer volume b and the number density of monomers in the volume occupied by the whole polymer N/R_{ee}^d

$$\Theta^* \approx b^d \frac{N}{R_{\mathrm{ee}}^d}. \tag{3.19}$$

Putting in the Gaussian statistics of ideal chains $\langle R_{\mathrm{ee}}^2 \rangle^{\frac{1}{2}} = bN^{\frac{1}{2}}$, this leads to the overlap volume fraction:

$$\Theta \approx b^d \frac{N}{\left(bN^{\frac{1}{2}}\right)^d} = N^{1-d/2}. \tag{3.20}$$

The number of monomer-monomer contacts is now given by the product of the number of monomers and the overlap volume fraction

$$N\Theta^* \approx N^{2-d/2}. \tag{3.21}$$

For $d > 4$, the number of contacts is small and the polymer behaves like an ideal chain without self-interaction. A rough estimate about the size of the polymer can be obtained by the Flory theory, which leads to the following total free energy:

$$F = \frac{1}{\beta}\left(\frac{3\langle R_{ee}^2\rangle}{2Nb^2} + \frac{N^2 b^d}{2\langle R_{ee}\rangle^2}\right). \tag{3.22}$$

Minimizing (3.22) with respect R_{ee} leads to

$$\langle R_{ee}\rangle^{\frac{1}{2}} \propto bN^{\nu}, \tag{3.23}$$

with $\nu = \frac{3}{d+2}$. This is exact in $d = 1$ and $d = 2$ and astonishingly close to more sophisticated methods (e.g. simulations or renormalization group calculations) in three dimensions.

Taking equation (3.22) and assigning each monomer-monomer contact

---

[1] The derivation given here follows Reference [88, pp. 97].

$\left(N^2 b^d / \left(2|R_{ee}|^2\right)\right)$ a contact energy ϵ, the free energy can be written as:

$$\beta F = \left(\frac{3\left\langle R_{ee}^2 \right\rangle}{2Nb^2} + (1+\epsilon\beta)\frac{N^2 b^d}{2\left\langle R_{ee}\right\rangle^2} \right). \tag{3.24}$$

If the factor $(1+\epsilon\beta)$ is negative, the short-ranged monomer-monomer attraction dominates and describe the bad solvent case, if $(1+\epsilon\beta)$ is larger than 0 it corresponds to repulsive monomers and the good solvent case. Most interestingly is the case where $(1+\beta\epsilon)=0$, the Θ-solvent case. At the Θ-point the repulsion and attraction are balanced and the scaling of the free polymer is retained.

Adding an additional attractive potential to each monomer leads to the so called ISAW (interacting self-avoiding walk). This leads to globule conformations below the Θ-point and very dense structures and ordered states close to the ground state. Without the constraint of the bonds between the monomers, a behavior similar to Lennard-Jones gases would emerge, with crystal-like conformations.

4. Model and Analysis Methods

This chapter begins with a brief motivation of the used polymer model followed by a detailed description of the model and the observables used to investigate its phase diagram in thermal equilibrium.

Studies of the competition between bending stiffness and self-interaction are relatively rare. In Reference [25] a mean-field calculation of a lattice model which incorporates bending stiffness gives a rough overview of the phase diagram in dependence of the temperature and the bending stiffness. There exists also works simulating semiflexible off-lattice models. For example, in [79] a simple off-lattice model using a harmonic bending potential is used to sample polymers over a range of bending stiffnesses. Noguchi et al. show that at high bending stiffness the polymer undergoes a first-order transition from a swollen into a toroidal phase. In [114, 115] similar analysis are done for a tube-like polymer. Within the model given there the bending stiffness is not modeled via an energetic potential, instead the polymer has a finite thickness which induces an effective stiffness. The phase diagram of this model exhibit several phases with differently structured conformations, such as rod-like, circular, sheet-like and helical polymers. A detailed analysis of the phase diagram of a bead-spring model is done in [97]. The Hamiltonian of the model used there is similar to the one predominantly used in this thesis. Nevertheless, there is a key difference which will lead to a major change in the overall picture. Seaton and co-workers used a finitely extensible nonlinear elastic (FENE) potential to model the covalent bonds of the polymer. The equilibrium elongation of that FENE potential r_b has the same distance as the minimum of the Lenard-Jones potential $r_{\min}$ which is used to model the interaction between non-adjacent monomers. The resulting phase diagram in Reference [97] spans the complete range of semiflexible polymers, from flexible to very stiff. In the flexible case it resembles the swollen (high temperature), the coiled and the frozen (low temperature) phase. The polymer conformations in the frozen phase are in most cases best described by Mackay or anti-Mackay patterns, which are already investigated in quite detail in [96].

4.1. The Bead-Stick Model

The majority of the simulations for this thesis are done with the so called bead-stick model. Originally, it was used to model a heteropolymer with two types of monomers as a toy model for protein folding in two dimensions [101, 102]. Later it was extended to three-dimensional space [46, 50, 56]. This model is simple enough to systematically study generic aspects, but has the advantage that is does not suffer from strong

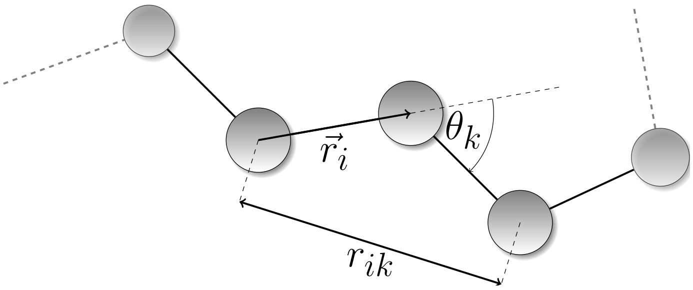

Figure 4.1.: Schematic description of the bead-stick polymer. $\vec{r_i}$ is the bond vector connecting the ith and $i+1$th monomer, r_{ik} is the distance between the ith and kth monomer.

discretization artifacts as lattice models do. The dependence on the sequence of the two different constituents was one of the major issues in former works. Here I want to concentrate on another aspect of the model, therefore the hydrophobicity between the monomers is neglected, instead it is considered as a generic model for a homopolymer with N identical monomers and an adjustable bending stiffness.

The adjacent monomers of the linear polymer are connected with bonds of fixed length. The bond vector of the ith and $(i+1)$th monomer is denoted by $\vec{r_i}$ with length $b = |\vec{r_i}|$. If not otherwise given, b is set to one and define the length scale of the polymer. Neighboring bonds form the bonding angle $\theta_i = \vec{r_i} \cdot \vec{r}_{i+1}$ and the distance between the ith and kth monomer is given by r_{ik}.

The self-avoidance and attraction of each monomer is provided by a Lennard-Jones potential of the common 12-6 form:

$$E_{\mathrm{LJ}} = 4\epsilon \sum_{i>k}^{N} \left(\frac{\sigma^{12}}{r_{ik}^{12}} - \frac{\sigma^{6}}{r_{ik}^{6}} \right), \tag{4.1}$$

The parameters ϵ and σ are set to one for the rest of this work, i.e. energies are measured in terms of ϵ and distances in units of σ. The bending stiffness is modeled via a cosine potential already known from the discrete worm-like chain model (3.19) and defined by:

$$E_{\mathrm{bend}} = \kappa \sum_{k}^{N-2} \left[1 - \cos(\theta_k)\right]. \tag{4.2}$$

The complete Hamiltonian is now given by:

$$H \equiv E = E_{\mathrm{LJ}} + E_{\mathrm{bend}}, \tag{4.3}$$

in which κ defines the ratio of the Lennard-Jones potential and the bending potential. Note that κ does not translate directly into the correlation length as it does in the case of the discrete worm-like chain model. The presence of the Lennard-Jones potential prevents an analytical solution for the correlation length.

4.2. Canonical Analysis

To describe the thermodynamic equilibrium behavior of the investigated systems, different observables $\mathcal{O}$ are measured. An observable is a projection of the high-dimensional state space with its large degree of freedom ($3N - 5$ for the bead-stick polymer) to a much lower dimension - in most cases one dimension. Usually, one distinguishes the true expectation value of an observable $\langle \mathcal{O} \rangle$ and its measurement in a Monte Carlo simulation $\overline{\langle \mathcal{O} \rangle}$. For the rest of the thesis this difference is neglected, since it has no influence on the derivations presented here.

The observables used in this thesis can be divided in three classes. Either they measure energetic quantities, they describe the size and the shape of the polymer, or they consider the topology of the polymer conformation itself. The most interesting regions in the pseudo-phase diagram are probably the pseudo-phase transitions, where the polymer undergoes a substantial conformational change. The pseudo-phase transitions are the thermal most active regions in the pseudo-phase diagram and are indicated by a local peak in the thermal derivative of an observable:

$$\frac{d}{dT} \langle \mathcal{O} \rangle = \frac{1}{T^2} \left(\langle \mathcal{O} E \rangle - \langle \mathcal{O} \rangle \langle E \rangle \right), \tag{4.4}$$

where E is the total energy. Peaks in (4.4) mark the location of pseudo-phase transition which should not be identified with phase transitions in the thermodynamic limit due to the finite system size. A short explanation of this difference is given in the following section.

4.2.1. Pseudo-Phase Transitions

The thermodynamic limit is the formal limit for a statistical system where the number of particles N and the volume V goes to infinity, while the density is fixed:

$$N \to \infty, \quad V \to \infty, \quad \frac{N}{V} = \text{const.} \tag{4.5}$$

A "true" thermodynamic phase transition only exists in this thermodynamic limit. Due to the finite length N of the polymer, the temperatures of the transitions for a fixed N depends on the observable it is derived from, thus, these finite-size transitions are smeared out and usually called pseudo-phase transitions. For a pseudo-phase transition which persists in the thermodynamic limit it is possible to obtain values for the infinite system by a finite-size scaling analysis. For different observables $T_c(N)$ approaches the true critical temperature $T_c^\infty \equiv T_c$ independently of the used observable. It is important to note that not all transitions persist in the thermodynamic limit. Nevertheless, even if the transition vanishes in the thermodynamic limit, it still determines the behavior of mesoscopic systems and should be considered to understand the behavior of finite polymers. Especially, nowadays it is important to understand the behavior of small and mesoscopic systems far away from the thermodynamic limit, since the detection and preparation of single polymers has made quite an impressive progress and polymers down to a length of 20 monomers are traceable [32, 33].

4.2.2. Energetic Observables

The mean total energy $\langle E \rangle$ can be divided into two parts, the mean bending energy $\langle E_{\mathrm{bend}} \rangle$ and the mean Lennard-Jones energy $\langle E_{\mathrm{LJ}} \rangle$. It is worthwhile to consider both separately, since for some pseudo-phase transition one maybe more useful than the other. Especially, if $\frac{d}{dT} \langle E_{\mathrm{bend}} \rangle \approx -\frac{d}{dT} \langle E_{\mathrm{LJ}} \rangle$ the heat capacity $C_v = \frac{d}{dT} \langle E \rangle$ will not provide signals considerably larger than the statistical noise to identify and investigate pseudo-phase transitions, but the thermal derivation of the two sub-energies may give an insight in such a transition.

4.2.3. Geometrical Observables

To measure the size and the shape of the polymer several observables are considered. The squared end-to-end distance (3.2) and the squared radius of gyration (3.5) usually give both a good measure of the average size of the polymer and hence their thermal derivations $\frac{d}{dT} \langle R_{ee}^2 \rangle$ and $\frac{d}{dT} \left\langle R_g^2 \right\rangle$ are suitable to search for pseudo-phase transition where the overall size of the polymer changes. However, for semiflexible polymers the squared end-to-end distance may not scale with the size of the polymer in all pseudo-phases. For highly structured conformations, for example bent, hairpin or toroidal conformations, both termini of the polymer may be located very close to each other, and thus R_{ee}^2 does not depend on the size of the polymer at all. Nevertheless, the thermal derivative of the squared end-to-end distance will signal transitions into these pseudo-phases since the relative position of the two termini drastically change in different pseudo-phases.

The overall shape of the polymer is best described by the complete gyration tensor $\mathcal{S}$ with

$$S_{mn} = \frac{1}{N} \sum_{i=1}^{N} \sum_{j=1}^{N} (r_m^i - r_m^j)(r_n^i - r_n^j), \tag{4.6}$$

where r_m^i is the mth component of the position vector $\vec{r}_i$ of the ith monomer. Since the gyration tensor is by definition a symmetric real 3×3 matrix, it can be diagonalized into the following form

$$\mathcal{S} = \begin{bmatrix} \lambda_1^2 & 0 & 0 \\ 0 & \lambda_2^2 & 0 \\ 0 & 0 & \lambda_3^2 \end{bmatrix}. \tag{4.7}$$

with axis chosen such the eigenvalues are in sorted order $\lambda_1 \leq \lambda_2 \leq \lambda_3$. Although it is possible to describe the shape of the polymer with these three eigenvalues, more frequently one uses combinations of these eigenvalues called shape descriptors. Namely, the relative shape anisotropy $\varkappa^2$, the asphericity b, and the acylindricity c. The relative shape anisotropy can be expressed in terms of invariants of the gyration tensor

$$\varkappa^2 = \frac{3}{2}\frac{\mathrm{Tr}(\hat{\mathcal{S}}^2)}{(\mathrm{Tr}\mathcal{S})^2} = \frac{3}{2}\frac{(\lambda_1^4+\lambda_2^4+\lambda_3^4)}{(\lambda_1^2+\lambda_2^2+\lambda_3^2)^2} - \frac{1}{2}, \tag{4.8}$$

with $\hat{\mathcal{S}}$ defined as

$$\hat{\mathcal{S}} = \mathcal{S} - \frac{1}{3}\mathbb{1}\,\mathrm{Tr}\mathcal{S}. \tag{4.9}$$

Hence, $\varkappa^2$ is by construction an invariant of the gyration tensor. The other two shape descriptors are no invariants of the gyration tensor, but can be constructed by considering $\hat{\mathcal{S}}$. Since $\hat{\mathcal{S}}$ is traceless, it can be written as

$$\hat{\mathcal{S}} = b\begin{pmatrix} -1/3 & 0 & 0 \\ 0 & -1/3 & 0 \\ 0 & 0 & 0 \end{pmatrix} + c\begin{pmatrix} -1/2 & 0 & 0 \\ 0 & -1/2 & 0 \\ 0 & 0 & 0 \end{pmatrix} \tag{4.10}$$

and thereby the asphericity b is defined by

$$b = \lambda_3^2 - \frac{1}{2}(\lambda_2^2 + \lambda_1^2) \tag{4.11}$$

and the acylindricity by

$$c = \lambda_2^2 - \lambda_3^2. \tag{4.12}$$

The relative shape anisotropy ranges from 0 to 1. It starts at 0 for a completely symmetric distribution of the monomers and reaches 1 if one direction dominates the distribution, see Figure 4.2. The acylindricity c ranges from 0 to ∞ and measures the deviation from a cylindric distribution, see Figure 4.3. The last descriptor, the asphericity parameter b, measures the deviation from spherical symmetry, see Figure 4.4. Like the three eigenvalues of the gyration tensor, all three shape descriptors describe only the shape of the polymer, which means they cannot distinguish polymer conformations of an identical shape but with a different internal structure, e.g., the shape descriptors do not signal the difference between a multiple time bent conformation and a helical conformation or between a full sphere and a spherical shell. Nevertheless, most of the conformations which a polymer forms in equilibrium are so distinctive that the shape descriptors are sufficient to identify almost all pseudo-phases.

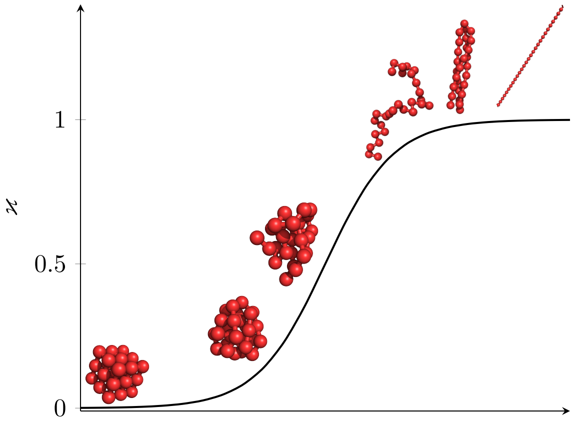

Figure 4.2.: The relative shape anisotropy $\varkappa^2$ is zero for a complete isotropic polymer, such as a spheric distribution or any tetrahedral distribution. It approaches one while the polymer unfold to a completely elongated conformation. The shown conformations are not generated by a simulation and just represent a possible conformation for a specific relative shape anisotropy.

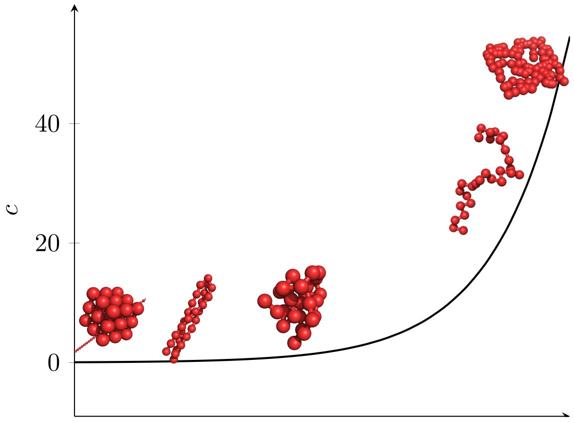

Figure 4.3.: The acylindricity c is zero if the two smaller eigenvalues are equal, for example in a sphere or a stick. It is still relative small if the polymer consists of several rod-like bundles or if the backbone forms a helix. It goes to ∞ if the smallest eigenvalue is substantial smaller than the other two, as it is in the case of a planar distribution of the monomers. Again, the shown conformations are just examples for specific acylindricity values and not obtained from real simulations.

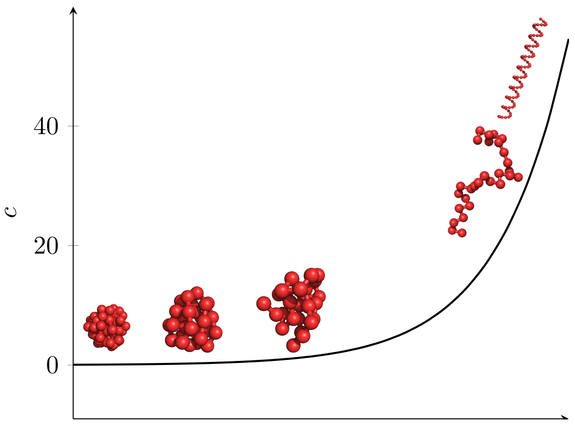

Figure 4.4.: The asphericity b describes the deviation from a spheric distribution of the monomers, it is zero for a sphere and goes to ∞ when the polymer unfolds to a stick. As for the other two shape parameters, the shown conformations are just exemplary.

4.2.4. Knot Type

Maybe the most interesting observable in this thesis is neither related to the energy nor the shape of the polymer. It is the knot type of the polygonal line formed by the backbone of the polymer. Although we know from our everyday live what a knot is, there exists a rigorous mathematical theory with a strict definition. A detailed exposition of the mathematical knot theory can be found in standard literature [59], here only a brief introduction is given.

First of all, our intuition of what a knot is does also hold in the mathematical sense; or almost holds: a mathematical knot is only defined for closed curves. Apart from that, the knot in our shoelaces or for a birthday present are real knots. In the mathematical sense a knot is usually given by the Alexander-Briggs notation [3], which assigns a symbol C_n to every closed polygonal line[1]. This symbol differs for two closed polygonal lines if both cannot be transformed into each other by applying multiple Reidemeister moves. Taking a real string as example: two closed strings have a different knot type if one cannot be transformed into the other without cutting the string apart. The first integer number C counts the minimal number of crossings the knot has on a projection onto a plane. The subscript n just distinguishes knots which have the same crossing number but a different topology, see Figure 4.5. The knot type describes a topological property of the polymer in the sense that even if the overall size and shape of the polymer does not differ between two conformations, and therefore also the typical observables do not differ, the knot type will differ if the internal structure is not identical.

To measure the knot type I will make use of a technique described in [110], which assigns a polynomial to every polymer conformation. This polynomial is called Alexan-

---

[1] Since every closed smooth curve can be interpolated by a closed polygonal line, every statement holds for closed smooth curves, too.

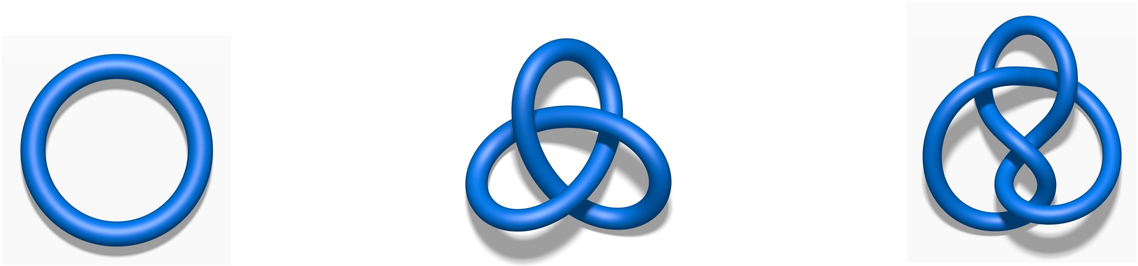

0_1 unknot

3_1 trefoil knot

4_1 figure eight knot

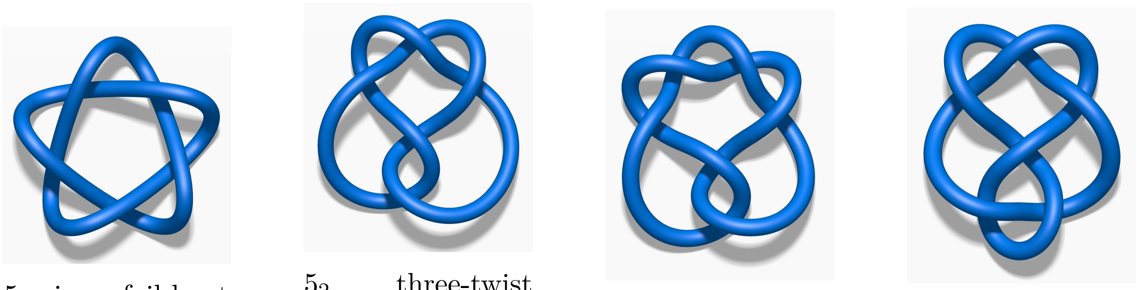

5_1 cinquefoil knot

5_2 three-twist knot

6_1 Stevedore knot

6_2 knot

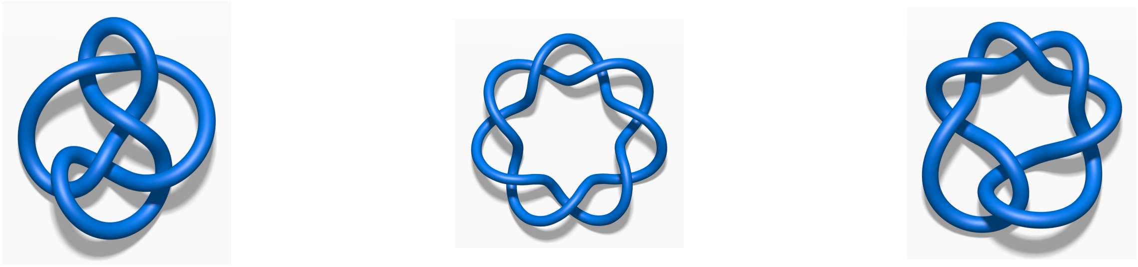

6_3 knot

7_1 knot

7_2 knot

Figure 4.5.: The ten most simple knots. For these knots the crossing number C can be obtained by eyes. (Pictures taken from Wikipedia `https://en.wikipedia.org/w/index.php?title=List_of_prime_knots&oldid=771645559`)

Table 4.1.: The Alexander polynomial and its derived quantity $\Delta_p(-1.1)$ for some simpler knots.

Knot	Alexander polynomial $\Delta(t)$	$\lvert\Delta(-1.1)\rvert$
0_1	1	1
3_1	$t + t^{-1} - 1$	9.05463
4_1	$-t - t^{-1} + 3$	25.09099
5_1	$t^2 + t^{-2} - t - t^{-1} + 1$	25.45754
5_2	$2t + 2t^{-1} - 3$	49.25488
6_1	$-2t + 5 - 2t^{-1}$	81.3276
6_2	$-t^2 + 3t - 3 + 3t^{-1} - t^{-2}$	122.406
6_3	$t^2 - 3t + 5 - 3t^{-1} + t^{-2}$	170.661
⋮	⋮	⋮
8_{19}	$t^3 - t^2 + 1 - t^{-2} + t^{-3}$	9.72667

der polynomial $\Delta(t)$ [2] and is a so called knot invariant, which means different polygonal lines with the same knot type correspond to the same Alexander polynomial. Therefore, different conformation of a polymer correspond to the same polynomial as long as the knot type of the polymer is identical. For example, the crossing number C is also a knot invariant. Unfortunately, the crossing number is not a very good one, since a substantial amount of knot types have the same crossing number. There are already two different knots having 5 crossings, see Figure 4.5 Ideally, one would search for a knot invariant which is unique and different for every knot type. Strictly speaking the Alexander polynomial is not such a unique invariant, different knot types can have the same Alexander polynomial. Nevertheless, the Alexander polynomial, in contrast to C, differs for all simpler knots and it is sufficient to distinguish all knot types found in this thesis.

Instead of using the complete Alexander polynomial, which is numerical not easily handleable, the following variant

$$\Delta_p(t) = |\Delta(t) \times \Delta(1/t)| \tag{4.13}$$

at $t = -1.1$ is calculated. $\Delta_p(-1.1)$ is a single numeric value and inherits from the Alexander polynomial the ability to distinguish different knot types, see Table 4.1. The value for t has no specific meaning as long as it is not an integer number. It just turns out that the value for $\Delta_p(t)$ increases rapidly with increasing t so that is numerical favorable to not use to large values for t.

Since an open polymer will never form a knot in the strict mathematical sense of the definition, one has to virtually close the polymer to apply the mathematical definition. The easiest knot closure would be to draw a virtual bond between both termini of the polymer which seems to be not a good idea since small changes in the conformation would lead to very different knot types, see Figure 4.6. Instead, I used two other closures which are statistically more stable and generate almost identical

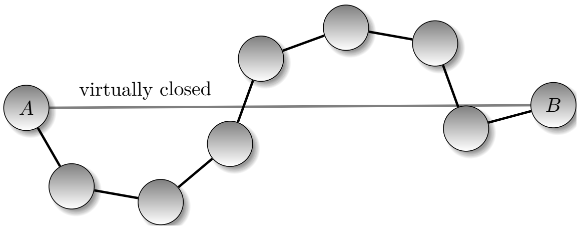

Figure 4.6.: The simplest closure directly connects the first and the last monomer.

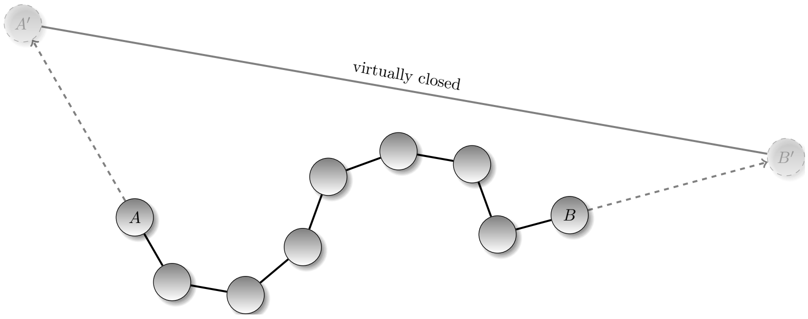

Figure 4.7.: The closure (CI) shifts both termini of the polymer, A and B, to a point far outside the polymer and then close the new termini, A' and B', virtually.

results. The first one (CI) extends the first and the last bond of the polymer, so that the new termini are located far outside of the rest of the polymer. These new termini are then connected directly by a virtual bond, see Figure 4.7. The second closure (CII) is inspired by tying a real knot: it shifts both termini of the polymer on the line connecting the two monomers in opposite direction. These new termini are not closed directly, instead one chooses a line perpendicular to the connecting line. On this perpendicular bisector a new virtual monomer is placed which again is located far outside the polymer. Now the new termini are virtually closed through this new monomer, see Figure 4.8. The used closure has an influence on the knot type of a conformation, but the estimated mean values of $\Delta_p(-1.1)$ using CI or CII shows no qualitative difference, see Figure 4.9. Please note that the presented results for $\Delta_p(-1.1)$ are canonical mean values, $\langle\Delta_p(-1.1)\rangle$ can take on any numerical value, although every individual measurement of $\Delta_p(-1.1)$ can only have distinct values, see Table 4.1. So if $\langle\Delta_p(-1.1)\rangle$ takes on exactly one value corresponding to a specific knot type, one can conclude that every measured conformation is of that knot type.

4.2.5. Error Analysis

All errors estimations in this thesis are obtained via the jackknife method [26], which splits the data in blocks and calculate the errors based on these blocks. For methods like the weighted histogram analysis method it is maybe the method of choice to do a proper error analysis with an acceptable computation effort. I want to note

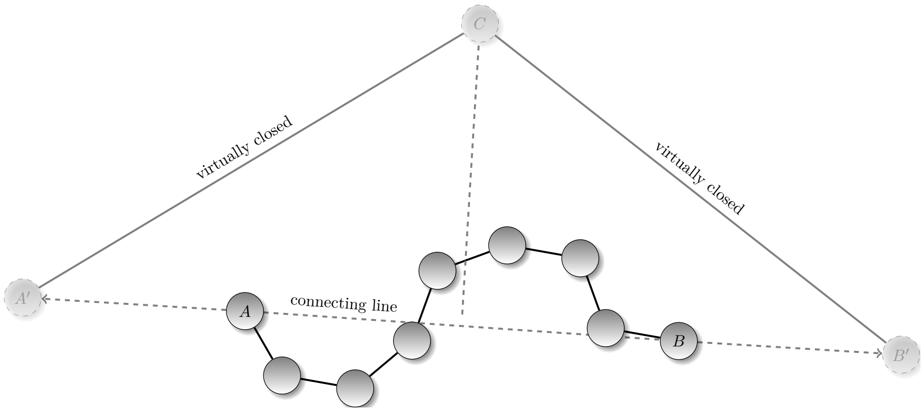

Figure 4.8.: The closure (CII) shifts both termini, A and B, on the line connecting these termini far outside the polymer. A new monomer C is virtually created on a line perpendicular to the connecting line and the new termini, A' and B', are virtually closed through C.

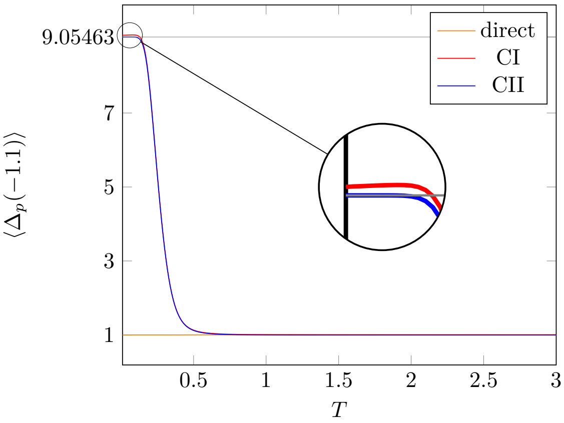

Figure 4.9.: $\Delta_p(-1.1)$ measured with all three closures (direct, CI, and CII) at $\kappa = 3$ over a large temperature range. The two more elaborated closures, CI and CII, lead to almost the same numerical values. There is only a small deviation at very low temperatures. The statistical errors are on the order of the line width and omitted in this plot.

that the errors may not be visible in some plots due to the resolution of the print in combination with very small error bars. In all figures showing results from the weighted histogram analysis method only errors for some selected points are shown such that the plots are not overburdened with errors along the whole abscissa.

4.3. Microcanonical Analysis

To get a better insight in the thermodynamical behavior, especially the different pseudo-phase transitions, of a complex but finite system, the microcanonical analysis is a complementary approach which can contribute to the knowledge obtained from the classical canonical expectation values. A detailed description of microcanonical thermodynamics and how to approach the microcanonical ensemble via Metropolis simulations can be found in [39]. Here, I follow the more modern approach given in [55, 56, 95]. The basis of the microcanonical analysis is the density of states $\Omega(E)$ which can be obtained from the weighted histogram analysis method of canonical simulations, see section 9.2.1.1, or directly from generalized ensemble simulations, see section 9.3. From the density of states the microcanonical entropy $S(E) = k_B \ln \Omega(E)$ and its derivative the microcanonical temperature

$$\beta_{\mathrm{micro}} = \frac{d}{dE} S(E) \tag{4.14}$$

can be derived. In the thermodynamic limit, when the microcanonical and canonical ensemble are identical, $S(E)$ is a strict concave function and the microcanonical temperature is equal to the canonical temperature (the temperature of the heat-bath the canonical ensemble is connected to). However, for a finite system structural transitions are reflected in $S(E)$ by a change of the curvature of $S(E)$ induced by the interplay of energy and entropy. Thus, inflection points in β_{micro} indicate structural transitions of a finite system. To identify these points the derivative of $\beta_{\mathrm{micro}}(E)$ with respect to the energy

$$\gamma(E) = \frac{d}{dE} \beta_{\mathrm{micro}}(E) = \frac{d^2}{dE^2} S(E) \tag{4.15}$$

is a convenient observable, since the inflection points in β_{micro} are maxima in $\gamma(E)$, which are easier to identify than the inflection points itself. At a first-order phase transition the phase-coexistence leads to a non unique mapping between β_{micro} and E, and therefore a backbending and a positive slope of $\beta_{\mathrm{micro}}(E)$ at $E = E_{\mathrm{tr}}$ occurs. For a negative slope there cannot be a phase-coexistence, and thus the transition is classified as second-order phase transition. For the numerical identification $\gamma(E)$ is more convenient where the height of the maxima separates first-order from second-order phase transitions:

$$\gamma_{\text{tr}} = \gamma(E_{\text{tr}}) > 0 \quad \text{first-order} \tag{4.16}$$

$$\gamma_{\text{tr}} = \gamma(E_{\text{tr}}) < 0 \quad \text{second-order.} \tag{4.17}$$

One advantage of the microcanonical analysis is that it allows distinguish pseudo-phase transitions where signals of canonical observables overlap. In contrast to the canonical analysis, the microcanonical analysis works out quite well for very small systems. On the other hand it becomes more complicated for larger systems. The microcanonical analysis needs quite an amount of statistics to produce utilizable results. Usually, one can use Bézier smoothing, which does not change the results qualitatively, to reduce the amount of needed statistics. However, it is hard to use these result quantitatively and a valid error estimation is even more complicated and not done in most investigations. In this thesis the microcanonical analysis is only used to cross-check the results obtained from the canonical analysis. However, the microcanonical analysis was very useful to identify and classify pseudo-phase transitions in regions where multiple phase-boundaries merge and the signals of the pseudo-phase transitions overlap.

5. Conformational Phases of the Free Semiflexible Polymer

This chapter starts with a brief overview of the behavior of the flexible homopolymer. Although already described in many previous works for similar models, it is a good basis to describe the stiffness dependent behavior of the semiflexible polymer. Then an overview of the complete pseudo-phase diagram of the free semiflexible bead-stick polymer for $N = 14, 28,$ and 42 is given. Based on these pseudo-phase diagrams the individual pseudo-phases and some selected pseudo-phase transitions are described in more detail. The pseudo-phase diagrams are constructed by employing the canonical expectation values of several observables, $\mathcal{O} = E_{\text{LJ}}, E_{\text{bend}}, R_g^2, R_{ee}, \lambda_1, \lambda_2, \lambda_3, \varkappa^2, b, c,$ and $\Delta_p(-1.1)$, obtained from two-dimensional replica-exchange Monte Carlo simulations, see section 9.2.2. The results of these simulations are crossed checked for different N and κ with parallel multicanonical simulations, see section 9.3.2.

One may argue that the polymer length is relative short, but the probably much more complex pseudo-phase diagram for long chains will not help to get an overview of the generic behavior. Moreover, the main reason to not use much longer polymers is that even with modern high-performance compute cluster is not possible to simulate much longer polymers for such a wide range of parameters. Especially, for large stiffnesses and low temperatures the needed amount of compute time to obtain proper results increases dramatically. For example, the time needed to simulate a flexible ($\kappa = 0$) polymer consisting of 256 monomers was roughly the same as the time needed to simulate a stiff ($\kappa = 30$) polymer with 42 monomers[1] and on the order of a few thousand CPU hours.

5.1. Flexible Bead-Stick Homopolymer

For the simulation of the flexible polymer exactly the same simulation methods are used as for the semiflexible case, but κ is evaluated at 0.1[2]. In principle, there are 3 different phases, namely the swollen/elongated (E) phase, the coiled/collapsed (C) phase, and the frozen (F) phase, separated by peaks in thermal derivation of $\frac{d}{dT}\left\langle R_g^2 \right\rangle$ and C_V, see Figure 5.1. Table 5.3 shows exemplary conformations for all three phases.

---

[1] This holds as long as the temperature range should include the swollen and globular phase. Simulate the frozen pseudo-phase at low κ gets even more complicated and time-consuming.

[2] For numerical reasons it is not set to zero which has no significant influence since the behavior of the polymer at $\kappa = 0.1$ is even quantitatively very similar to the behavior at $\kappa = 0.0$. For small κ the Hamiltonian is dominated by the Lennard-Jones energy.

All three phases persist in the limit of infinite chains [113], as long as the interaction range of the non-bonded interaction is sufficient large. If the interaction range is lower than a certain threshold the collapse transition and the freezing transition coincide and the globular phase vanishes [107, 113]. A similar behavior is also known from colloidal systems [22]. The swollen phase is dominated by the entropy and can be considered as a vapor phase. Non-adjacent monomers are not bound to each other and freely moving, beside the constraint of their bonding to adjacent monomers. While lowering the temperature the polymer undergoes a second-order phase transition into the globular phase, which is defined by the interplay of the entropy and the Lennard-Jones energy. It is unstructured but compact and globular, similar to a liquid phase of a fluid. At the lowest temperatures the polymer goes into a frozen phase (F). Honestly speaking, the frozen phase is not a single phase and better described by a conglomerate of different crystal-like sub-phases. In F the pairwise monomer-monomer contacts are maximized by minimizing the distance between the monomers, thus the Lennard-Jones energy is minimized. Any small perturbation in the system size or κ can result in changes of local energy minima and thus changes in the structure of the polymer. In Figure 5.2 the thermal derivation of the shape parameters signals three different “frozen” structures. It would be appealing to describe this phase by a glass-like behavior, however, a detailed analysis of the glassiness of F would be necessary to give any definitive statements, which is out of the scope of this work. In principle, the frozen phase is very model dependent. If the bonds are modelled via finitely extensible nonlinear elastic (FENE) springs and have a length identical to the distance of the minimum of the Lennard-Jones potential, the ground-state conformations are much more regular and Mackay or anti-Mackay patterns occur. However, for models not tuned in a way that the bond length is identical to the minimum of the potential for the intra-polymer interaction one would not find such regular structures. In such a case it would be impossible for all monomers to “fall” into the valleys of the intra-polymer potential. For a more detailed analysis of these low temperature pseudo-phases Schnabel et al. [93, 96] done a very elaborated study of the crystallization process of elastic flexible polymers using a bead-spring polymer model.

5.1.1. Collapse/Θ-Transition

The collapse transition between the globular and swollen phase (E ↔ C) is also known as Θ-transition. The term Θ-transition promotes the fact that changing the solubility of the polymer with its solvent leads to the same effect as changing the temperature. In the bead-stick model the solubility is implicitly modeled through the monomer-monomer attraction between non-adjacent monomers. Although there was some debate of the behavior at the Θ-transition [82, 99, 113], it is now quite well understood. The Flory-Huggins mean-field theory [30, p. 566] leads to the following

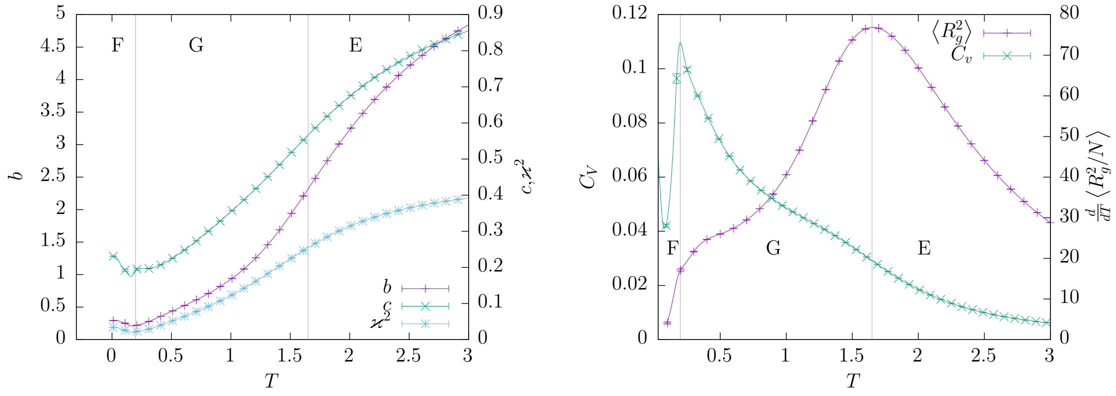

Figure 5.1.: (left) The temperature profile of the three shape parameters b, c, $\varkappa^2$ and (right) the thermal derivative of $\left\langle R_g^2 \right\rangle$ and the specific heat capacity c_V measured of a polymer with 28 monomers and $\kappa = 0.1$. The right solid gray line mark the coil-globule transition and the left one the freezing transition.

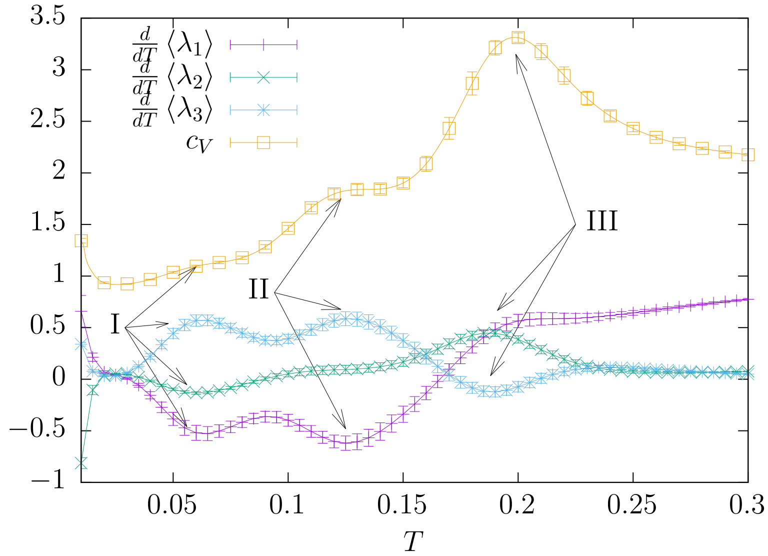

Figure 5.2.: A temperature profile for low temperatures of the derivation of the three eigenvalues of the gyration tensor $\lambda_1, \lambda_2, \lambda_3$ and the specific heat capacity c_V for a polymer consisting of 28 monomers at $\kappa = 0.1$. The temperature range span the frozen pseudo-phase within three different sub-phases are visible separated by the peaks I, II, and III.

Figure 5.3.: Typical conformations of the 3 different phases of a flexible polymer. All three are taken from a parallel tempering simulation with $N = 28$, $\kappa = 0.1$ and E : $T = 3.0$, C : $T = 0.7$, and F : $T = 0.05$.

pseudo-phase	example configuration
swollen (E)	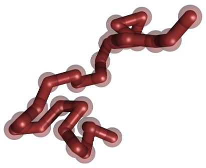
collapsed (C)	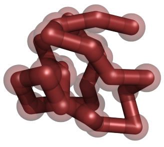
frozen (F)	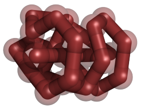

Table 5.1.: Results of the fit of the ansatz (5.1) of the polymer collapse.

T_Θ	a_1	a_2	χ
4.46(1)	−21.13(3)	34.7(2)	≈ 0.2

ansatz for the scaling of the Θ-temperature:

$$T_\Theta(N) - T_\Theta = -\frac{a_1}{\sqrt{N}} + \frac{a_2}{N}, \tag{5.1}$$

with T_Θ being the temperature of the phase transition in the thermodynamic limit and $T_\Theta(N)$ the transition temperature for a polymer with N monomers. The ansatz was shown to be valid for different polymer models, on lattice [113], and for off-lattice models with flexible bonds [99]. For the bead-stick model I obtain $T_\Theta(N)$ from the peak position of the derivative of squared radius of gyration $\frac{d}{dT}\left\langle R_g^2 \right\rangle$ and the derivative of the squared end-to-end distance $\frac{d}{dT}\left\langle R_{\mathrm{ee}}^2 \right\rangle$. Figure 5.4 shows the canonical curves of $\frac{d}{dT}\left\langle R_g^2 \right\rangle$ and $\frac{d}{dT}\left\langle R_{\mathrm{ee}}^2 \right\rangle$ for different N. For both observables the peak shifts to larger temperatures and gets more pronounced for larger N. This effect is quantized by a finite-size scaling presented in Figure 5.5 which shows that the bead-stick model satisfy (5.1) within the statistical errors, see Table 5.1.

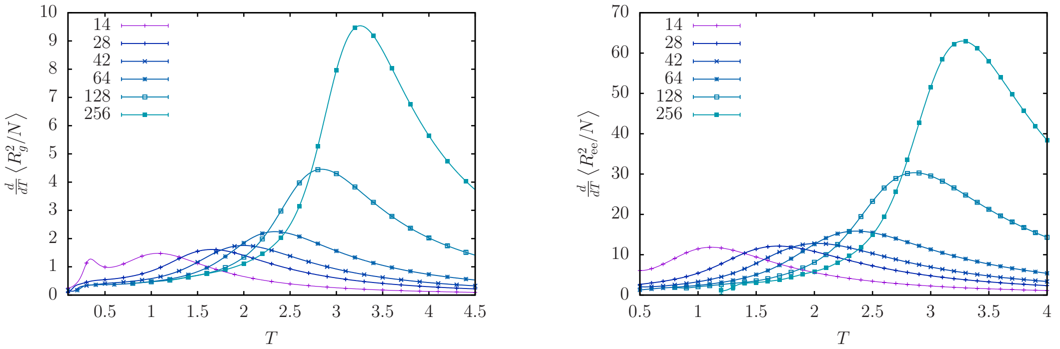

Figure 5.4.: (left) Thermal derivative of the squared radius of gyration and (right) squared end-to-end distance for different polymer lengths N. The most right peak in each temperature profile corresponds to the collapse transition. The transition shifts to higher temperatures and gets more pronounced for larger N.

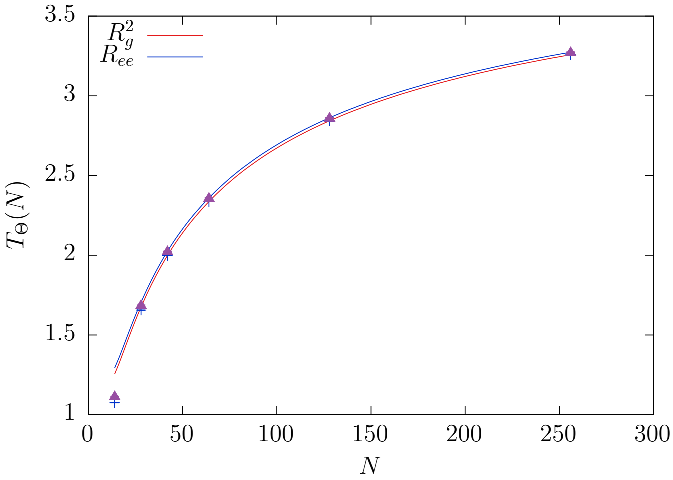

Figure 5.5.: Finite-size scaling of the Θ-transition temperature. The data points agree very well with (5.1) which is shown by solid lines Due to strong finite size effects, $N = 14$ is not taken into account.

5.2. From Flexible to Stiff

The pseudo-phase diagram gets much richer, in the sense of different emerging structures, as soon as an adjustable bending stiffness is introduced. Figures 5.6, 5.7, and 5.8 show the pseudo-phase diagram for $T \in [0.01, 3]$ and $\kappa \in [0, \kappa_{\max}(N)]$ for three different polymer lengths $N = 14, 28, 42$, with $\kappa_{\max}(14) = 8.0$, $\kappa_{\max}(28) = 18$, and $\kappa_{\max}(42) = 35$. The black lines on the right-hand side mark the regions of the thermal most active regions where several canonical observables and the microcanonical analysis indicate pseudo-phase transitions. The overall size of the polymer in the different pseudo-phases is given in the left-hand side in Figures 5.6, 5.7, and 5.8 by presenting the squared radius of gyration as a surface plot. The different symbols mark the position of a maximum of the following observables: $\frac{d}{dT}\left\langle R_g^2 \right\rangle$(violet pluses), $\frac{d}{dT}\left\langle E_{\mathrm{LJ}} \right\rangle$(green crosses), $\frac{d}{dT}\left\langle \Delta_p(-1.1) \right\rangle$(blue stars), and $\frac{d}{dT}\left\langle b \right\rangle$(orange squares).

Although there are numerous differently shaped conformations, only several general motifs crystallizes out and build up the complete pseudo-phase diagram, at least for the polymers lengths simulated in this work. The principal structure of the pseudo-phase diagram of short polymers is summarized in Figure 5.9. I have done a few additional simulations with other parametrizations of bead-stick and bead-spring models with finitely extensible nonlinear elastic (FENE) bonds; all show qualitatively the same structure of the pseudo-phase diagram.

5.2.1. Pseudo-Phase Diagram in Detail

For small bending stiffnesses and high temperatures, as in the flexible case, the polymer is dominated by the entropy and in an elongated conformation (E) equivalent to the gaseous phase of a liquid. When increasing the bending stiffness at high temperatures the bending energy becomes more important and the polymer forms rod-like conformations (R). If the bending stiffness is large enough $\kappa > \kappa_R$, the bending energy dominates the Lennard-Jones energy and the polymer is in a rod-like conformation independently of the temperature. For values of κ smaller than κ_R the polymer always undergoes a kind of collapse transition with a transition temperature dependent on the actual value of κ. Since the polymer rapidly changes its size during the transition, the collapse transition is best observed in the squared radius of gyration or the end-to-end distance, see Figure 5.10.

The motif of the collapsed phase crucially depends on the bending stiffness. For low values of κ the transition remains similar to the Θ-transition. It is also second-order-like and the polymer contracts into the globular phase (G) when lowering the temperatures. This globular phase does not differ qualitatively from the globular phase of the flexible polymer and is similar to the liquid phase of a fluid. The pseudo-phase denoted with AG in Figure 5.6 is a curiosity of the very short polymer length. In this region of the phase diagram both termini have a high probability to align themselves to each other, but the rest of the polymer is globular and unstructured. In principle, it is possible to find sub-phases in G for all polymer length. Even still determined by entropy, the polymer start to form a specific shape different from a

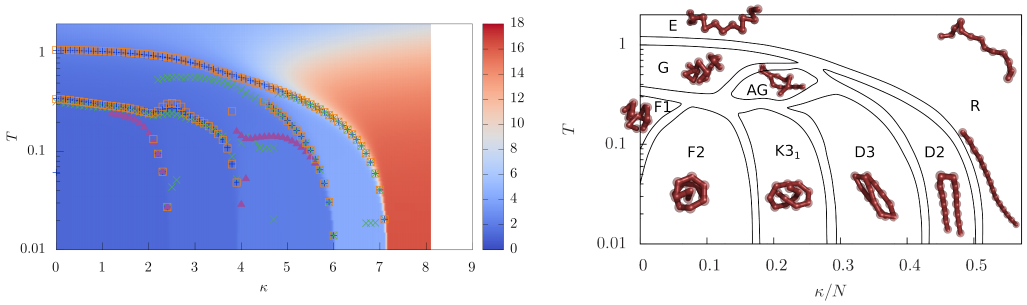

Figure 5.6.: The pseudo-phase diagram of a semiflexible homopolymer with 14 monomers. The left-hand side shows the squared radius of gyration in the (T, κ)-plane. Locations of the peaks are marked by violet pluses - $\frac{d}{dT}\left\langle R_g^2\right\rangle$, green crosses - $\frac{d}{dT}\left\langle E_{\mathrm{LJ}}\right\rangle$, blue stars - $\frac{d}{dT}\left\langle D_p(-1.1)\right\rangle$, orange squares - $\frac{d}{dT}\left\langle b\right\rangle$. The right-hand side shows the aggregated pseudo-phase diagram, subsuming the data analysis of all measured observables. The pseudo-phase transitions are labeled as follows: E - extended phase, G - globular phase, R - rod-like phase, DN - $N-1$ times bent , K - knot like states, F - frozen state.

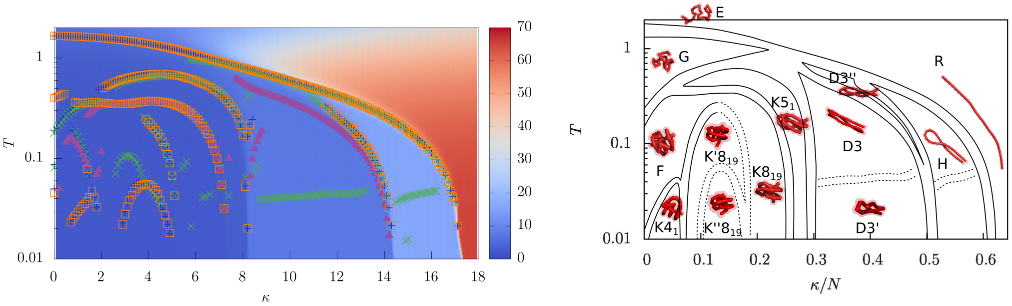

Figure 5.7.: The pseudo-phase diagram of a semiflexible homopolymer with 28 monomers. (left) The squared radius of gyration with peaks of the same observables as in Figure 5.6. The right-hand side are again the aggregated phases with the same labels, with H labeling the pseudo-phase where the polymer forms a hairpin.

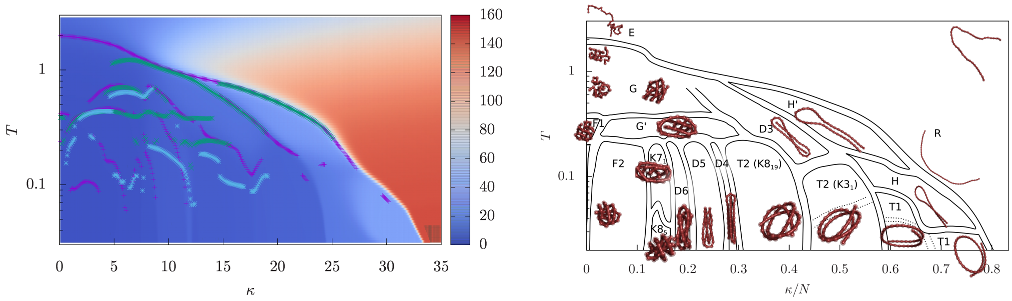

Figure 5.8.: The pseudo-phase diagram of semiflexible homopolymer with 42 monomers. Both plots are identical to the ones in Figures 5.6 and 5.7. TN mark the phases consisting of toroidals. Both TN pseuo-phases form also a torus knot (knot type in parentheses).

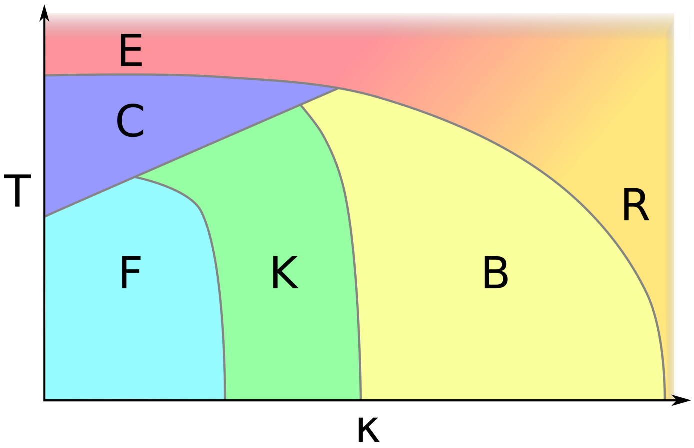

Figure 5.9.: Generic structure of the pseudo-phase diagram for short polymers. The different pseudo-phases are observable for all measured polymer lengths and labeled as in Figures 5.6, 5.7, and 5.8. B subsumes all kind of bent conformations.

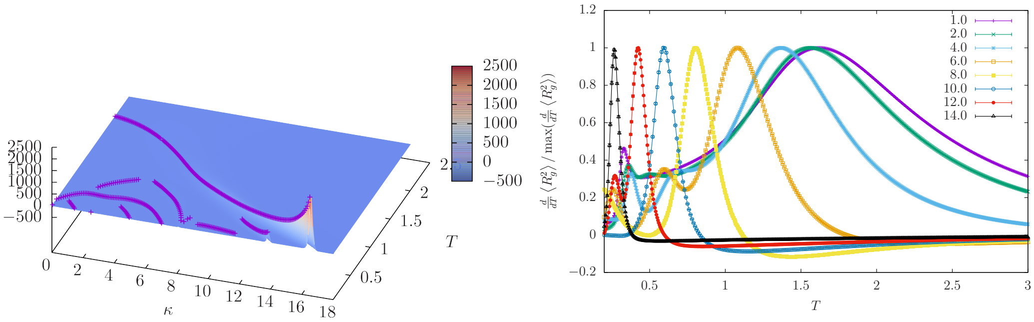

Figure 5.10.: (left) Surface plot of $\frac{d}{dT}\left\langle R_g^2\right\rangle$ with its maxima marked with violet pluses. Especially, for large κ the signal of the collapse transition dominates, therefore, the temperature profile for different κ of $\frac{d}{dT}\left\langle R_g^2\right\rangle$ (right) is normalized by its maximum value. Both profiles stems from a simulation with a polymer consisting of 28 monomers.

spherical distribution in these sub-phases, e.g., G' of the 42mer, see Figure. 5.8.

The transition into the globular phase persists up to a value for κ/N slightly smaller than ≈ 0.3. For the polymer length measured here, the exact localization of this value for κ/N is very hard, since at this location in the pseudo-phase diagram the transition changes from second-order-like to first-order-like. Therefore, the maxima of the different thermal derivatives overlap and a plateau emerges instead of single peaks. This makes it hard to distinguish the different maxima and to locate the exact κ value where the transition switches from second-order to first-order behavior. Moreover, one cannot assume that here exists such a fixed value for κ/N for $N \to \infty$ at all.

Below the globular phase, temperature wise, comes the frozen phase (F) which is again similar to the frozen phase of the flexible polymer. Starting from that frozen phase and increasing κ at constant temperature, first a transition into knotted conformations (K) occurs and at even higher values for κ a transition from the knotted into bent conformations (B). In this “bent” pseudo-phase several motifs are subsumed, namely either multiple linear strands (DN), where N denote the number of parallel strands, hairpin (H) or toroidal conformations (TN), where N denotes the number of full loops. All have in common that the polymer backbone is aligned with itself. These changes of the structure at different κ and constant temperature can be very nicely seen in the κ-profile for the different observables measuring the size and the shape of the polymer or the surface plot of $\langle R_{\mathrm{ee}}^2\rangle$, see Figure 5.11.

The different emerging structures are defined by the interplay of the Lennard-Jones and bending energy. In Figure 5.12 one can see that when increasing κ the bending energy (violet) grows until it is strong enough that a transition into a new structure is energetically favorable. At each transition the bending energy and the Lennard-Jones energy (blue) change in opposite direction. Away from the transitions the Lennard-

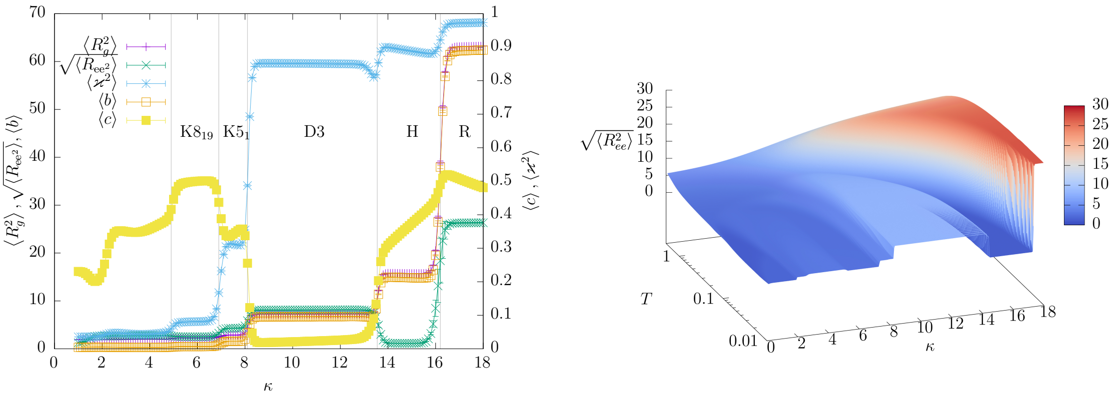

Figure 5.11.: (left) Profile of the squared radius of gyration $\left\langle R_g^2 \right\rangle$, the square root of the squared end-to-end distance $\langle R_{\mathrm{ee}}^2 \rangle$, the relative shape anisotropy $\langle \varkappa^2 \rangle$, the acylindricity $\langle c \rangle$, and the asphericity $\langle b \rangle$ along the κ axis at a constant temperature of $T = 0.1$ for the 28mer. (right) Surface plot of the square root of $\langle R_{\mathrm{ee}}^2 \rangle$ for the 28mer.

Jones energy and $\frac{1}{\kappa} \langle E_{\mathrm{Bend}} \rangle$ [3] make nice plateaus. Within each knotted (K5$_1$, K8$_{19}$) or bent (D3, H, R) pseudo-phase there are almost no energetic changes, at least at constant temperature. However, the κ-profile in Figure 5.11 of the acylindricity (yellow) and less pronounced the relative shape anisotropy (blue) shows that there are small structural changes within the pseudo-phases when increasing the bending stiffness. Especially in the D and H pseudo-phase the increasing acylindricity indicates that the radius of the smallest cylinder which completely surrounds the polymer increases without changing the overall size of the conformation, $\left\langle R_g^2 \right\rangle$ and $\langle R_{\mathrm{ee}}^2 \rangle$ are almost constant within each pseudo-phase.

In the following I will describe the different regions in the pseudo-phase diagram in more detail. Therefore, I show for the most effects only one or two examples, but carefully checked the described behavior for all measured polymer lengths. In most cases I use the 14mer or 28mer, the more complex pseudo-phase diagram of the 42mer does not contribute to the comprehension of the overall structure.

5.2.2. “Frozen” Pseudo-Phases

As mentioned before, the bead-stick model does not form real crystals. For this to happen, the bonds have to be modelled via flexible springs with a not to large spring constant, as it is done in [94, 96, 99]. Instead, F consists of many different subphases with many metastable states. For example, in Figure 5.13 the two-dimensional histograms of the energy and the squared end-to-end distance show that there is a coexistence between conformations with different end-to-end distances. Especially for the 42mer one observes several maxima, some only weakly pronounced, and thus

---

[3] The bending energy divided by κ measures in some sense the mean angle distortion between neighboring bonds.

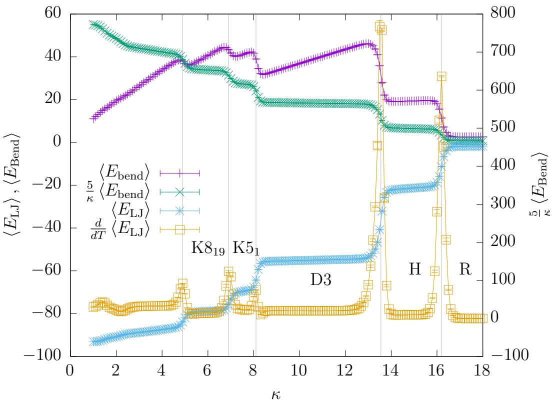

Figure 5.12.: Profile of $\langle E_{\mathrm{LJ}} \rangle$, $\langle E_{\mathrm{Bend}} \rangle$, $\frac{5}{\kappa} \langle E_{\mathrm{bend}} \rangle$, and $\frac{d}{dT} \langle E_{\mathrm{LJ}} \rangle$ along the κ axis at a constant temperature $T = 0.1$ for the 28mer. $\frac{5}{\kappa} \langle E_{\mathrm{Bend}} \rangle$ is the bending energy divided by κ and thus takes only the angle distribution into account (the 5 is only used to bring it to a scale where it is comparable to the other observables).

for this choice of parameters ($T = 0.11$, $\kappa = 3.0$) many metastable states. The two histograms in Figure 5.13 are just an example, a small deviation in the temperature, the bending stiffness, or the length of the polymer may lead to a reorganization of the polymer structure and thus to a qualitatively different histogram. Nevertheless, all these conformations have in common that they try to minimize the Lennard-Jones energy and, thus, all conformations are very dense. In the end, the strong dependence on the parameters would lead to numerous sub-phases within F with many solid-solid-like transitions between them. Moreover, this behavior is not generalizable and would strongly depend on the chosen model. In the following all the different sub-phases are subsumed in F.

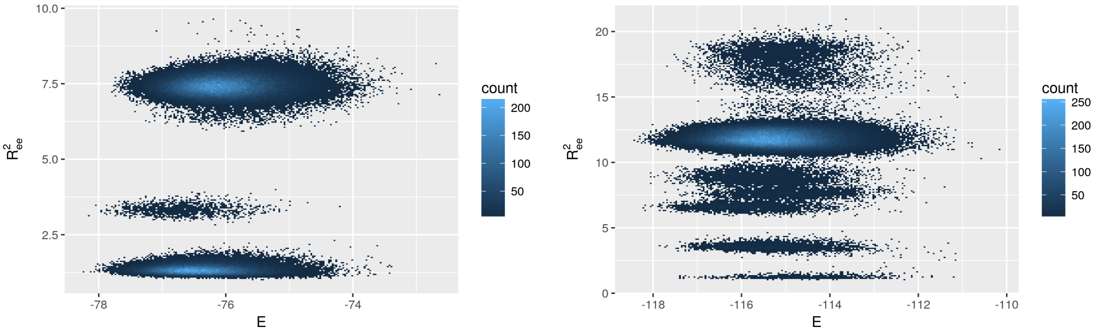

Figure 5.13.: Two-dimensional histograms in terms of the energy and the squared end-to-end distance of (left) a 28mer at ($T = 0.11$, $\kappa = 1.5$) and (right) a 42mer at ($T = 0.11$, $\kappa = 3.0$). The number of dots represent the number of conformations with a specific (E, R^2_{ee}) pair. For the 28mer one can easily identify 3 different clusters corresponding to three different states all with a different end-to-end distance. The histogram of the 42mer shows one dominant cluster, but also four to seven less pronounced clusters which correspond to metastable states with different end-to-end distances.

5.2.3. "Knotted" Pseudo-Phases

The first simulations of knotted polymers were done in 1975 [34]. Since then, most of the investigations are either concerned with knots in specific proteins or the occurrence probability and behavior of knots in the swollen or collapsed phase of polymers. By scanning through different databases [68, 71, 108] several proteins which form knots have been found. The most comprehensive work has been done by Virnau et al. [112], which have scanned the whole protein database[4] and revealed 36 different proteins forming relative simple knots. Today many more knotted proteins are known and listed in databases like ProtKnot [52], but still only a small fraction of the known proteins form knots. Simulations of randomly sequenced lattice HP polymers [119] suggest that evolution somehow avoid knotted proteins. On the other

Figure 5.14.: Typical conformations of the knotted pseudo-phases.

trefoil knot ($K3_1$)	cinqfoil knot ($K5_1$)	$K8_{19}$
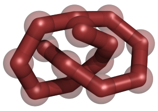	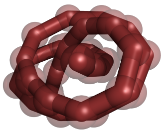	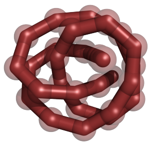

---

[4] `www.pdb.org` [13]

hand the knots in the few known knotted protein structures might have some functionality. For example in the human ubiquitin hydrolase, the 5_2 knot might prevent the protein from being pulled into the proteasome [112]. This effect was investigated in more detail by molecular dynamics simulation of knotted proteins pulled through a pore, depending on the force the knot blocks the pore and prevents the protein from entering.

Most of the works concerning knots in synthetic polymers investigate either the occurrence probability and the size of knots in the swollen or globular phases of the polymer, see References [24, 63, 64, 67, 111], or the mechanical properties of knots [89] and the dynamics in unknotting [61]. For a flexible polymer the unknot probability, the probability that no knot is formed, in the swollen or globular phase goes to zero if the number of monomers increases. Which means that if a flexible polymer is long enough, it almost ever forms a knot. These knots are created by entropy are somehow similar to the annoying knots occurring in cables of headphones or anything comparable to a long linear string and fitting into a trouser pocket. The distribution of the random knots in polymers tends to complexer knots if N increases [111].

Of course, I also found these "random" knots in the swollen (E) and collapsed (G) phases as well, but the knots found in the region marked with (K) are of completely different nature. In that region of the pseudo-phase diagram all, or almost all, conformations of the polymer are of one knot type and can be even identified by eye as a knot, see Table 5.14. For all "knotted" pseudo-phases the expectation value for $\Delta_p(-1.1) \equiv D$, see Figure 5.15, takes on exactly one value out of Table 4.1. Therefore, in these pseudo-phases there is no fluctuation of the knot type, hence one can call the knot thermodynamically stable.

The knot parameter D itself is of course a very good phase separation parameter to identify these phases. In Figure 5.16 the knot parameter $\langle D \rangle$ is much more suitable to identify the knotted phase of the 14mer than more classical observables like the mean total energy per monomer $\frac{1}{N}\langle E \rangle$ or the squared radius of gyration $\left\langle R_g^2 \right\rangle$. $\frac{1}{N}\langle E \rangle$ and $\left\langle R_g^2 \right\rangle$ have a very similar shape at $\kappa = 1.0$ (no knotted phase) and $\kappa = 3.0$ (K3_1 phase), whereas $\langle D \rangle$ has a different shape in the two cases.

A very interesting fact is that all the knot types of the stable knotted pseudo-phase are so called torus knots, with except for the 4_1 knot. A torus knot can be constructed by winding up a closed loop on the surface of a torus. Each torus knot is defined by two coprime numbers (p, q), where q counts for the number of windings around a circle in the interior of the torus and p counts for the number of windings around the axis of rotational symmetry of the torus. Torus knots seems to reduce the bending energy for compact polymer conformations. They are also found to be important in different context. In [5] it was found by simulation of DNA in a virus capsuid that the DNA has a high probability to form a torus knot.

The K4_1 pseudo-phase does not fit to the other knotted phases not only by not being a torus knot. In contrast to all other knotted pseudo-phases, the K4_1 pseudo-phase also exists at $\kappa = 0.0$ (no bending energy). In this sense the K4_1 pseudo-phase fits more in the frozen pseudo-phases which minimizing the monomer-monomer

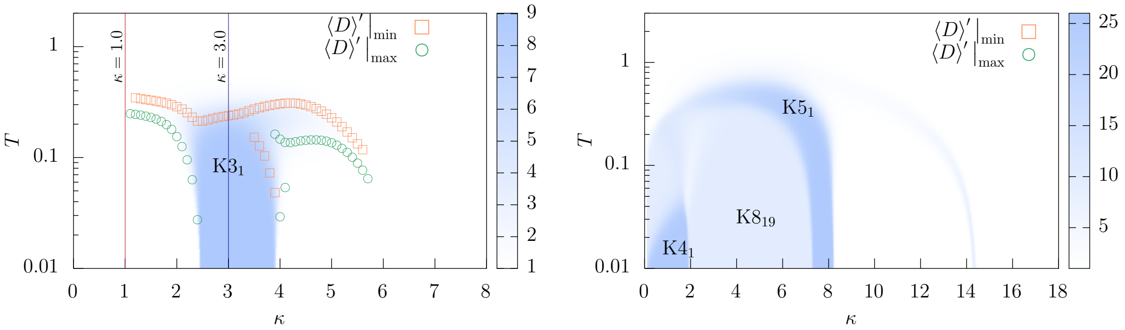

Figure 5.15.: Surface plot of $\langle D\rangle$ measured with Closure II for a 14mer (left) and a 28mer (right). The green circle marks the position of maxima of $\frac{d}{dT}\langle D\rangle = \langle D\rangle'$ and the orange squares the minima of the same observable. The blue regime, $\langle D\rangle = 9.05463$ in the left figure marks the K3$_1$ knot phase. In the right figure there are three different knotted phases, K4$_1$: $\langle D\rangle = 25.09099$, K5$_1$: $\langle D\rangle = 25.45754$, and K8$_{19}$: $\langle D\rangle = 9.72667$, in all other parts of the right figure the value for $\langle D\rangle$ is not singular, hence one finds a distribution of different knots in these regions.

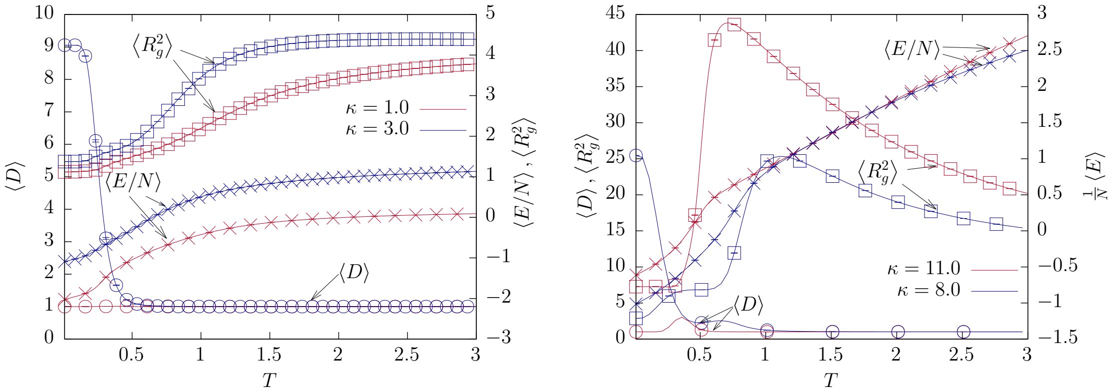

Figure 5.16.: The temperature profile for the (left) 14mer and (right) 28mer at different values for κ. In contrast to the squared radius of gyration $\left\langle R_g^2\right\rangle$ and the normalized total energy $\frac{1}{N}\langle E\rangle$, the knot parameter D is a much better observable to distinguish the knotted from the non-knotted pseudo-phases.

distance. It is just “accidentally” also a knot. This holds also for the characteristics of the “knotting” transition explained later, which is different for the K4_1 pseudo-phase in contrast to all other knotting transitions.

With the help of the Figures 5.16 and 5.15 I would like to explain some peculiarities of the knot parameter D. As already mentioned, in a knotted pseudo-phase every polymer conformation has the same value for D, thus also the expectation value $\langle D\rangle$ has exactly this value. This results in a statistical error of $\langle D\rangle$ that is zero. Therefore, any numerical procedure which uses the value of the error of $\langle D\rangle$ has to take this into account.

In the surface plots in Figure 5.15 are several colored regions which are no purely knotted phases. The distribution of different knotted and unknotted conformations lead to an average expectation value $\langle D\rangle$. Looking more closely into these values, one can see that this happens especially in regions in the pseudo-phase diagram where a second-order-like pseudo-phase transition occurs. For example, it occurs at the collapse transition from E to G as small bump in $\langle D\rangle$ of the curve for $\kappa = 11.0, N = 28$ in Figure 5.16. At first glance this seems to be strange, but it can be easily explained: at a second-order-like phase transition the polymer is very volatile in the sense that at the transition the polymer has to be in some state between both phases. This results in a slightly higher chance that the used knot closure indicate a knotted conformation. However, these knots are similar to the random knots found in the globular or extended pseudo-phase. The region in the pseudo-phase diagram of the 28mer, see Figure 5.7, marked with D$3''$ is also surrounded with maxima and minima of $\frac{d}{dT}\langle D\rangle$, see right-hand side of Figure 5.15, but for a different reason. The D$3''$ is a sub-phase of the three times bent phase D3 (three aligned linear strands). It differs from the rest of the D3 phase in the way that the two termini tend to bent inside the polymer. This leads to a high probability that the conformations D$3''$ form a 3_1 knot which is also the reason for the maxima and minima of $\frac{d}{dT}\langle D\rangle$ that surround D$3''$. This occurs also for other bent conformations, where knots from by termini which bent inside the polymer, for example for the T2(K8_{19}) and the T2(K3_1) phase where the toroidal is also a knot similar to what happens to proteins in virus capsids [87].

5.2.3.1. Knotting Transition in Detail

The transitions from structured (bent, frozen, differently knotted) states into knots are quite interestingly. Since these transitions goes from a structured to a differently structured state, one could assume that they should behave first-order-like, similar to other solid-solid transitions. At first glance this assumption seems to be not true, the probability distribution $p(E)$, see Figure 5.17, exhibit no double-peak structure, which would indicate a phase coexistence and thus a first-order-like transition. Moreover, the microcanonical analysis signals no transition at all. The derivative of the microcanonical inverse temperature with respect to the energy $\frac{d}{dE}\beta_{\mathrm{micro}}(E) = \gamma(E)$ exhibit no peak at the energy corresponding to the “knotting” transition, for example the $\gamma(E)$ curve of the 28mer at $\kappa = 8.0$ in Figure 5.18. The canonical curve of $\frac{d}{dT}\langle D\rangle$ and several other observables has a minimum at $T = 0.171$ which indicates the tran-

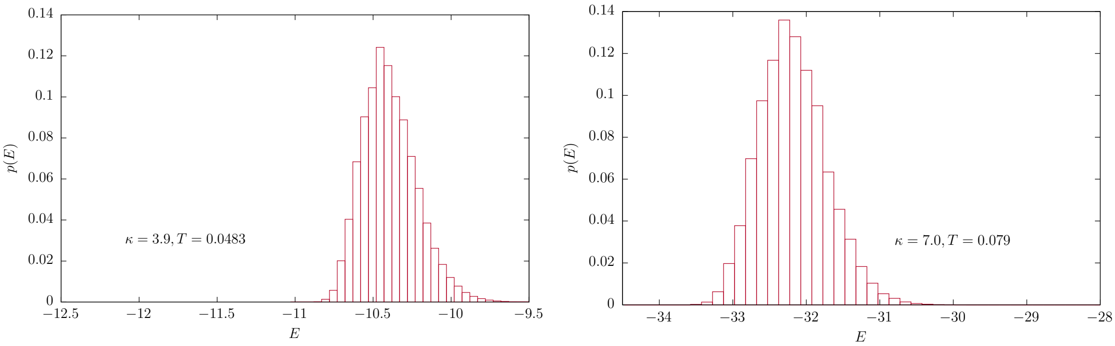

Figure 5.17.: Probability distribution $p(E)$ (left) of a 14mer at the knotting transition K3_1 $\leftrightarrow$ D3 and (right) of a 28mer at the transition between two different knots K5_1 $\leftrightarrow$ K8_{19}. Neither of them show any signals of a phase-coexistence (no double-peak structure).

sition into the knotted pseudo phase. The corresponding canonical expectation value of the energy at $T = 0.171$ is $\langle E\rangle \approx -23.70$ (green curve in Figure 5.18). For comparison also the microcanonical temperature (red curve) is shown in Figure 5.18 shows almost identical behavior. The microcanonical temperature only coincides with the caloric curve $T(\langle E\rangle)$ far away from a pseudo-phase transition. If the microcanonical analysis would signal the knotting transition it has to occur somewhere in the gray region in Figure 5.18, in which $\gamma(E)$ signals no transition at all. It does not have to happen exactly at $E = -23.70$, since being not in the thermodynamic limit, different observables signals different transition temperatures and different energies at which the transition occurs. Nevertheless, several canonical observables indicate the knotting transition very well, see Figure 5.19, only the heat capacity $C_V = \frac{d}{dT}\langle E\rangle$ shows no signal of a pseudo-phase transition. The missing signal in the heat capacity corresponds to the incapability of the microcanonical analysis to observe the knotting transition. In principle, the microcanonical analysis is capable of unrevealing phase transitions which are not visible in C_V if the signals in C_V are overlapped by another phase transition, for example the collapse of the flexible polymer in Figure 5.1. But if there is no signal in the energy or any observable derived from it at all, also the microcanonical observable is not capable to detect the transition.

In contrast to the microcanonical analysis and the one-dimensional energy probability distribution, the two-dimensional probability distribution in dependence of the two constituent energy parts, E_{LJ} and E_{bend}, yield a better understanding of the transition. Figure 5.20 shows $p\left(E_{\mathrm{LJ}}, E_{\mathrm{bend}}\right)$ for several transitions between structured and knotted pseudo-phases. The first three, which correspond to a transition between two structured states, show a typical double-peak structure which indicates a phase-coexistence between the two phases. The one-dimensional probability distributions, shown in Figure 5.17, simulated at the same parameters as the upper two two-dimensional probability distributions in Figure 5.20 exhibit no double-peak structure. This means that the phase-coexistence is not visible in $p(E)$ because the

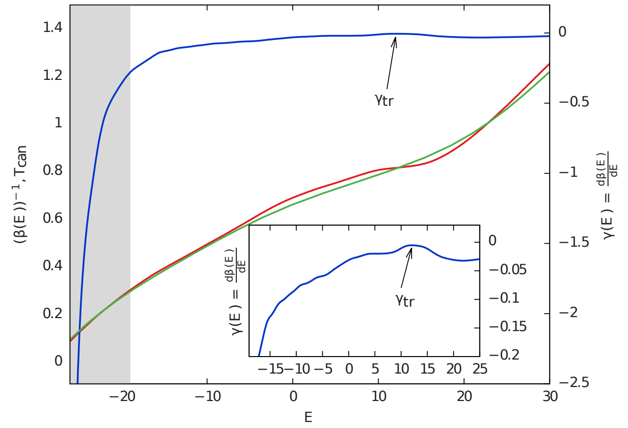

Figure 5.18.: Microcanonical analysis of the 28mer at $\kappa = 8.0$. Shown are the microcanonical temperature $\beta_{\text{micro}}(E)$ (red, obtained from MUCA simulations), its derivative $\gamma(E)$ where the peak γ_{tr} indicates the collapse transition, and the caloric curve $T(\langle E\rangle)$ (green, obtained from parallel tempering simulations, evaluated with WHAM). At $\kappa = 8.0$ the collapse transition changes from second-order-like to first-order-like and several pseudo-phase transition merge into each other.

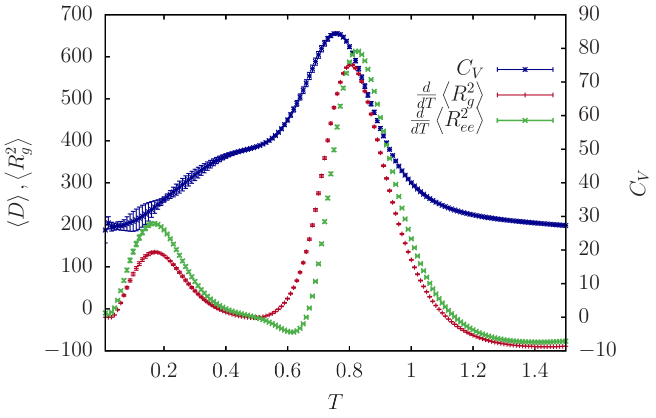

Figure 5.19.: Temperature profile of $\frac{d}{dT}\left\langle R_g^2\right\rangle$, $\langle R_{\text{ee}}^2\rangle$, and C_V for a 28mer at $\kappa = 8.0$. The collapse transition (right peak) is visible as peak in all three observables, whereas the knotting transition (left peak) is not visible in C_V, but in the other two observables.

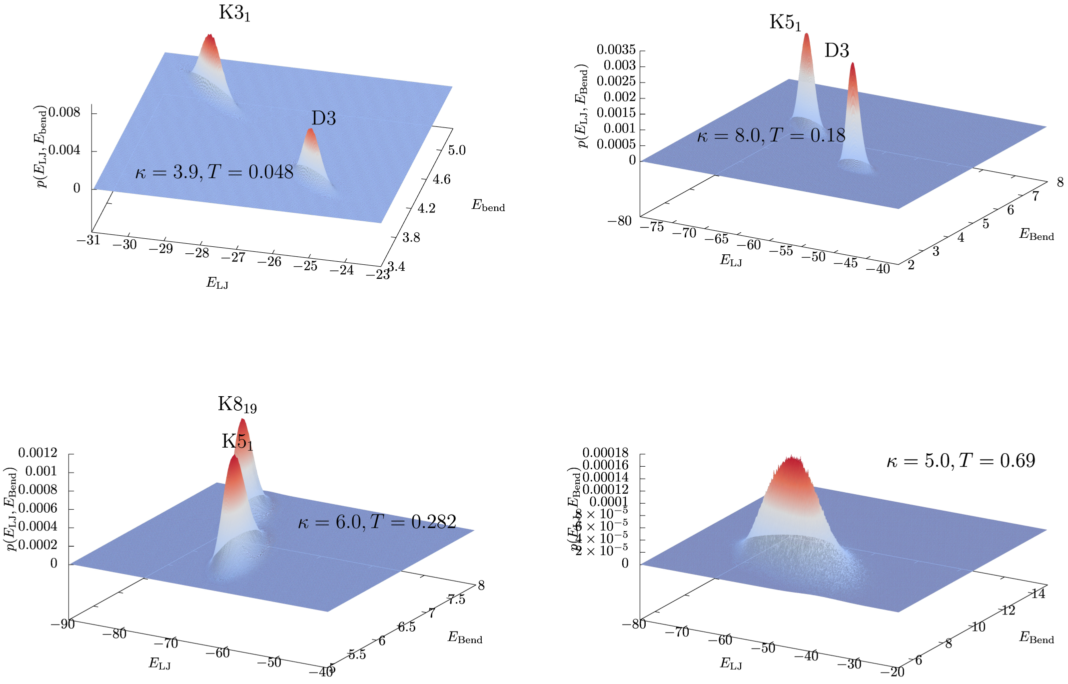

Figure 5.20.: Two-dimensional probability distribution $p(E_\mathrm{LJ}, E_\mathrm{bend})$ for different knotting transitions: (top left) D3 ↔ K3$_1$ of the 14mer, (top right) D3 ↔ K5$_1$ of the 28mer, (bottom left) K5$_1$ ↔ K8$_{19}$ of the 28mer, and (bottom right) G ↔ K8$_{19}$ of the 28mer. The first three belongs to a transition between a knotted and a differently structured conformation, the last one to a transition from an unstructured to the knotted conformation.

two peaks in $p(E_\mathrm{LJ}, E_\mathrm{LJ})$ are perfectly aligned on a projection onto the total energy and both peaks has the same total energy $\langle E \rangle$. Within the transition between the two structured states the total mean energy $\langle E \rangle$ does not change and hence no latent heat is observable. Instead, the two energy parts, E_LJ and E_bend, are transformed into each other. This behavior changes if the polymer enters the knotted phase from an unstructured pseudo-phase, see fourth plot of Figure 5.20, where no double-peak structure is visible. For example, staying at the transition line K3$_1$ ↔ D3 of the 14mer, see Figure 5.6, one observe two peaks in $p\,(E_\mathrm{LJ}, E_\mathrm{bend})$ for low temperatures; with increasing temperature they start to merge until they form a single peak at the transition AG ↔ K3$_1$, thus the phase coexistence vanishes. In that case the transition into the knot is a continuous one.

What's left is to explain the discrepancy between my observations and the pseudo-phase diagram reported in [97], where a bead-spring model with FENE springs to model the covalent bonds. The FENE bonds in [97] adds a bonding energy of form

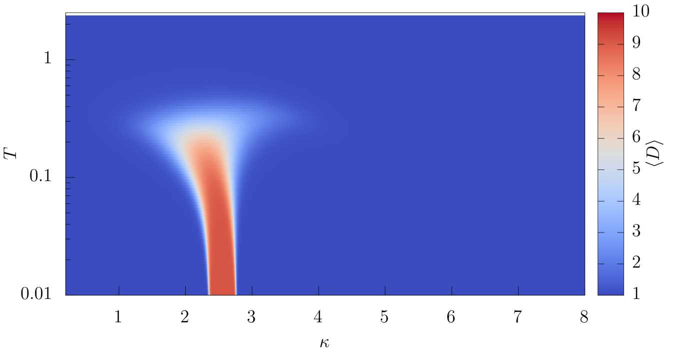

Figure 5.21.: Knot Parameter D measured with closure CII for a bead-spring polymer with the following parameters: $N = 14, K = 40, R = 0.3, r_b = 1, \sigma = 2^{-1/6}$, and $\epsilon = 1$. Although very narrow, there is a region in the phase-diagram where the almost every conformation forms a 3_1 knot.

$E_{\text{FENE}} = -\frac{K}{2}R^2 \ln\left(1 - [(r - r_b)/R]^2\right)$. Of course, Seaton and co-workers does not explicitly look for knots in the pseudo-phase diagram, but I have simulated exactly[5] the same model and also have not observed stable knots. The parametrization in [97] is not a usual one, so I also simulated two more common parametrizations of bead-spring models with FENE springs, with the following parameters: $K = 40, R = 0.3, r_b = 1$ and $K = 60, R = 0.1, r_b = 1.3$. I found stable knots in the pseudo-phase diagram for both parametrizations of the bead-spring model 5.21. The results suggest that the regions of thermodynamically stable knots are much smaller when $r_b \approx r_{\text{min}}$, with r_{min} being the distance of the minimum of the Lennard-Jones potential. The observation that the polymer minimizes its total energy in bent conformations by maximizing the number of monomers located in the Lennard-Jones minima leads to the conjecture: if $r_b \approx r_{\text{min}}$ and the bonds are flexible enough, bent conformations are energetically so strongly favored that knotted states become unlikely. With the special parametrization used in [97] they even vanish completely.

5.2.4. “Bent” Pseudo-Phases

Within the bent pseudo-phases different conformations are subsumed, see Table 5.22. In particular, I found three different motifs, namely closely packed strands (DN), where N is the number of strands, hairpins (H) and toroidal states (TN), where N is the number of complete loops the polymer forms. All three have also been observed with a bead-spring model [97] and a tube-like polymer model [114]. The actual motif depends on the value of κ. For the lowest values of κ this are closely packed strands. When increasing κ the number of strands decrease until for the 28

---

[5] I want to thank Stefan Schnabel and Daniel Seaton for providing me the source code to implement the exactly same force field as they did.

Figure 5.22.: Typical conformations of the bent pseudo-phases.

two linear strands (D2)	three linear strands (D3)	three linear strands (D3″)
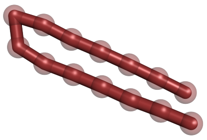	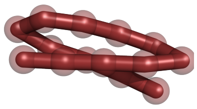	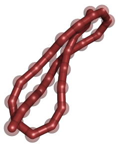
three linear strands (D3′)	hairpin (H)	toroidal (T)
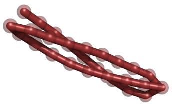	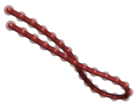	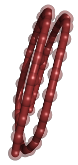

and 42mer hairpin conformations are energetically more favorable, and only for the 42mer at high κ and low temperatures toroidal loops are the energetic most preferable conformations. With increasing κ the radius of the toroid increases and the number of loops decreases. The toroidal with two loops (T2) comes in two flavors, either as K8_{19} knot or as K3_1 knot. These knots are a bit different from those found for lower stiffnesses and more similar to the knots found in DNA molecules packed in phage capsid [87]. For a toroidal it is sufficient that the termini run through the inner loop, in such a case the polymer forms automatically a torus knot. However, also these knots are thermodynamically stable, which means both termini do not fluctuate such the knot type is unique in these pseudo-phases.

The pseudo-phase transition within each motif are best observable in $\left\langle R_g^2 \right\rangle$, $\langle R_{\mathrm{ee}}^2 \rangle$ or $\langle b \rangle$, see Figure 5.11, in particular the squared end-to-end-distance shows by its alternating plateaus that both ends of the polymers also alternates its position relative to each other in each bent pseudo-phase.

All bent pseudo-phases have several sub-phases which are separated in temperature direction, see the dashed lines in Figure 5.7. For example: the canonical analysis, see Figure 5.23, and the microcanonical analysis, see Figure 5.24, of the 28mer at $\kappa = 11.0$ show that one can identify three different sub-phases of the D3 pseudo-phase. For higher temperatures the dangling ends of the polymer tend to bent inside the polymer such that the conformation is equivalent to a 3_1 knot. Compared to the stable knotted pseudo-phases the D″ pseudo-phase does not contain stable knots. I found that approximately 10% of the conformations are knotted. Thermal fluctuations allow the dangling ends to move around such that the most conformations are unknotted. The D3″ is separated by a second-order-like phase transition from the D3 pseudo-phase, indicated by a peak $\gamma_{\mathrm{tr}}^{II}$ which is smaller than 0, see Figure 5.24. The transition can also be seen in the canonical analysis of the shape parameters, for example in the peak T_{tr}^{II} of $\frac{d}{dT} \langle \varkappa \rangle$. In the D3 pseudo-phase the strands tightly align and, since the

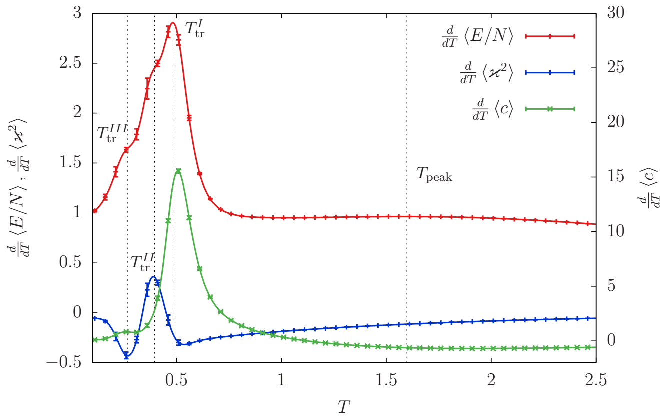

Figure 5.23.: Canonical analysis of the specific heat capacity, $Nc_v = \frac{d}{dT}\langle E/N\rangle$, the thermal derivative of the acylindricity $\frac{d}{dT}\langle c\rangle$, and the thermal derivative of the relative shape anisotropy $\frac{d}{dT}\langle \varkappa^2\rangle$ for $N = 28$ and $\kappa = 11.00$. The peaks and shoulders, T_{tr}^{I-III}, mark the following pseudo-phase transitions $T_{\mathrm{tr}}^{I} : R \leftrightarrow \mathrm{D3}''$, $T_{\mathrm{tr}}^{II} : \mathrm{D3}'' \leftrightarrow \mathrm{D3}$ and $T_{\mathrm{tr}}^{III} : \mathrm{D3} \leftrightarrow \mathrm{D3}'$. The less pronounced peak at T_{peak} and the missing signal in the microcanonical analysis 5.24 indicate that there is not pseudo-phase transition for the crossover from the extended to the rod-like state.

termini of the polymer fluctuate much less, the probability that a 3_1 knots forms is almost zero. If the temperature is even lower, a further second-order-like transition into D3′ occurs. The transition is clearly visible in the microcanonical analysis as peak $\gamma_{\mathrm{tr}}^{III}$ and in the canonical analysis as peak T_{tr}^{III} in $\frac{d}{dT}\langle c\rangle$, see Figure 5.24. In this pseudo-phase the polymer starts to twist itself to reduce the monomer-monomer distance further and thus reducing the total mean energy. Such sub-phases exists also for the bent phases of the 42mer. Generally, as lower the temperature as more the polymer tries to tighten itself, and thereby starts to twist.

The characteristics of the collapse into the bent pseudo-phases ($\mathrm{R} \leftrightarrow \mathrm{D}N, \mathrm{HH}$) and the transition between bent pseudo-phases of different motifs ($\mathrm{D}N, \mathrm{H}, \mathrm{T}N \leftrightarrow \mathrm{D}N, \mathrm{H}, \mathrm{T}N$) are similar to the previously described knotting transition. The main difference is that one can already observe the phase-coexistence as a double peak in the energy probability distribution $p(E)$, see Figure 5.25. However, the suppression in $p(E)$ does not reflect the true suppression between the two phases. The two-dimensional probability distribution $p(E_{\mathrm{LJ}}, E_{\mathrm{bend}})$ is much more suited to see this true suppression, see Figure 5.26.

5.2.4.1. Lower Bound for κ_R

As mentioned before, when the bending stiffness is large enough ($\kappa > \kappa_R$) the polymer does not collapse anymore into a bent pseudo-phase. A rough estimate for the lower bound of κ_R can be obtained by a relative simple approach. Since for low temperatures the entropy effects are not important, the bending of the polymer occurs as

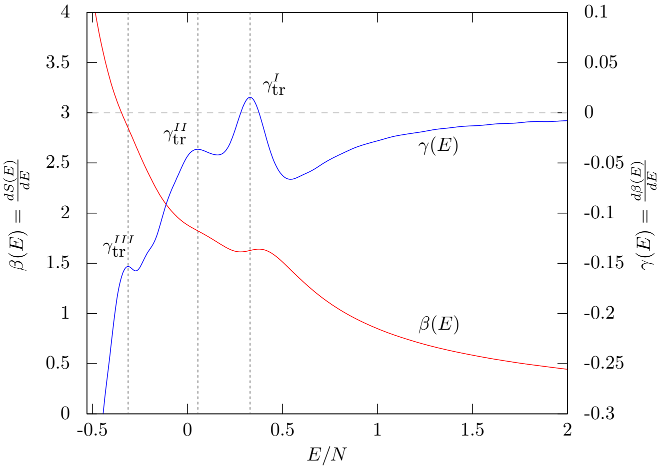

Figure 5.24.: Inflection point analysis of the inverse microcanonical temperature $\beta_{\rm micro}(E)$ and its derivative $\gamma(E)$. $\gamma_{\rm tr}^{I}(E)$ corresponds to $T_{\rm tr}^{I}$ in Figure 5.23 and indicates a first-order-like transition. $\gamma_{\rm tr}^{II-III}$ correspond to the transitions $T_{\rm tr}^{II-III}$, which are second-order-like transitions.

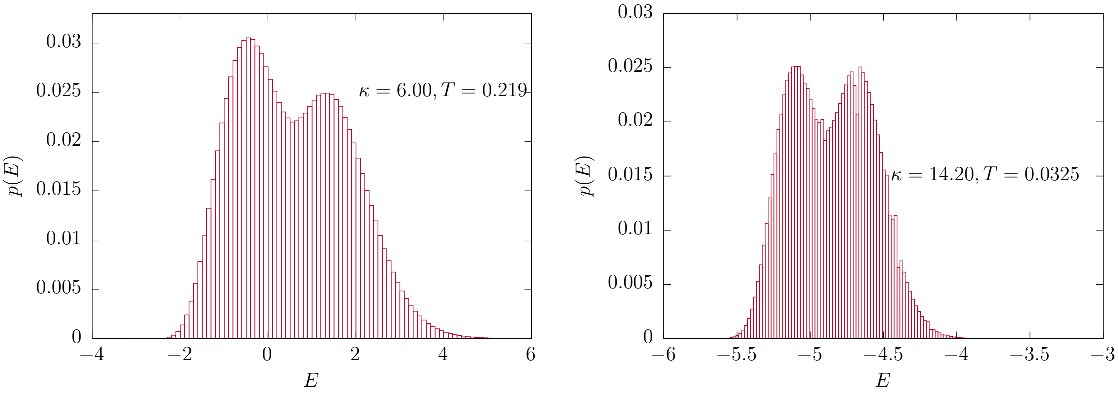

Figure 5.25.: Probability distribution $p(E)$ at (left) the collapse transition from R to D3 of the 14mer and (right) at the transition between H and D3′ of the 28mer. In both distributions one can see the phase-coexistence as a double peak, but the true depression between both phases is not reflected in $p(E)$.

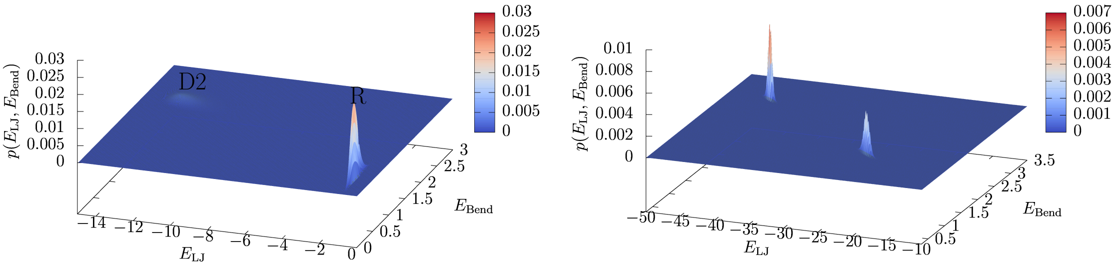

Figure 5.26.: Two-dimensional probability distribution $p(E_{\mathrm{LJ}}, E_{\mathrm{bend}})$ for the same transitions as in Figure 5.25. In contrast to the one-dimensional probability distribution the suppression between both phases is much deeper. Note that the peak height of the two phases are not identical, but the enclosed volumes of each peak are.

soon as the cost in terms of bending energy is balanced by the gained Lennard-Jones energy. In the ground state ($T = 0$) the polymer tries to maximize the number of neighbors per monomer located close to the minimum of the Lennard-Jones potential ($r_{\mathrm{min}} = 2^{1/6}$). For the one time bent polymer this means that every monomer has two adjacent monomers with distance close to r_{min}. Within the approximation that the whole polymer lies in a plane the gained Lennard-Jones energy is roughly given by

$$\begin{aligned} E_{LJ}^{\mathrm{gain}} \approx \sum_{i=2}^{N-1} (N-i) * (\frac{1}{i^{12}} - \frac{1}{i^{6}}) + 4\epsilon \sum_{i=2}^{2i<N+1} O_{\mathrm{os}}(i) \\ - (N-2) * \epsilon + 4\epsilon \sum_{i=2}^{2i<N} O_{\mathrm{ss}}(i) \end{aligned} \qquad (5.2)$$

where

$$O_{\mathrm{ss}}\left(i\right) = \left(N - 2i + N \bmod 2\right) \left(\frac{1}{i^{12}} - \frac{1}{i^{6}}\right)$$

$$O_{\mathrm{os}}\left(i\right) = \left(N - 2i + 1\right) \frac{1 - \left(r_{\mathrm{min}}^{2} - \frac{1}{4}i + i^{2}\right)^{3}}{\left(r_{\mathrm{min}}^{2} - \frac{1}{4}i + i^{2}\right)^{6}},$$

with O_{ss} is the Lennard-Jones energy of monomers located on the same strand, and O_{os} the Lennard-Jones energy from monomers of the opposite strand. The factors in front of $O_{\mathrm{ss}}/O_{\mathrm{os}}$ just count the number of these monomers. The energy cost of the bending is approximately given by $E_{\mathrm{bend}} \approx 2.0\kappa$. Due to the fixed bond length the formula (5.2) is not exact, but it gives a reasonable approximation for κ_R. For the simulated systems these values are $\kappa_R \approx 6.8$ for $N = 14$, $\kappa_R \approx 16.53$ for $N = 28$ and $\kappa_R \approx 25.56$ for $N = 42$ and consistent with the observed data. If hairpins or toroidal states come into play the bending energy is larger, therefore the above calculated κ_R is only a lower bound. A more elaborate calculation of these low-energy states considering the toroidal states can be found in [44].

5.2.5. Thoughts on the Thermodynamic Limit

Besides the flexible case, where the behavior in the thermodynamic limits is known [82, 99, 113], it is very dependent on the value of κ what happens when the length of the polymer increases. It is relative clear that the elongated/rod-like phase persists for the infinite chain. At a certain temperature the entropy should always dominate the conformational behavior and the system is above any collapse transition. It is also plausible, that the purely knotted pseudo-phase vanishes for longer chains. For a stable knot, both termini have to be located outside the collapsed chain. If not, a small perturbation would lead to a change of the knot type. This condition gets unlikely for a non-stretched conformation when the chain length increases. Nevertheless, even if the termini are located somewhere inside the collapsed polymer and thermal fluctuation would change the identified knot type, the resulting distribution of knots will be narrow and would be dominated by a few different knot types and thus different from the knots found in the coiled or globular phase.

In principle, some kind of structured phases should persist in the thermodynamic limit for the following reason: The existence of these phases depends on the competition of the interaction between all monomers (Lennard-Jones energy) and the interaction between neighboring monomers (bending energy). If the Lennard-Jones energy dominates the bending energy completely, the polymer is in the thermodynamic limit either globular or frozen. One may argue that the Lennard-Jones energy has N^2 contribution and the bending energy only N and so for $N \to \infty$ the Lennard-Jones energy always win. But this is not true, since as long as the interaction potential between all monomers decreases faster than $\frac{1}{r^3}$ (in three dimensions) one find always a cutoff radius r_c at which all more distant monomers can be neglected in average. Thus, both energies scales with N and one can find a finite κ for which both energies are in competition for sufficient long chains. However, this κ may be so large, that no real polymer would fit to such a coarse-grained polymer.

6. Stabilizing and Destabilizing Effects of Spherical Confinement

6.1. Introduction

The investigation of confined polymers is a long-standing field in polymer science and is related to many open questions. Already de Gennes described the scaling behavior of the free energy of confined polymers in slits or pores (one and two-dimensional confinement) [23]. There are many recent works investigating these and similar problems, see References [45, 80, 90, 91]. In particular, References [90, 91] give a good theoretical overview of the scaling of the free energy of confined chains in slits (two-dimensional confinement), pores (one dimensional confinement), or spherical cavities (three-dimensional confinement). Especially, the third kind plays an important role in all kind of delightful tricks of nature. It ranges from chaperon-mediated protein folding [42, 120], and DNA packing in viral capsid into a host cell [5, 6, 20, 21, 31, 48, 78, 87], over subsequent modulation of amyloid formation [4, 41], to entropic segregation [7, 40, 54].

The influence of this kind of confinement on the structural properties and the thermal response of polymers could be delightful. Taking only flexible self-avoiding polymers into account, one can already show that spherical confinement differs qualitatively from cylindrical or planar confinement, by scaling analysis of the free energy [19]. In [91] Sakaue and Lutjen suggest by mean-field approaches, that flexible polymers exhibit two regimes in spherical confinement: a fluctuating and a semi-dilute Θ-solvent regime. Similar to semiflexible polymers which show a richer phase diagram with more subregimes [90]. In particular, in the stiff limit there are many recent computational studies employing Gõ-like [1, 37] or similar models which show that a three-dimensional confinement stabilizes the functional state of proteins. There are plenty studies [35, 62, 86, 106, 121] showing that chaperon-like confinements increase the folding transition for different proteins, for example using a SH3, β-hairpin or β-barrel protein. On the other hand the stabilizing nature is at least unclear and seemingly model or even solvent dependent, see Reference [69]. In a preliminary study [73] we have seen a shift of the collapse transition of a flexible polymer to lower temperatures induced by the spherical confinement.

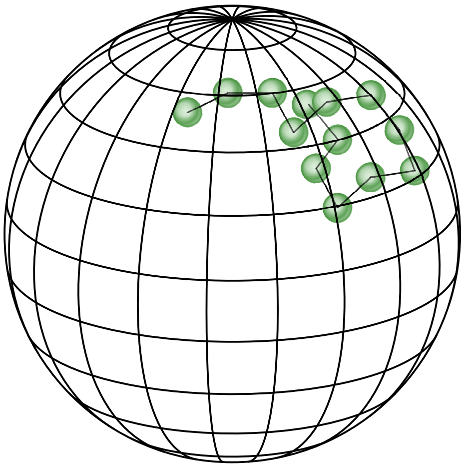

Figure 6.1.: A bead-stick polymer inside a hard sphere.

6.2. The Bead-Stick Model inside a Sphere

To investigate this behavior in more detail the coarse-grained polymer already known from the first chapter is considered. This model describes an entire class of semi-flexible polymers, thus suitable to shed light on the interplay of the attraction and stiffness in confinement. The spherical confinement is a sphere with radius R, see Figure 6.1, thus the Hamiltonian can be written as:

$$H = E_{\mathrm{LJ}} + E_{\mathrm{bend}} + V_{\mathrm{Sphere}}, \tag{6.1}$$

where E_{LJ} identical to (4.1), E_{bend} identical to (4.2), and V_{Sphere} defined by

$$V_{\mathrm{Sphere}} = \begin{cases} 0, & r_S \leq R \\ \infty, & \text{else} \end{cases}, \tag{6.2}$$

where r_S is the distance of a monomer to the center of the sphere.

In the flexible limit this is a decent model for simple linear synthetic polymers, such as sufficiently long polyethylene chains. When increasing the stiffness, its behavior get more in the direction of biopolymers. As I have shown in the first section, the interplay between the stiffness and the short range attraction leads to a rich structural phase space, see also References [72, 97, 122].

Since I am interested in the stabilizing or destabilizing effects of the confinement I will identify the collapse transition by observables measuring the elongation of the polymer, primarily the squared radius of gyration $\left\langle R_g^2 \right\rangle$ as defined by (3.5), its thermal derivation $\frac{d}{dT}\left\langle R_g^2 \right\rangle$, the end-to-end distance as defined by (3.2), and its thermal derivation $\frac{d}{dT}\left\langle R_{ee}^2 \right\rangle$. However, the identification of the collapse transition temperature and its classification is backed up by the measurement of $\varkappa^2$, b, c, see equations (4.8), (4.11), and (4.12), and a microcanonical analysis.

The canonical equilibrium estimates are obtained from histogram reweighting, see sec. 9.2.3, of two-dimensional replica-exchange Monte Carlo simulations, see section 9.2.2, running parallel in temperature T and stiffness κ. Since this means exploring a three-dimensional parameter space, T, κ, and R, the simulations are restricted for the longer polymers to a subset of κ values.

6.3. Influence of the Sphere Radius onto the Pseudo-Phase Transitions

6.3.1. Flexible Polymer

This chapter starts by discussing the influence of the confinement on a totally flexible homopolymer, which was also the first study done for this thesis. Using a more simple but also more generic model I wanted to understand why and how a sphere could stabilize proteins as reported in [35, 62, 86, 106, 121].

The behavior of a flexible homopolymer is recapped in Fig. 6.2, where the peak in $\frac{d}{dT}\left\langle R_g^2\right\rangle$ signals the second-order like collapse transition and the peaks in $\frac{d}{dT}\left\langle E/N\right\rangle$ locate the freezing transition and other solid-solid transitions within the frozen phases. For the later analysis the solid-solid like transitions are neglected. These are on the one hand very model dependent, even a slight change of the number of monomers N could completely change the number of the frozen pseudo-phases and the form of the polymers in these phases. On the other hand, to simulate these solid-solid like transitions correctly, the already computationally demanding simulations would be even more computationally demanding.

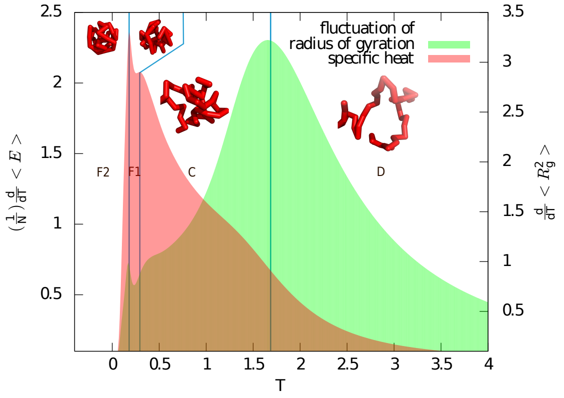

Figure 6.2.: Thermal derivative of the energy and squared radius of gyration of a free 28mer without bending stiffness ($\kappa = 0$). The lines indicate the pseudo phase transitions between the de-collapsed/extended (D), collapsed/globular (C), and frozen (F1, F2) phases.

Figure 6.3 shows the polymer extension in terms of the squared radius of gyration for $N = 14$ and $N = 42$ for different radii of the sphere including the free case. Of course, as smaller the sphere gets as smaller the polymer is extended, the sphere obviously restrict the size of the polymer by an effective repulsive force. However, with decreasing temperature the polymer continuously contracts into the collapsed/-globular pseudo-phase. The behaviour of the globular pseudo-phase does not change considerably compared to the free case, only its size is slightly influenced by the size of the sphere. Although the confinement has no major influence on the size of the polymer within the frozen phases, it may influence the ground-state-like conformation of the polymer in the frozen phase. This is visible in the squared end-to-end distance which differs for different sphere radii at very low temperatures, see inset in Figure 6.3. A small perturbation in this frozen phase, like the change of the size of the sphere, leads to a different orientation of the termini of the polymer and thus to a different end-to-end distance.

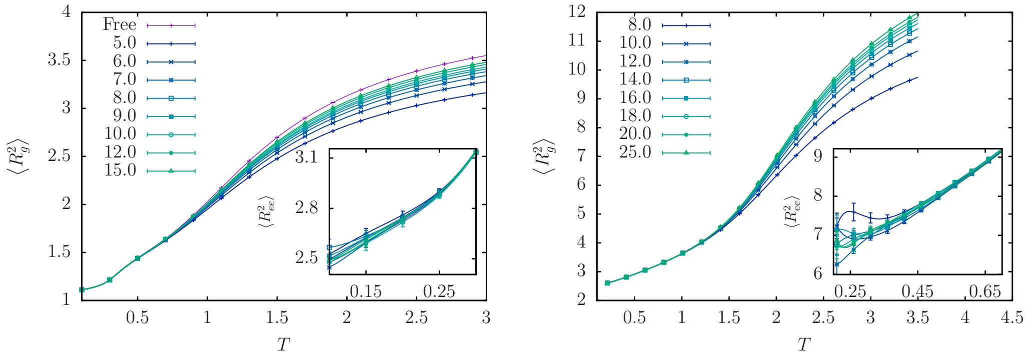

Figure 6.3.: Squared radius of gyration for a 14mer (left) and a 28mer (right) for different sphere radii. The insets show the squared end-to-end distance of these polymers for the frozen phase. The size of the polymer, in terms of $\left\langle R_g^2 \right\rangle$, is almost independent of the confinement size for the frozen phase. On the other hand the squared end-to-end distance starts to differ for very low temperatures where the polymer goes into ground-state-like conformations.

What indeed changes is the location of the collapse transition temperature $T_\Theta^N(R)$, see Figure 6.4. The peaks in $\frac{d}{dT}\left\langle R_g^2 \right\rangle$ shrink, become broader, and shift to lower temperatures as R decrease until R is so small that the difference between the coiled and globular pseudo-phase vanishes and hence no collapse transition is observable anymore. Which means that the collapse transition temperature decreases, in some sense the polymer is destabilized by the tighter confinement, see Figure 6.6. This is in contrast with what is reported for protein simulations, see [35, 62, 86, 106]. The decreasing radius of the confinement pushes the polymer into more collapsed conformations even above the collapse transition, thus the conformational difference between the collapsed and extended phase decreases, which explains the broader and lower peaks.

The freezing transition is only observable in $\frac{d}{dT}\left\langle R_g^2 \right\rangle$ for short polymers ($N = 14$), for longer polymers it is just a shoulder in $\frac{d}{dT}\left\langle R_g^2 \right\rangle$. However, the heat capacity,

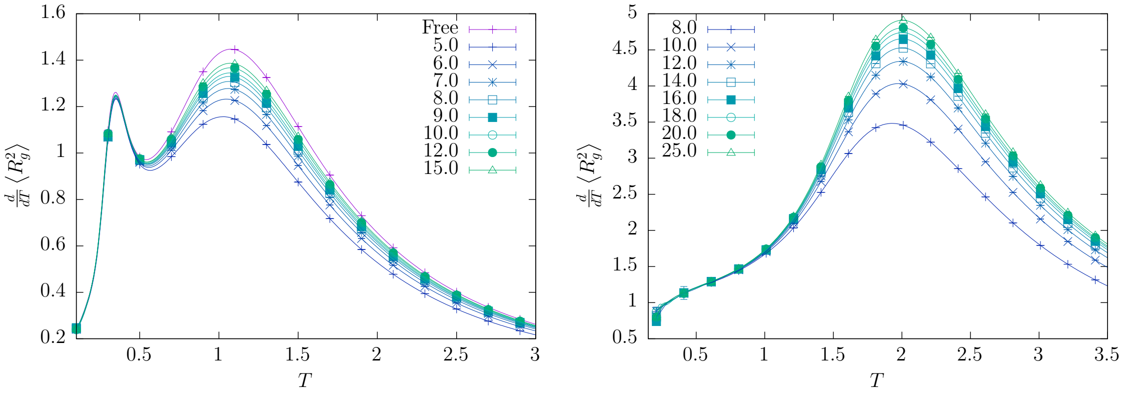

Figure 6.4.: Thermal derivation of the squared radius of gyration in dependence of the size of the confining sphere for a 14mer (left), and 42mer (right). The right peak denotes the Θ-transition where the polymer contracts from a coiled into a globular state. The left peak, if visible, signals the freezing transition.

see Figure 6.5, is ideal to identify the freezing transition. The freezing transition itself shows no systematic dependence on the sphere radius. Since the precise form of the conformation in the frozen phase may change by a change of the size of the confinement, also the freezing transition temperature fluctuate, as it is shown in Figure 6.6.

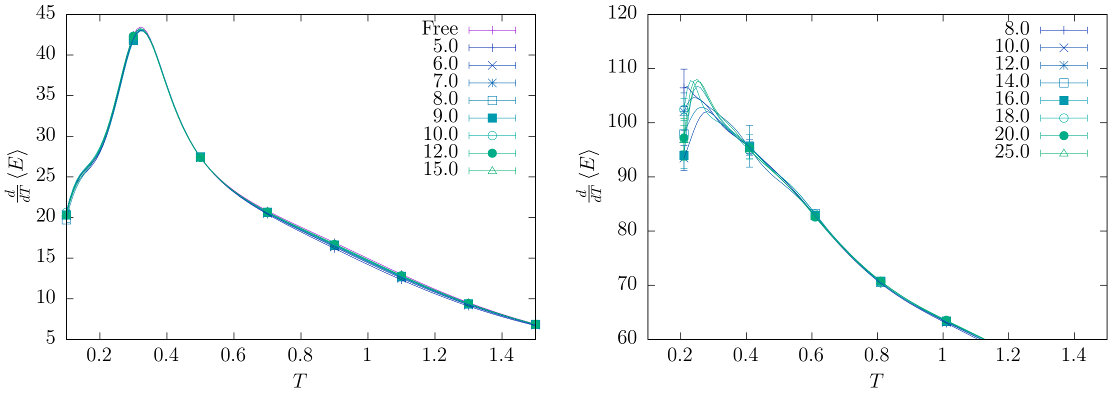

Figure 6.5.: The heat capacity $C_V = \frac{d}{dT}\langle E\rangle$ in dependence of the size of the confining sphere for a 14mer (left), and 42mer (right). The heat capacity is well suited to identify the location of freezing transition.

6.3.2. Effect of Stiffness on the Collapse Transition

The reason of the different behavior of the coarse-grained model used here and the more complex protein models could be located in the much more complex intra-protein interactions. Nevertheless, I try to find a more simple explanation. One key

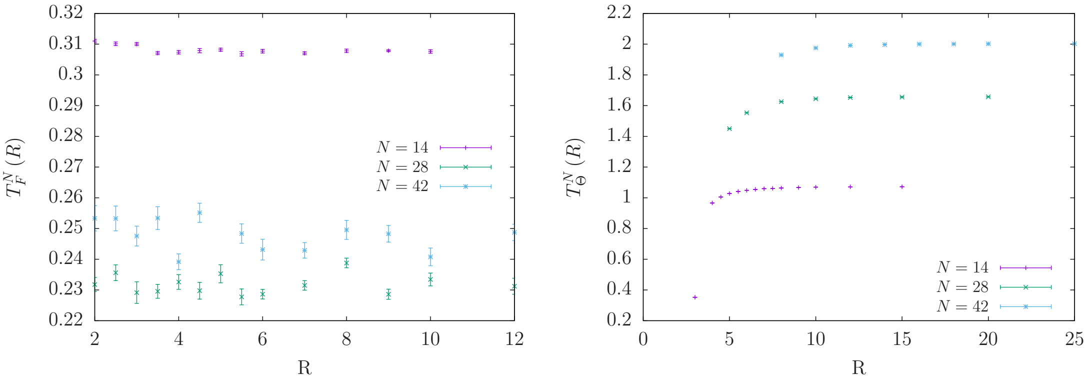

Figure 6.6.: The freezing transition temperature (left) and the collapse transition temperature (right) for some polymer lengths. There is a clear radius dependency for the collapse transition temperature, whereas the freezing transition temperature is fluctuating around some mean value for all measured radii.

difference of the bead-stick polymer and biopolymers or proteins is obviously the stiffness. Proteins are usually relative stiff objects, if compared to flexible synthetic polymers. Therefore, I present how introducing stiffness, in form of a finite κ, changes the effect of the spheric confinement on the collapse transition.

Figure 6.7 shows the elongation of the polymer by the squared radius of gyration for different κ. The intense lines represent $\left\langle R_g^2 \right\rangle$ for the unconfined case, the opaque lines represent $\left\langle R_g^2 \right\rangle$ for the same polymer but confined to a sphere or radius 8.

The confinement reduces the size of the polymer for high temperatures for all stiffnesses due to an effective repulsive force of the confinement. This effect increases with stiffness and, therefore, also how strong the confinement reduces the extension.

The low temperature extension of the polymer is barely influenced, as it was the case for the completely flexible polymer. But it may invoke different low-temperature motifs. For some κ in Figure 6.7 the canonical squared radius of gyration clearly differs between the confined and unconfined case.

Figure 6.8 shows the influence of the confinement on the collapse transition for low (left-hand) medium (middle) and high (right-hand) κ values. As long as the stiffness is low the behavior is similar to the completely flexible case, with decreasing radius of the sphere, the collapse transition temperature shrinks. This situation changes for stiffer polymers, where the spherical confinement strongly reduces the conformational entropy of only the high-temperature states. For an intermediate regime (middle column in Figure 6.8) there seems that the confinement has no influence on the transition temperature, only the peak of $\frac{d}{dT}\left\langle R_g^2 \right\rangle$ broadens and is less pronounced. However, as I will show later, there is still a measurable effect. For high κ values one can see a clear increase of the collapse transition temperature of the bent states.

For a polymer of length 28 the confinement influence is qualitatively summarized in Figure 6.9. There is a general trend for flexible polymers to be destabilized by the

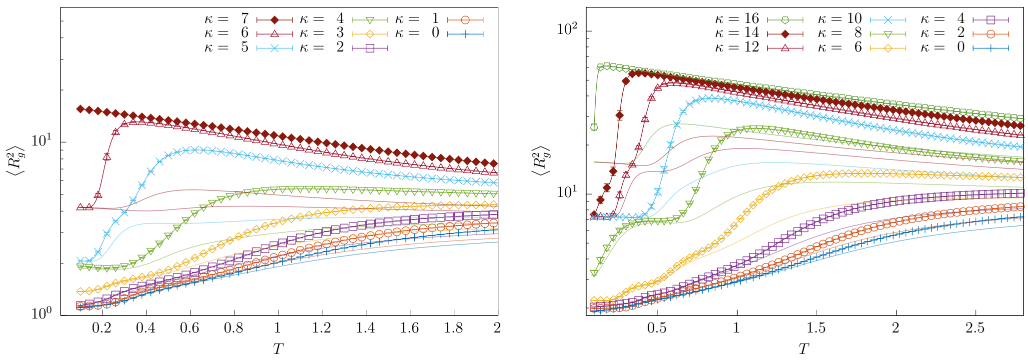

Figure 6.7.: Equilibrium extension of a single 14mer (left) and 28mer (right) in terms of the squared radius of gyration. The intense lines with error bars show the unconfined case, the opaque lines show the confined behavior for $R = 4$ (left) and $R = 8$ (right).

confinement, namely the collapse transition temperature is reduced. Towards stiffer polymers a crossover regime (for $N = 28$ around $\kappa \approx 4 - 6$) emerges, where both effects cancel each other. Interestingly, this roughly coincides with the crossover from a finite-size second-order to a first-order collapse transition in the free semiflexible polymer [125]. Still, the height and width of the peak of $\frac{d}{dT}\left\langle R_g^2 \right\rangle$ gets less pronounces and broader than in the free case. For stiffer polymers the collapse transition temperature increases and the bent states are stabilized. This effects increases with growing stiffness. Notice that the low-temperature peak in the right column in Figure 6.8 already shows the next structural transition. This transition is not directly comparable to the freezing transition of flexible polymers. The low-temperature motifs may alter through the influence of the confinement, for example the bent state of the free 28mer is a hairpin, whereas the confident polymer collapses into a toroidal state.

Similar structures have been observed recently for double-stranded DNA in confinement [104], and as a result of DNA packing into viral capsids [5, 6, 21, 31, 87]. This is consistent with the previously shown results as DNA may be modeled by a semiflexible homopolymer, where in common approximations [109] the $N = 28$ chains correspond to very short strands of about $L \approx (70 - 140)$ nm or $(210 - 420)$ base pairs in the stiffness regime $\kappa \approx 10 - 20$ for $T \approx 1$. More specifically, DNA under typical conditions shows a persistence length of $l_p \approx 50$nm. Depending on the salt concentration, the thickness d of DNA varies between 2.5nm and 5nm including screened electrostatic interactions. This thickness enters in coarse-grained models as the bead size σ. Within the discrete worm-like chain approximation one obtains $\kappa/k_BT \approx l_p/\sigma \approx 10 - 20$. The energy scale maps typical temperatures to $k_BT \approx 1$.

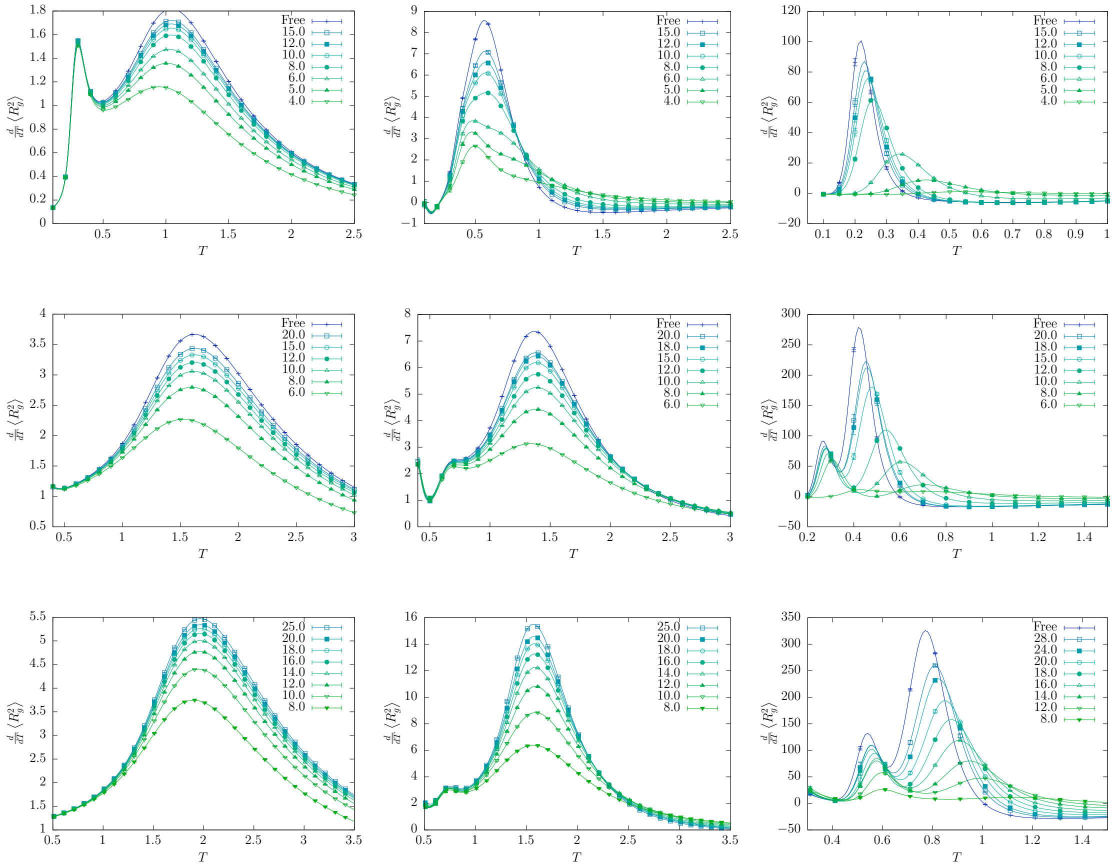

Figure 6.8.: Squared radius of gyration for a 14mer (top), 28mer (middle), and 42mer (bottom), with low stiffness (left), intermediate stiffness (middle), and high stiffness (right). Actual parameters; left top: $N = 14, \kappa = 1$, middle top: $N = 14, \kappa = 4$, right top: $N = 14, \kappa = 6$, left middle: $N = 28, \kappa = 1$, middle: $N = 28, \kappa = 4$ right middle: $N = 28, \kappa = 12$, left bottom: $N = 42, \kappa = 1$, middle bottom: $N = 42, \kappa = 6$, right bottom: $N = 42, \kappa = 16$.

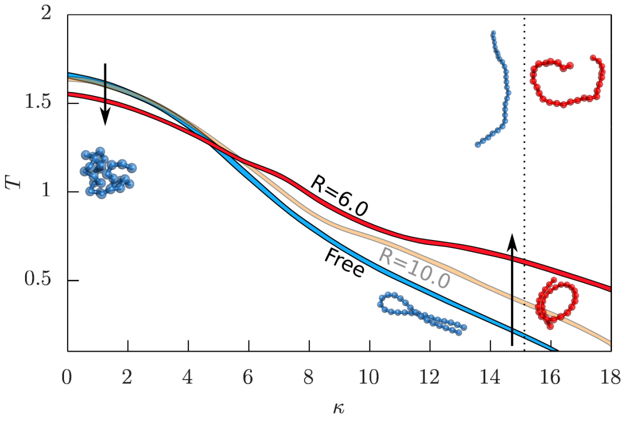

Figure 6.9.: Illustration of the stabilizing and destabilizing effect induced by the spherical confinement for a 28mer. The lines encode the location of the collapse transition, where the colors encode the size of the confinement, free case: blue, $R = 10$: orange, and $R = 6$: red. As indicated by the exemplary polymer conformations, the motif of the bent structure for high κ values may change. For the case presented here, the hairpin structure alter to a toroidal one.

6.3.3. Quantitative Explanation of the Stabilizing/Destabilizing Effect

There has been an ongoing debate on the nature of the effect of the confinement, for protein models [76, 86, 106, 121] and flexible polymers [73, 91]. As it is shown above, there are actually both stabilizing and destabilizing effects present in the same model. It appears that the shift direction is connected to the transition mechanism, where second-order characteristics lead to a destabilizing effect while first-order characteristics lead to a stabilizing effect. Still, for both cases a leading-order ansatz has been a power-law behavior of the form

$$T_\Theta(R) - T_\Theta^\infty \propto R^{-\gamma}, \tag{6.3}$$

where $T_\Theta(R)$ and T_Θ^∞ are the collapse temperature of the confined and free polymer, respectively. I start with the second-order case for flexible polymers. For a continuous transition, the confinement gradually increase the free energy at all temperatures, while the effect is higher at higher temperatures. A natural ansatz is to quantify the free-energy increase in terms of the dimensionless ratio of polymer extension and confinement size

$$\beta \Delta F \propto \left(\frac{N^\nu}{R} \right)^x . \tag{6.4}$$

This has to be extensive, i.e., for $N \to aN$ one expects $F \to aF$, while $R \to a^{1/d}R$. It directly follows that for flexible polymers

$$\beta \Delta F \propto \left(\frac{N^{\nu}}{R}\right)^{d/(d\nu-1)} . \tag{6.5}$$

In the high-temperature regime the polymer forms extended coils with $\nu = \frac{3}{5}$ (Flory approximation) such that $x = \frac{d}{d\nu-1} = \frac{15}{4}$ for a polymer in good solvent [91]. Directly at the free-polymer collapse $\nu = \frac{1}{2}$ and $x = 6$. In the globular phase $\nu = \frac{1}{3}$ and the above requirement of an extensive free-energy excess is only fulfilled for $\beta\Delta F = 0$. This is consistent with the previously shown results that the confinement barely influences the low-temperature behavior. Thus, the effect of confinement is strongest in the good solvent regime with a crossover to the Θ-point and lowest in the bad solvent regime. The finite-size transition point of a flexible polymer is energetically only signaled in a shoulder of the heat capacity, the second derivative of the free energy, $C_V = -k_B\beta^2\partial^2\beta F/\partial\beta^2$. Still, it is possible to discuss the qualitative effect of confinement onto the direction of the temperature shift: If one considers $\beta\Delta F\left(\beta\right)$ in (6.5) as a monotonic function of inverse temperature β for a fixed confinement with radius R. For $T \to \infty$ or $\beta \to 0$ there will be a constant (purely entropy-dominated) maximal modification, for $T \to 0$ or $\beta \to \infty$ there will be a vanishing modification, and consequently there has to be a gradual increase in between corresponding to a single peak in $\partial\beta\Delta F/\partial\beta$ at β^* or $\partial^2\beta\Delta F/\partial\beta^2|_{\beta=\beta^*} = 0$. Since directly at the (inverse) collapse transition temperature $\beta\Delta F|_{\beta=\beta_C^\infty} \sim R^{-6}$ is already comparably small and vanishing below, one can argue that $T^* \geq T_C^\infty$ or $\beta^* \leq \beta_C^\infty$. Then it follows that, $\partial^2\beta\Delta F/\partial\beta^2 > 0$ for all $\beta > \beta^*$ which covers β_C^∞. Thus, a confinement that modifies the free energy as $\beta F = \beta F^\infty + \beta\Delta F$ shifts the high-temperature shoulder in the corresponding heat capacity $C_V = C_V^\infty - k_\mathrm{B}\beta^2\partial^2\beta\Delta F/\partial\beta^2$ to higher inverse temperatures and thus lowers the collapse temperature.

The situation becomes clearer in the first-order regime of stiffer polymers. At the transition, the collapsed regime is in coexistence with the extended regime. One can now approximate this in a two-state model, where the system can only change between a structured state with free-energy F_s, and an unstructured state with free-energy F_u. Coexistence is then expressed in the relation $e^{-\beta F_s} = e^{-\beta F_u}$ or $0 = \beta F_u - \beta F_s$. Now, the spherical confinement essentially only influences the unstructured regime, decreasing the available entropy (and even increasing the accessible energy) which increases the free-energy $F_u = F_u^\infty + \Delta F \geq F_u^\infty$. At the same time the free energy of the structured phase is barely influenced by the confinement, $F_s \approx F_s^\infty$. Considering the temperature-independent correction ansatz $\beta\Delta F = aR^{-\gamma}$ $(a > 0)$ in the unstructured (high-temperature) regime. This ansatz is consistent with all regimes found for semiflexible polymers in spherical confinement [90] and it yields

$$0 = \beta F_u^\infty - \beta F_s^\infty + aR^{-\gamma}. \tag{6.6}$$

A Taylor expansion around the free-polymer collapse transition at β_C^∞, for which

$F_s^\infty(\beta_C^\infty) = F_u^\infty(\beta_C^\infty)$, yields

$$\beta_C(R) = \beta_C^\infty - aR^{-\gamma}/\Delta E^\infty, \tag{6.7}$$

where $\partial\beta F/\partial\beta = E$ is used. In general, thermodynamics implies that $\Delta E^\infty = E_u^\infty - E_s^\infty \geq 0$, where equality may occur for topological transitions, in which case a higher-order expansion of (6.6) is necessary. Interestingly the knotting transitions found in the last chapter show exactly such topological behavior ($E_u^\infty - E_s^\infty = 0$). Thus, one obtains for the collapse temperature a positive shift as expected. The exponent depends on the free-energy excess which for semiflexible polymers shows several regimes [90].

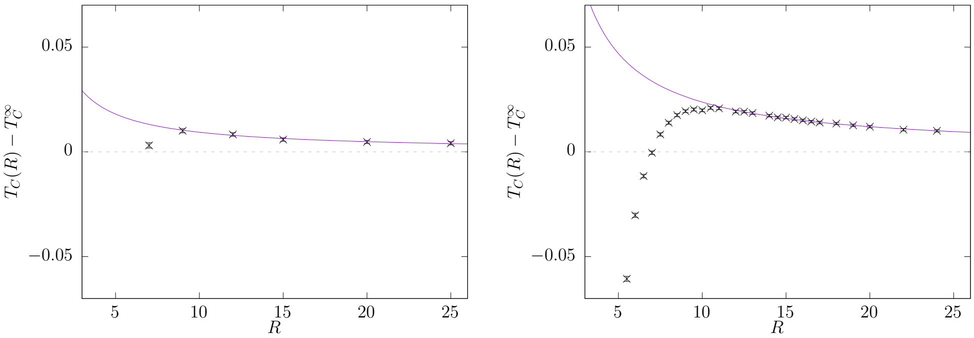

Figure 6.10.: Fit for the exponent γ for a 14mer (left) and 28mer (right) in the crossover regime ($\kappa = 4$), where for larger sphere radii the collapse transition temperature shifts to the lower and starting from a certain radius the collapse transition temperature starts to shift to higher temperature.

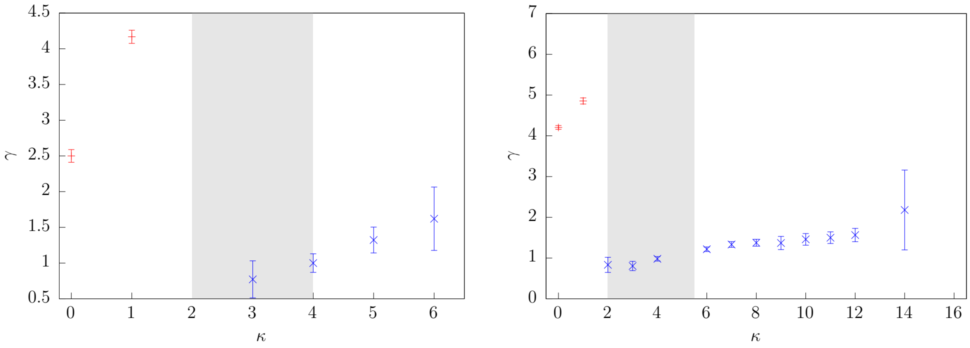

Figure 6.11.: Scaling exponent γ as a function of the stiffness κ for a 14mer (left) and a 28mer (right). Red pluses stand for a destabilizing effect $T_C(R) < T_C^\infty$ and blue crosses for a stabilizing effect $T_C(R) > T_C^\infty$. Inside the shaded area there is a crossover from an initial increase of $T_C(R)$ (large R) to a small decrease as shown in Figure 6.10.

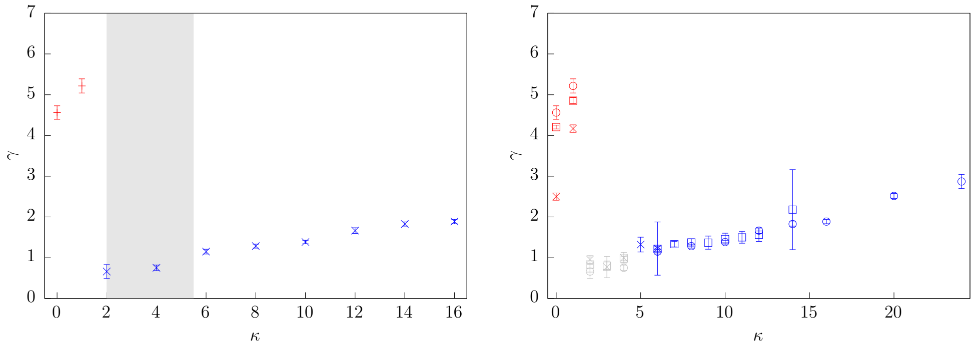

Figure 6.12.: Scaling exponent γ as a function of the stiffness κ for a 42mer (left) and for all N (right). Interestingly the value of γ seems to increase linearly with κ.

Figures 6.11 and 6.12 show a numerical verification of the above arguments, presenting the measured scaling exponent γ as a function of stiffness parameter κ. The obtained values for γ from fits to the temperature shift $T_C(R) - T_C^\infty \propto R^{-\gamma}$. The sign of the temperature shift is encoded in the color of the data symbols: stabilization (positive) is blue and destabilization (negative) is red. For flexible polymers, which collapse into a globular state, the shift is destabilizing with $\gamma \approx 4 - 5$. For stiffer polymers, the shift is stabilizing and γ seems to be linear dependent on κ. The values presented here are noticeably smaller than previous results [90, 106, 121]; one obtains $\gamma \approx 1 - 2$ with an increasing tendency from bended to hairpin-like or toroidal structures (compare [72]). These results are only consistent with the results for proteins for the highest values of κ simulated in this work. The shaded area signals a regime of crossover behavior. Here, reducing the available configuration space first leads to an increase in $T_C(R) > T_C^\infty$ (stabilizing) before a clear shift to $T_C(R) < T_C^\infty$ (destabilizing) occurs for small radii. This regime seems to cover the coil-to-globule-like regime of rather flexible polymers with a second-order like transition. Hence, it seems that the (second-order) destabilizing and the (first-order) stabilizing effect overlap, where for small sphere radii the destabilizing effect dominates.

Part II.

Advanced Monte Carlo Simulations

7. Introduction

In the last decades computer simulations have been proven to be a useful tool in physics located between theory and experiment. Of course, simulations can never perfectly mimic a real system and replace real experiments. This apparent disadvantage could be turned into an advantage in many cases. It is often valuable to ignore all kind of side effects real experiments suffer from and are cumbersome to control. Especially, observables inaccessible by experiments can be “measured” within a simulation, which can lead to an enriched understanding of the underlying mechanism. On the other hand the connection to theory, in particular statistical physics, goes in the opposite direction. In many non-trivial problems, there exists no or only approximative analytical solutions. Simulations can not only be used to check theoretical predictions on complexer models, they are also useful to connect them to real experiments. The connection to theory and experiments makes simulation a relevant and complementary method of modern physics.

There exists two different techniques to simulate microscopic models, namely molecular dynamics algorithms (MD) and Markov-Chain Monte Carlo (MCMC) algorithms. The former one uses Newtons second law to simulate trajectories of all individual constituents of a physical system in contrast to MCMC which sample random states from the equilibrium distribution. Both have advantages and disadvantages. For example, with MCMC simulations it is cumbersome, although not impossible, to obtain dynamical properties, whereas MD simulation are perfectly suited to calculate dynamical observables. On the other hand MCMC simulations are more appropriate to simulate systems over large temperature ranges or, due to its possibility to use arbitrary dynamics, to investigate phase transitions.

For MD simulation some well-established programs are available which can simulate all kinds of problems (e.g. GROMACS [84], LAAMPS [83]). Unfortunately, that is not the case for MCMC simulations. There exists many MCMC algorithm which can differ in implementation details quite a lot. Additionally, one can use arbitrary dynamics in a MCMC simulation. Often this free choice of the dynamics is crucial to cope with problems arising from slow dynamics induced by phase transitions. However, the free choice makes it very complicated to integrate various algorithms and arbitrary dynamics into a single program. This is why we decided to create a framework which enables us, and hopefully also others, to create programs tailored to a each problem.

The rest of this part of the dissertation is organized as follows:

- The eighth chapter briefly repeats some statistical mechanics prerequisites, which are necessary to understand the different MCMC algorithms.

- In chapter 9 all MCMC algorithms which are implemented in the framework are presented. First the standard Metropolis MCMC algorithm is explained. Based on this the more advanced techniques like parallel tempering, replcia-exchange and generalized ensemble algorithms are described. These techniques make it possible to use more advanced data evaluation techniques, which are also explained in this chapter.
- Chapter 10 gives an overview of the used MCMC moves. Since the first part of this thesis employs mainly models with fixed bonds, it is necessary to adopt most common moves to this constraint.
- Chapter 11 explains the principal design goals of the framework. The general structure of the framework is given and how the individual parts fit together. Also, a short explanation of some programming techniques should help a technically interested reader to understand the implementation of the framework itself. This is the only chapter where implementation details play a role.

8. Markov-Chain Monte Carlo Simulation

8.1. Statistical Mechanics Primer

This section briefly describes a few basic concepts of statistical mechanics which are necessary to understand how Metropolis Monte Carlo simulations work. For convenience only the canonical ensemble is considered, however, every presented algorithm can be applied to any ensemble. The canonical ensemble is defined as a system at constant temperature T, with constant volume V, and containing constant number of particles N in thermodynamic equilibrium. Also, for convenience the Boltzmann constant is set to one, $k_B = 1$. Thermodynamic equilibrium means that there is no net macroscopic flow of energy or matter. The system is completely defined by its Hamiltonian $\mathcal{H}$ which connects every micro state $\{S_\mu\}$ of the system with an energy $E \equiv \mathcal{H}(\{S_\mu\})$. The partition function is then given by

$$\mathcal{Z} = \sum_{\{S\}} e^{-\beta\mathcal{H}(\{S_\mu\})}, \tag{8.1}$$

where the "sum" runs over all possible states. The expectation value of any observable $\mathcal{O}$ can now be calculated via

$$\langle\mathcal{O}\rangle = \frac{1}{\mathcal{Z}} \sum_{\{S\}} \mathcal{O}\left(\{S_\mu\}\right) e^{-\beta\mathcal{H}(\{S_\mu\})}, \tag{8.2}$$

and the equilibrium probability of any microstate is defined by

$$P^{\mathrm{eq}}\left(\{S_\mu\}\right) = \frac{1}{\mathcal{Z}} e^{-\beta\mathcal{H}(\{S_\mu\})}. \tag{8.3}$$

For systems with a continuous state space all sums in the formulas above should be interpreted as integrals over the phase space. For example, considering a three-dimensional system with N particles, every state of every particle is given by its position vector $\vec{q}$ and momentum vector $\vec{p}$. The partition function reads now as

$$\mathcal{Z} = \int dp \int dq \exp\left[-\beta\left(\sum_{i=0}^{N} \frac{\vec{p}^2}{2m} + V(q)\right)\right], \tag{8.4}$$

where $V(q)$ is the potential energy in dependence of the location of all particles.

One can integrate out the momentum part which gives a partition function only dependent on the state space constructed from all possible locations of all particles

$$\mathcal{Z} = (2\pi m T)^{3N/2} \int dq \exp\left(-\beta V(q)\right). \tag{8.5}$$

One usually neglects the constant $(2\pi m T)^{3N/2}$, since Monte Carlo simulations can only determine the partition function up to a constant. However, this is unimportant since in the calculation of any canonical observable the constant cancels out.

8.2. Metropolis Algorithm

The basic idea of the Metropolis algorithm is to integrate (8.1) or (8.2) by setting up a Markov-Chain

$$\ldots \xrightarrow{W} \{S_\mu\} \xrightarrow{W} \{S_\nu\} \xrightarrow{W} \ldots, \tag{8.6}$$

describing a chain of thermodynamically equilibrated states $\{S_\mu\}$ and transition probabilities $W = W\left(\{S_\mu\} \to \{S_\nu\}\right) = W_{\mu\to\nu}$. The master equation connects now the probability of two states $P(\{S_{\mu/\nu}\}, t)$ with the transition probabilities $W_{\mu\to\nu}$ and $W_{\nu\to\mu}$:

$$\frac{dP\left(\{S_\mu\}, t\right)}{dt} = \sum_\nu \left[P\left(\{S_\nu\}, t\right) W_{\nu\to\mu}(t) - P\left(\{S_\mu\}, t\right) W_{\mu\to\nu}(t)\right]. \tag{8.7}$$

At thermal equilibrium $\frac{dP(\{S_i\},t)}{dt} = 0$, W have to satisfy the following criteria in order to create a proper Markov chain:

(I)

$$W_{\mu\to\nu} \geq 0 \quad \forall \quad \{S_\mu\}, \{S_\nu\} \tag{8.8}$$

(II)

$$\sum_\nu W_{\mu\to\nu} = 1 \quad \forall \quad \{S_\mu\} \tag{8.9}$$

(III)

$$\sum_\mu \left[P^{\text{eq}}\left(\{S_\mu\}\right) W_{\mu\to\nu} - P^{\text{eq}}\left(\{S_\nu\}\right) W_{\nu\to\mu}\right] = 0 \tag{8.10}$$

The last criteria can be replaced with the detailed balance condition

$$P^{\text{eq}}\left(\{S_\mu\}\right) W_{\mu\to\nu} = P^{\text{eq}}\left(\{S_\nu\}\right) W_{\nu\to\mu}, \tag{8.11}$$

which is a sufficient condition for (III), but often easier to prove. The transition probability can be composed into the product of the probability to choose a new state $p^s\left(\{S_\mu\} \to \{S_\nu\}\right)$ and the probability of a specific microstate $P^{\text{eq}}\left(\{S_\mu\}\right)$. This leads to the Metropolis-Hastings [43] acceptance probability of a transition

$$W_{\mu\to\nu} = \min\left(1, \frac{P^{\text{eq}}\left(\{S_\nu\}\right) p^s\left(\{S_\mu\} \to \{S_\nu\}\right)}{P^{\text{eq}}\left(\{S_\mu\}\right) p^s\left(\{S_\nu\} \to \{S_\mu\}\right)}\right). \tag{8.12}$$

Together with the Boltzmann weight of a state 8.3 and a symmetric selection probability $p^s\left(\{S_\mu\} \to \{S_\nu\}\right) = p^s\left(\{S_\nu\} \to \{S_\mu\}\right)$ this gives the acceptance probability of the Metropolis algorithm [75]

$$W_{\mu\to\nu} = \min\left(1, e^{-\beta \Delta E}\right), \tag{8.13}$$

where ΔE is the energy difference of two states $\Delta E = E_\nu - E_\mu = \mathcal{H}\left(\{S_\nu\}\right) - \mathcal{H}\left(\{S_\mu\}\right)$.

9. Advanced Monte Carlo Methods

9.1. Need for more advanced Algorithms

Unfortunately, the Metropolis algorithm, although in principle capable to simulate all kind of systems, is not sufficient to cope with problems arising from simulations of more complex systems. The generated data from MCMC simulations suffer from temporal correlations which means successive measurements cannot be treated as uncorrelated data points. The integrated autocorrelation time quantifies this effect and gives approximately the distance between two measurements which are uncorrelated. It is defined by

$$\tau_{\mathrm{int}}(\mathcal{O}) = \frac{1}{2} + \sum_{k=1}^{k_{\mathrm{max}}} A(k)(1 - \frac{k}{N}), \tag{9.1}$$

with N the number of measurements and $A(k)$ being the autocorrelation function defined as

$$\frac{\langle \mathcal{O}_i \mathcal{O}_{i+k} \rangle - \langle \mathcal{O}_i \rangle \langle \mathcal{O}_{i+k} \rangle}{\left\langle \overline{\mathcal{O}^2} \right\rangle - \left\langle \overline{\mathcal{O}} \right\rangle^2} \xrightarrow{k\to\infty} a \exp(-\frac{k}{\tau_{\mathrm{exp}}}). \tag{9.2}$$

τ_{exp} is called exponential autocorrelation time and connected with the correlation length ξ of a system:

$$\tau_{\mathrm{exp}} \propto \xi^z, \tag{9.3}$$

where z is the so called dynamical critical exponent. Close to criticality the correlation length diverge, $T \to T_C \Rightarrow \xi \to \infty$. For finite system at criticality the correlation length is replaced by the system size, which leads to the following scaling for τ_{exp}:

$$\tau_{\mathrm{exp}} \propto L^z \tag{9.4}$$

For the Metropolis algorithm with local updates z is rather large and close to two. This means the needed computing time for the same amount of uncorrelated data increase quadratically with the system size. This effect is called critical slowing down. For system with local interactions the computing time of a single measurement itself increase at least linear with the system size N, which leads to a total computing time

t scaling at least with

$$t \propto N^3, \tag{9.5}$$

at second-order phase transition. For first-order phase transition an even worse scenario kicks in [53]. The autocorrelation time scales exponentially with the system size

$$\tau_{\mathrm{exp}} \propto \exp(2\sigma L^{d-1}), \tag{9.6}$$

where d is the dimensionality of the system and σ denotes the interface tension between the two coexisting phases of the first-order phase transition. This effect is sometimes called supercritical slowing down.

Both, the critical slowing down and the supercritical slowing down, enforces the usage of advanced algorithm techniques in order to simulate larger systems. Especially for system with strong first-order phase transition large can mean rather small system sizes, less than 20 particles are sufficient in some cases to bring modern computers to its limitations [77].

9.2. Parallel Tempering Simulation

The idea of the parallel tempering algorithm [36, 49, 103, 105, 117] is to simulate m replicas of the system in parallel. Each of them at a different temperature $T_1, T_2, \ldots, T_m$. The difference to the standard Metropolis algorithm is that the individual replicas exchange their states between each other every now and then. Thereby, states from temperatures with low autocorrelation times (fast dynamics) are exchanged with these from temperatures which suffer from large autocorrelation times, which is typical close to phase transitions or at low temperatures. Conceptually, the simulation avoids the suppressed regions in the phase space and walk around the regions where standard Metropolis simulations suffer from slow dynamics.

The exchange of the state of two replicas has still to satisfy the detailed balance constraint (8.11). To construct the right exchange probability one starts with the combined partition function of all replicas:

$$\mathcal{Z}_{\mathrm{PT}} = \prod_{i=1}^{m} \mathcal{Z}(\beta_i) = \prod_{i=1}^{m} \sum_{\{S_\mu\}} \exp(-\beta_i H(\{S_\mu\}) \tag{9.7}$$

Now one can adept the Metropolis criteria on (9.7) and get the following acceptance probability W that two replicas at β and β', with states $\{S_\nu\}$ and $\{S_\mu\}$ and their

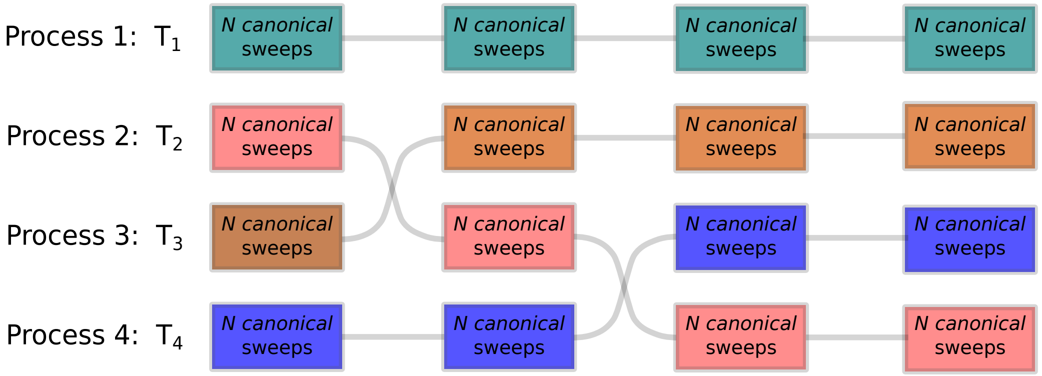

Figure 9.1.: Flow of the states (different colors) of a parallel tempering simulation with 4 different temperatures.

corresponding energies $E_x = H(\{S_x\})$, are swapped

$$
\begin{aligned}
W_{\nu\leftrightarrow\mu} &= \min\left(1, \frac{e^{-\beta E_\nu} e^{\beta' E_\mu}}{e^{-\beta E_\mu} e^{\beta' E_\nu}}\right) \\
&= \min\left(1, e^{-\beta(E_\nu - E_\mu) - \beta'(E_\mu - E_\nu)}\right) \\
&= \min\left(1, e^{\Delta\beta\Delta E}\right) . \qquad (9.8)
\end{aligned}
$$

This generates a flow of states of the individual Metropolis simulation through the temperature space, see Figure 9.1.

To ensure that the update probability for exchanging two replicas is reasonably high, their temperatures should be so close that their canonical probability distributions $p(E)$ overlap sufficiently well. A possible spacing for T_i could be equal spacing, which in most cases lead to sufficient result. Nevertheless, much more refined techniques were developed, see References [14, 58], which optimize the choice for T_i to maximize the flow between the different replicas. However, for complicated system and a large temperature range it is more expensive to find such an ideal spacing compared to a uniform distributed spacing where the temperatures are close enough such that all replicas have a sufficient exchange probability.

Another advantage of the parallel tempering method is that it is agnostic to the underlying simulation method. As long as the technique which simulate the individual replicas produce well equilibrated states, one can adept parallel tempering to it. In principle, it is even possible to use different update moves in different replicas. In practice, it is more common to use identical moves, but adjust their update ranges for every temperature. An easy improvement is to use smaller update ranges at lower temperatures to get an equivalent update probability over all temperatures. This can be easily achieved by applying the ARM method, see section 10.0.5, to adjust the update ranges of the individual temperatures within the thermalization procedure.

Although parallel tempering has many advantages, some weaknesses of the underlying Metropolis algorithm remain. The canonical simulation will not sample the suppressed regions of the phase space occurring at first-order phase transition. So examining the free energy barrier would still be error prone. Also, at low temperatures the canonical histograms will become very narrow, such that the number of necessary replicas increases strongly while lowering the temperature.

9.2.1. Data Evaluation for Parallel Tempering

A proper parallel tempering simulation produce for every simulated temperature an equilibrated time series from which canonical measures for every temperature can be calculated by taking the mean value of an observable

$$\langle O_\beta \rangle = \sum_{i=1}^{N} O_i, \tag{9.9}$$

where N is the number of measurements and O_i is the value of an observable at step i of the simulation. But one can do much better, it is possible to obtain results over a range of temperatures from single canonical simulation at $T_0 = \frac{1}{\beta_0}$. Given the not normalized histogram $H_{\beta_0}(E)$ measured during a simulation at β_0, one can easily calculate the not normalized histogram at any other temperature by

$$H_\beta(E) \propto \Omega(E) e^{-\beta E} = \Omega(E) e^{-\beta_0 E} e^{-(\beta-\beta_0)E} \propto \Omega(E) e^{\Delta\beta E} \tag{9.10}$$

Based on (9.10) we can calculate the expectation value of any observable $\mathcal{O}$ via

$$\langle O \rangle_\beta = \frac{\sum_E O(E) H_\beta(E)}{\sum_E H_\beta(E)} = \frac{\sum_E O(E) H_{\beta_0}(E) e^{-(\beta-\beta_0)E}}{\sum_E H_{\beta_0}(E) e^{-(\beta-\beta_0)E}}. \tag{9.11}$$

This technique is called histogram reweighting and was first proposed in [92] and the first time successfully applied by Ferrenberg and Swendson in [28, 29]. Theoretically, one can reweight the results from any temperature to any other temperature. In practice, however, the measured $H_\beta(E)$ is only an estimation suffering from statistical errors. Therefore, the reweighting range which gives proper results is restricted to those temperatures which canonical distribution have a sufficient overlap with the distribution of the simulated temperature.

The reweighting can also be based on the time series instead of the histograms obtained by a canonical simulation at β_0. The mean value is then given by the weighted sum over the time series.

$$\langle O \rangle_\beta = \frac{\sum_i O_i e^{-(\beta-\beta_0)E_i}}{\sum_i e^{-(\beta-\beta_0)E_i}}, \tag{9.12}$$

where O_i is the value of the observable O at time step i and E_i the corresponding value of the energy. In comparison to histogram reweighting, timeseries reweighting is computational more demanding but it does not suffer from discretization errors in the case one applies it to systems with a continuous state space.

9.2.1.1. Weighted Histogram Analysis Method

The single histogram reweighting techniques can only reweight the results from one simulation. Of course, it would be nice to simultaneously use all canonical measures of a parallel tempering simulation to calculate one result for the whole temperature range. This can be achieved by the weighted histogram analysis method (WHAM) [66], sometimes also called multiple histogram reweighting. Starting with m histograms $H_i(E)$ measured at β_i, every one of them with N_i measurements, one can construct the density of states $\Omega(E)$ and thus calculate expectation values for any observable $\mathcal{O}$ over a range of temperatures. The individual histograms do not have to come from a parallel tempering simulation, m individual Metropolis simulation would be also adequate. The energy distribution at β_i is given by

$$p_i(E) = \frac{H_i(E)}{N_i} \tag{9.13}$$

and its error by

$$\sqrt{\sigma^2(p_i(E)))} = g_i(E) \left\langle p_i(E) \right\rangle , \tag{9.14}$$

with $g_i(E) = 1 + 2\tau_i(E)$ and $\tau_i(E)$ the integrated autocorrelation time of the energy bin $H_i(E)$ of the ith simulation. Furthermore, we assume that the generated histogram bins are uncorrelated, $\tau_i(E) = 0$. This is, of course, not true, but as only the ratio of $H_i(E)$ with $H_{i-1}(E)$ is important for calculating $\Omega(E_i)$ and both have very similar $\tau_i(E)$, setting $\tau_i(E) = 0$ does not considerably reduce the accuracy of the result. So we assume that the error of $p_i(E)$ is approximately given by $\sqrt{p_i(E)}$. The density of states $\Omega(E)$ estimated from a single simulation is given by

$$\Omega(E) = \frac{p_i(E) e^{\beta_i E}}{Z_{\beta_i}}, \tag{9.15}$$

with the unknown partition function Z_{β_i} as normalization factor. Now one can construct the error weighted combined density of states

$$\Omega(E) = \frac{\sum_{i=1}^{m} p_i(E)}{\sum_{i=1}^{m} N_i Z_{\beta_i}^{-1} e^{-\beta_k E}}. \tag{9.16}$$

Z_{β_i} is still unknown, but can be determined iteratively via

$$Z_{\beta_i} = \sum_E \Omega(E) e^{-\beta_i E} = \sum_E e^{-\beta_i E} \frac{\sum_{k=1}^{m} p_k(E)}{\sum_{k=1}^{m} N_k Z_{\beta_k}^{-1} e^{-\beta_k E}} \tag{9.17}$$

up to an additive constant. One repeat the calculation of $\Omega(E)$ and Z_{β_i} until the difference of the consecutive Z_{β_i} is lower than some threshold. The additive constant does not influence the calculation of the canonical measure of an observable calculated via

$$\langle O\rangle_\beta = \frac{\sum_E O(E)\Omega(E)e^{-\beta E}}{\sum_E \Omega(E)e^{-\beta E}}. \tag{9.18}$$

By using $\Omega(E)$ it is also possible to calculate the first and second derivative with respect to temperature of an observable $\langle O\rangle$ and thus search for maxima and minima of the first thermal derivation which gives rise to a phase transition.

$$\begin{aligned}\frac{d}{dT}\langle O\rangle =& \beta^2\langle O\rangle\langle E\rangle - \langle OE\rangle \qquad (9.19)\\ \frac{d^2}{dT^2}\langle O\rangle =& 2\beta^3(\langle O\rangle\langle E\rangle - \langle OE\rangle)\\ &+\beta^4(\langle OEE\rangle) - \langle O\rangle\langle EE\rangle\\ &\quad - 2\langle OE\rangle\langle E\rangle + \langle O\rangle\langle E\rangle^2) \qquad (9.20)\end{aligned}$$

The individual histograms H_i must overlap to in order to apply WHAM. However, this is also a condition for a successful parallel tempering simulation, and thus no further problem when applying WHAM to the data. Everything which is left is an initial guess for Z_1. The simplest approach is to start with $Z_k = 1\forall k$. A better starting point would be to start with Z_k obtained from a different method, such as the direct histogram reweighting technique [27].

9.2.2. Two-Dimensional Replica-Exchange Method

Within the parallel tempering method the canonical exchange probability (9.8) can be replaced with a weight of an arbitrary simulation at equilibrium

$$p(\mu\leftrightarrow\nu) = \min\left(1, \frac{W_k(\{r\}_\nu)W_l(\{r\}_\mu)}{W_k(\{r\}_\mu)W_l(\{r\}_\nu)}\right), \tag{9.21}$$

where $\{r\}_\mu$ is the state of a replica with the simulation weight $W_k(\{r\})$ which will be exchanged with the state $\{r\}_\nu$ of another replica with weight $W_l(\{r\})$. Therefore, it is necessary that both states have a valid weight on both replicas.

Having a system with a Hamiltonian of the following form

$$H = E_0 + \kappa E_1, \tag{9.22}$$

one can now construct a two-dimensional replica-exchange method probing the system parallel in T and κ at the same time[1]. The probability (9.21) simplifies to

$$p(\mu\leftrightarrow\nu) = \min(1, \exp(\Delta\beta\Delta E_1 + \Delta(\beta\kappa)\Delta E_2)). \tag{9.23}$$

---

[1] In general, the system can be simulated parallel in any parameter linear in the Hamiltonian. T and κ are just the ones used in the first part of this thesis.

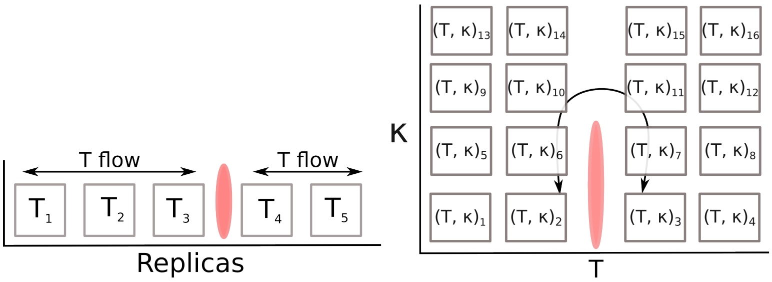

Figure 9.2.: Visualize the ability that in a two-dimensional replica-exchange simulation the wider parameter space allows overcoming barriers which hinder the one-dimensional parallel tempering to create a flow through all replicas.

Instead of having m replicas running at m different temperatures T_m, one now has m replicas running at m different parameter pairs $(T, \kappa)_m$. The two-dimensional parameter space has the advantage that it can avoid topological barriers which would hinder the flux in a one-dimensional parallel tempering simulation. In a parallel tempering simulation it can happen that there are some temperatures T_m where almost no state exchange occurs. In principle, that is also possible for the two-dimensional case, but in two dimensions the state can be exchanged in the second direction such that two points in the parameter space $(T, \kappa)_m$ can be connected by many different paths, see Figure 9.2.

Strictly speaking, it is not necessary that the Hamiltonian is of form (9.22), but the exchange probability (9.21) is more complicated, and thus more complicated to implement. Moreover, to apply a two-dimensional WHAM method a Hamiltonian of form (9.22) is compulsory.

This method was used to produce the canonical data given in chapter 5. For the bead-stick homopolymer the obvious choice for E_0 and E_1 are the Lennard-Jones energy $E_0 = E_{\mathrm{LJ}}$ and the bending energy $E_1 = E_{\mathrm{bend}}$, which gives us the ability to simulate the whole (T, κ) range at once.

9.2.3. Two-Dimensional Weighted Histogram Analysis Method

It is obvious that the two-dimensional replica-exchange method should also allow for a more elaborated analysis method which is able to reweight the simulated data to any parameter pair (T, κ). This not only allows for a very fine resolution, one can also calculate the derivation with respect to κ of any observable.

The starting point of the two-dimensional WHAM method is to measure two-dimensional histograms $H_i(E_1, E_2)$ at m different parameter pairs $(T, \kappa)_i$. The two-dimensional energy distribution is given by

$$p_i(E_1, E_2) = \frac{H_i(E_1, E_2)}{N_i}. \tag{9.24}$$

With the same assumption as for the normal WHAM method equations (9.16) and (9.17) are written as:

$$\Omega(E_0, E_1) = \frac{\sum_{i=1}^{m} p_i(E_0, E_1)}{\sum_{i=1}^{m} N_i Z_{\beta_i,\kappa_i}^{-1} e^{-\beta_i(E_1+\kappa_i E_2)}} \tag{9.25}$$

and

$$Z_{\beta_i,\kappa_i} = \sum_{E_0,E_1} e^{-\beta_i(E_0+\kappa E_1)} \frac{\sum_{k=1}^{m} p_k(E)}{\sum_{k=1}^{m} N_k Z_{\beta_k,\kappa_i}^{-1} e^{-\beta_k(E_0+\kappa E_1)}}. \tag{9.26}$$

The estimate of an observable O at any β and κ can now be calculated via

$$\langle O \rangle_{\beta,\kappa} = \frac{\sum_{E_0,E_1} O(E_0, E_1)\Omega(E_0, E_1)e^{-\beta(E_0+\kappa E_1)}}{\sum_{E_0,E_1} \Omega(E_0, E_1)e^{-\beta(H_0+\kappa E_1)}}. \tag{9.27}$$

As for the standard WHAM method one can calculate the first and second thermal derivation via (9.19) and (9.20), but also the derivative with respect to κ by:

$$\frac{d}{d\kappa} \langle O \rangle = \langle O E_1 \rangle - \langle O \rangle \langle E_1 \rangle \tag{9.28}$$

In principle, the WHAM method can be expanded to an arbitrary number of parameters, but the number of parameters is equal to the dimensionality of the problem solving the WHAM equations (9.25) and (9.26). Therefore, the complexity of the problem, and hence the computing time and necessary memory dramatically increases with the number of parameters. Even for the two-dimensional case the usual iterative method becomes very cumbersome in the case the two-dimensional histograms span a wide energy range. For the simulations using the largest parameter range in the first part of this thesis the only method which was able to effectively solve equation (9.26) was the Broyden method of second kind [18]. When applying the iterative method to thousands replicas it even failed to converge.

9.3. Generalized Ensemble Algorithms

The idea of all generalized ensemble techniques is to replace the Boltzmann configuration weights of a Metropolis Monte Carlo simulation with artificial ones

$$W(\{S(E)\}) = \exp(-\beta \Delta E) \Rightarrow \hat{W}(\{S(E)\}). \tag{9.29}$$

The configuration weights $\hat{W}$ are usually constructed such that the simulation spend equal amount of time at each energy. Thus, the simulation would act as a random walker in the energy landscape and sample all regions of the phase space sufficiently well. Especially at first-order phase transitions, this method copes with the problems arising from the double peak structure of the probability distribution $p(E)$ and thus does not suffer from the super-critical slowing down. To generate such a flat histogram the weights should be the inverse of the density of states:

$$\hat{W}(E) = \frac{1}{\Omega(E)}. \tag{9.30}$$

The resulting time series of a simulation with arbitrary weights have to be reweighted to a specific temperature in order to give valid canonical results for an observable $\langle O \rangle$. This can either be done via histogram reweighting:

$$\langle O \rangle = \frac{\sum_{E_i} H(E) O(E) \exp(-\beta E) \frac{1}{\hat{W}(E)}}{\sum_{E_i} H(E) \exp(-\beta E) \frac{1}{\hat{W}(E)}}, \tag{9.31}$$

where $O(E)$ is the microcanonical mean value of the observable O, or via time series reweighting:

$$\langle O \rangle = \frac{\sum_i O_i \exp(-\beta E_i) \frac{1}{\hat{W}(E_i)}}{\sum_i \exp(-\beta E_i) \frac{1}{\hat{W}(E_i)}}, \tag{9.32}$$

where i denote the ith step of the time series. One can reweight the results to every temperature whose canonical energy distribution is spanned by the measured generalized energy histogram $H(E)$. One question remains: How to obtain the desired weights $\hat{W}$. Since the density of states is not known in beforehand, it has to be calculated within the simulation. There are several algorithms which are able to construct these weights. The two most famous are the multicanoncial algorithm [11, 12, 16, 53] and the Wang-Landau sampling [116]. Both are implemented in our framework, but only the former one is used for the simulation of this work, and therefore explained here.

9.3.1. Multicanonical Algorithm

The idea of the multicanoncial algorithm is to start with arbitrary weights, for example $\hat{W}_0 = 1$, generate with these weight a histogram $H_0(E)$, and calculate the next weights iteratively via

$$\hat{W}_{n+1} = \frac{1}{H_n(E)}. \tag{9.33}$$

This procedure is repeated until the resulting histogram is sufficiently flat and span the desired energy range. However, this algorithm only use the generated data from the last iteration. A more sophisticated method is the recursive multicanonical iteration, which takes into account the full statistic of all iterations to generate efficiently the configurational weights. As in the former case, the recursive multicanoncial iteration starts with arbitrary weights $\hat{W}_0$ from which the first histogram $H_0(E)$ is generated. Then a statistical weight of the current run is introduced

$$p(E) = H_n(E)H_n(E+\Delta E)/\left[H_n(E)+H_n(E+\Delta E)\right], \tag{9.34}$$

and an accumulated statistical weight defined by

$$p_{n+1}(E) = p_n(E) + p(E), \tag{9.35}$$

which is initialized with $p_0(E) = 0$. The new simulation weights are then given by

$$W_{n+1}(E+\Delta E) = \frac{W_n(E+\Delta E)}{W_n(E)W_{n+1}(E)}\left[H_n(E)/H_n(E+\Delta E)\right]^{p(E)/p_n(E)}, \tag{9.36}$$

where $W_{n+1}(E)$ for one specific E can be set to an arbitrary value, since $W(E)$ is only defined up to a multiplicative constant.

9.3.2. Parallel Multicanonical Sampling

The iteration procedure of the multicanoncial algorithm can be very time-consuming. Especially, if a broad energy range (large system) is considered. This can result in wall-clock times of days or even weeks. We proposed a method which reduces the needed time drastically by using modern high-performance computing with its many cores architecture [123, 124]. The parallel multicanoncial algorithm (PMUCA) is not just a parallelization of the standard multicanoncial method, which would mean it is exactly the same algorithm just executed on many cores. Instead, it is a new algorithm, since many Markov-Chains are simulated in parallel similar to the parallel tempering algorithm.

The basic idea of PMUCA is to speed up the iteration procedure of MUCA by simulating m replicas of the system. The simulation of all replicas is done with identical weights $W_n^i = W_n$ for all $i = 1, \ldots, m$, but every with a different starting point of the Markov-Chain (every replica is initialized with a different seed for the random number generator). This leads to m different histograms $H_n^i(E)$ which are merged into one final histogram $\bar{H}_n(E) = \sum_u H_n^i(E)$ per iteration. This final histogram is now the starting point for the calculation of the next multicanonical weight W_{n+1}, either with the standard (9.33) or the recursive multicanonical (9.36) weight modification. This procedure is summarized in Figure 9.3. In practice, each replica would run on its own CPU core which does most of its work independently and only the merging of the histograms and the calculation of the new weight require communication between the individual processes. This is a perfectly suited to run PMUCA on many computers with many hundreds of CPU cores in combination. However, each replica have to equilibrate before every iteration, therefore, the maximal number of CPUs is restricted such that the equilibration time before each iteration does not dominate the simulation time.

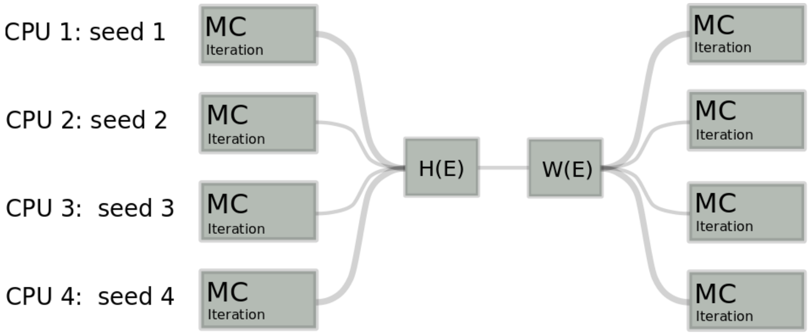

Figure 9.3.: Sketch of the parallel multicanonical algorithm. The generation of the histogram for each iteration are distributed to many processes, but the calculation of the weight itself is done only on one process and distributed to all other processes afterwards.

9.3.2.1. Performance of PMUCA

The scaling properties of PMUCA are already published in [123, 126] and only summarized here. The PMUCA algorithm is employed onto the two-dimensional Ising and q-states Potts model. Both models are often used in computer simulations as standard models to investigate new algorithms. The Ising model exhibit a temperature driven second-order phase transition and is analytical solved [60] such one can compare the simulated results with exact ones. The Hamiltonian of the Ising model is defined by $\mathcal{H} = -J\sum_{\langle i,j\rangle} s_i s_j$, where the sum goes over all spins $s \in \{0,1\}$ which are nearest neighbors and the coupling constant J is usually set to one. The q-states Potts model shows a first-order phase transition for $q \geq 5$ and one can compare the simulation with the exact known order-disorder interface tension σ_{od} given in [15]. Its Hamiltonian is given by $\mathcal{H} = -J\sum_{\langle i,j\rangle} \delta(s_i, s_j)$, where the sum is again the sum over all nearest-neighbors interactions, the spins s can have q different states $s \in \{0,\ldots,q-1\}$ and $\delta(s_i, s_j)$ is the Kronecker-Delta which is one only if two neighboring spins have the same state q.

The parallel multicanonical simulation yields correct results within the statistical errors for the heat capacity of the Ising model, see Figure 9.4, and for the σ_{od} of the 8-state Potts model obtained from the finite-size scaling of $\sigma_{\mathrm{od}}(L)$ simulated for system sizes up to 96 × 96, see Figure 9.4.

To evaluate the scaling of the performance of PMUCA two different speedup factors are considered. The first is the speedup of the wall-clock time t_p needed until the MUCA iteration is converged

$$S_p = \frac{t_1}{t_p}, \tag{9.37}$$

where t_1 is the wall-clock time needed if only one replica is used and t_p is the wall-clock time if p replicas, and therefore, p CPU cores are used. Also, the time-independent statistical speedup S^* factor which takes the total number of sweeps per core until

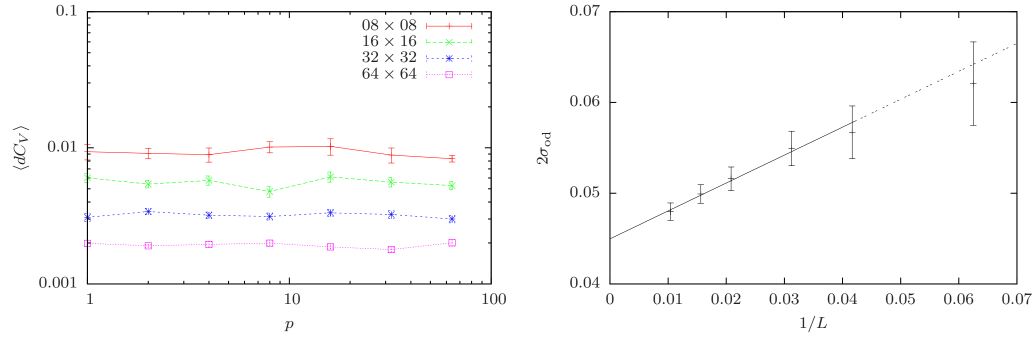

Figure 9.4.: (Left) The heat capacity for the Ising model simulated with PMUCA and the exact result from the Kaufman solution are in good agreement with each other. Shown are the difference of the analytical results with the ones obtained from the simulation. (Right) The finite-size scaling of the order-disorder interface tension obtained from a PMUCA simulation results in $\sigma_{\mathrm{od}} \approx 0.045$ which is in good agreement with [15]. Both plots are already published in [123].

convergence into account

$$S_p^* = \frac{[N_{\mathrm{iter}} M_{\mathrm{opt}}(L,1)]_1}{[N_{\mathrm{iter}} M_{\mathrm{opt}}(L,p)]_p}. \tag{9.38}$$

$[N_{\mathrm{iter}} M_{\mathrm{opt}}(L,p)]_p$ is the total number of sweeps needed until convergence for a lattice of linear size L using PMUCA with p replicas, N_{iter} is the number of iterations until convergence and $M_{\mathrm{opt}}(L,p)$ is the optimal number of sweeps per iteration such that the total amount of sweeps until convergence is minimal for the used lattice size and number of replicas. To fix $M_{\mathrm{opt}}(L,p)$ beforehand, many PMUCA simulations over a range of possible number of sweeps per iteration M are done and the M is used where the total number of sweeps is minimal. Of course, in a simulation of a complex system, where one not investigate the speedup of the algorithm, one would just chose a reasonable M and loose a bit of performance. The determination of M_{opt} would need more computer time than the simulation itself. But for a fair comparison it is necessary to search for the optimal number of sweeps per iteration.

For the Ising model the time-independent speedup of PMUCA is almost ideal, see Figure 9.5, also the scaling of S_p is ideal as long as the lattice size is larger than 28×28. For very small system sizes the communication between the replicas dominate the needed wall-clock time. Nevertheless, if the system is large or more complex than the Ising model, it is almost for sure that the simulation is dominated by the iteration process and not by the communication in between. For the Potts model PMUCA has an ideal time-independent speedup up to a certain number of replicas. As larger the system is as more replicas can be used without sacrificing performance, see Figure 9.6. The reason for that behavior may lie in the first-order phase transition with emerging barriers inducing a high integrated autocorrelation

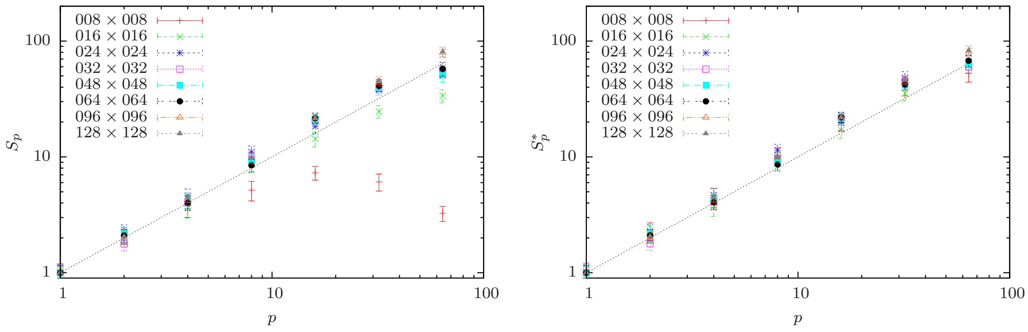

Figure 9.5.: Scaling of the performance of PMUCA method applied on the Ising model. As long as the system sizes are large enough, we found almost an ideal scaling for the statistical speedup S_p (left) as long as the system sizes are large enough. For small system sizes each iteration is so short that the communication between each replica becomes the dominant part of the simulation. Therefore, the time-independent speedup S_p^* (right) is better suited to rate the performance of PMUCA, since S_p^* does not depend on the used computer environment. Both plots are already published in [123].

time τ_i. Each replica of a PMUCA reduces the number of sweeps per replica until convergence, but only as long the number of sweeps per iteration for each replica is larger than τ_i, see Figure 9.6.

9.4. Generalized Replica-Exchange Algorithm

The replica-exchange algorithm can be generalized in terms of the underlying ensemble. Instead of using a Metropolis Monte Carlo algorithm with its canonical weight ($e^{-\beta E}$), it is also possible to use a generalized ensemble in each replica with weights $W_\kappa(E)$, where each replica uses a different set of parameters. For example, one can sample m systems, each defined by $H = E_0 + \kappa_i E_1$, where κ_i is some arbitrary parameter of replica i. Each replica does an independent multicanonical simulation to generate their weights, resulting in a flat histogram. On top of the m individual multicanoncial simulations, each replica tries every now and then to exchange its state with another replica. The exchange probability that the state S_i of a replica with weights $W_\kappa(E)$ is exchanged with a state S_j from another replica with weights $W_{\kappa'}(E)$ is given by

$$p(S_\mu \leftrightarrow S_\nu) = \min(1, \frac{W_\kappa(E\{S_\mu\})W_{\kappa'}(E(\{S_\nu\}))}{W_{\kappa'}(E\{S_\nu\})W_\kappa(E\{S_\mu\})}. \tag{9.39}$$

The advantage of this method is the possibility to circumvent suppressed regions in the phase space hidden from the total energy of the system, for example the knotting

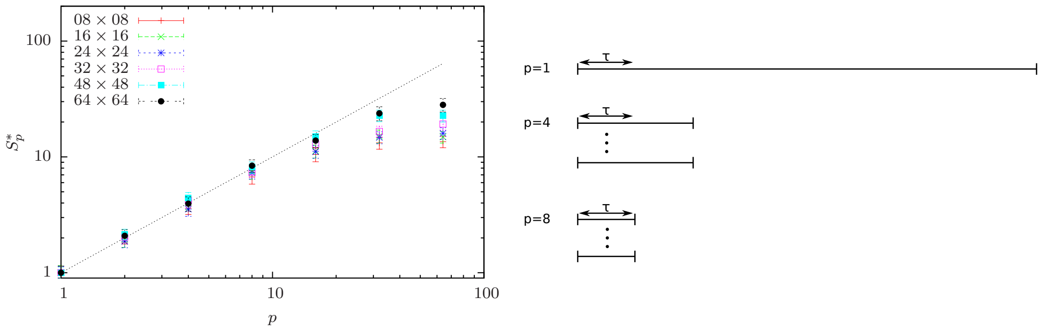

Figure 9.6.: (Left) Scaling of the time-independent speedup S_p^* for the 8-states Potts model. (Right) As long as each iteration have more sweeps per replica than the integrated autocorrelation time S_p^* scales ideal. If more replicas are used, S_p^* starts to saturate.

transitions described in section 5.2.3.

10. Monte Carlo Updates

Beside the Metropolis Monte Carlo algorithm itself, the transformation from one state in the Markov-Chain to the next one $S_\mu \rightarrow S_\nu$ is equally important to perform proper simulations. These updates have to satisfy different criteria. Furthermost, they must be ergodic (8.8), which means every possible point in phase space must be reachable, they must fulfill the detailed balance criteria (8.11) and preserve all constraints imposed by the physical system, e.g. boundary conditions or fixed lengths constraints.

Beyond those tight requirements, the set of used updates determines also the efficiency of the overall simulation. The right choice of updates is crucial to reduce the autocorrelation time of a simulation. Ideally, the updates change the conformation significantly and have an acceptable acceptance ratio at the same time. If both criteria are satisfied, the autocorrelation time could be substantively reduced. For spin-systems a cluster update even changes the dynamical critical exponent (9.3) from a value close to two for single spin flips to a value significantly smaller than one [118]. For off-lattice systems good updates are even more important due to the large degree of freedom of such systems. Although, until now, nobody has proposed an update which has been proved to solve all problems of off-lattice polymer simulations, in practice a set of different updates is sufficient to obtain proper results.

The following updates are used for the simulations done in the first part of this thesis. All these updates are not allowed to change the bond length of the polymer, which is a tight requirement and excludes many of the commonly used updates. Within the framework there are many more updates implemented, but not described here since not applicable to the bead-stick polymer.

10.0.1. Rotational Move / Pivot Move

The rotational update, illustrated in Figure 10.1, is the most simple one. It just picks one monomer at position $\vec{y}_0$ at random, choose a direction and rotates every monomer, denoted with $\vec{x}_i$, in that direction around a random axis with a random angle. To create the random axis $\vec{a}$ we need two random numbers $z \in [-1.0, 1.0], \phi \in [0, 2\pi]$. Using $\sin(\theta) = \sqrt{1.0 - z^2}$ the three components of the axis are given by

$$a_1 = \sin(\theta)\cos(\phi) \tag{10.1}$$

$$a_2 = \sin(\theta)\sin(\phi) \tag{10.2}$$

$$a_3 = z, \tag{10.3}$$

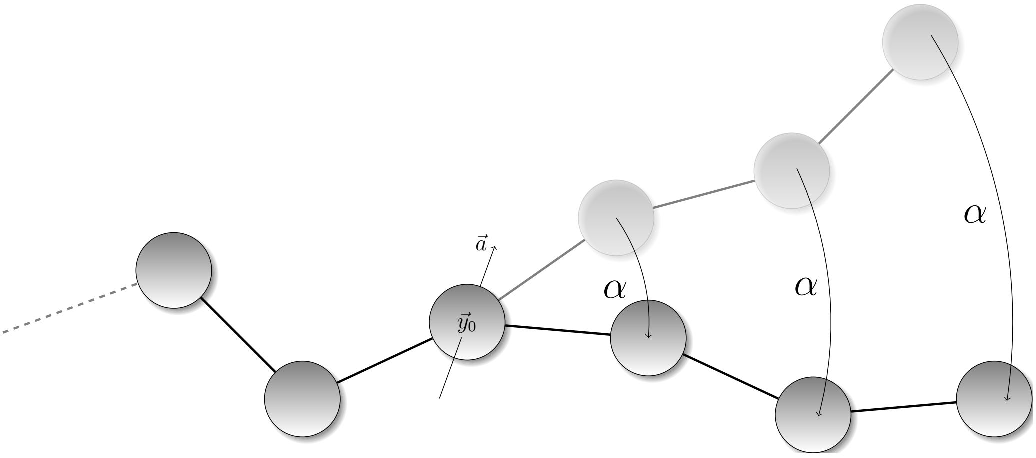

Figure 10.1.: Graphical sketch of the rotational move. One monomer $\vec{y}_0$ is randomly chosen and all following monomers are rotated around the random axis $\vec{a}$ by α.

which are by construction normalized. For the rotation one needs an additional random number $\alpha \in [0, \alpha_{\max}]$, where $\alpha_{\max}$ defines the maximal rotation angle and can be adjusted to achieve optimal acceptance ratios. The new position $\vec{x}'$ of the monomers can be calculated by using the rotation matrix $\mathbf{R}$

$$\vec{x}_i' = \mathbf{R}\vec{x}_i \tag{10.4}$$

The rotation matrix is given by

$$\mathbf{R} = \begin{pmatrix} c + a_1^2 t & a_1 a_2 t - a_3 s & a_1 a_3 t + a_2 s \\ a_1 a_2 t + a_3 s & c + a_2^2 & a_2 a_3 t - a_1 s \\ a_1 a_3 t - a_2 s & a_2 a_3 t + a_1 s & c + a_3^2 \end{pmatrix} \tag{10.5}$$

with $c = \cos(\alpha)$, $s = \sin(\alpha)$ and $t = 1 - c$. The rotational update itself is ergodic and fulfil the detailed balance condition, but to rely only on this update is probability not a good idea. Since all monomers after position y_0 are rotated by the same angle, this update induces a large change of the position of many monomers which leads to a large change in energy, and therefor to low acceptance rates if either the polymer is not in its high-temperature phase or the update angles α are not tiny. Therefore, this move should only be part of a larger move set.

10.0.2. Spherical Move

The spherical update, sketched in Figure 10.2 and described in detail in [8, 55], is similar to the rotational update and move several monomers at once. One also picks a monomer $\vec{y}_0$ at random, choosing one of its bonds, rotating only the first monomer $\vec{x}_0$ in the direction of the bond on the unit sphere. Afterwards all following monomers $\vec{x}_i$

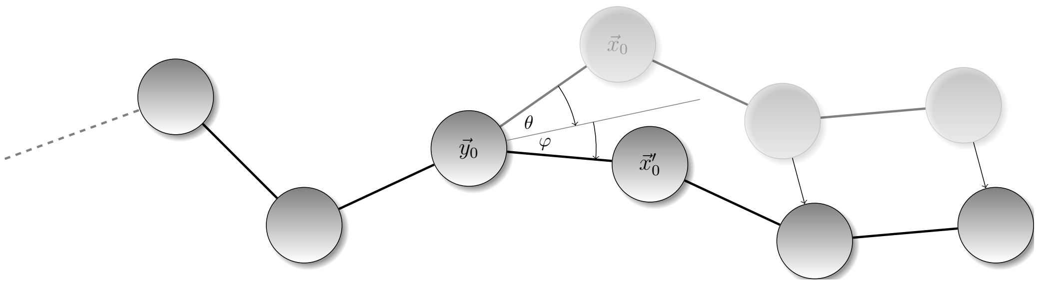

Figure 10.2.: Graphical sketch of the spherical move. First, a monomer $\vec{y}_0$ is drawn at random. One neighboring monomer $\vec{x}_0$ is then moved on the spherical cap around $\vec{y_0}$. The following monomers are shifted by $\vec{x}_0' - \vec{x}_0$ such that their relative position to $\vec{x}_0$ do not change by the spherical move.

are shifted such that their relative positions to first moved monomer are not changed. For sufficient high acceptance probabilities the unit sphere is reduced to a spherical cap with opening angle $2\theta_{\text{max}}$. To ensure detailed balance (8.11) the rotation must be equally distributed on the spherical cap $dA = \cos\theta d\theta d\varphi$. Hence, one has to draw two random numbers φ and θ, the first equally distributed in the interval $[0, 2\pi)$ and the second equally distributed out of the interval $(\cos\theta_{\text{max}}, 1]$.

If one now defines $\vec{d}$ as

$$\vec{d} = \begin{pmatrix} d_1 \\ d_2 \\ d_3 \end{pmatrix} = \vec{x} - \vec{y} \tag{10.6}$$

the new position of $\vec{x}$ is given by

$$\vec{x}' = \vec{x} + \cos\theta\vec{d} + \sin\theta\sin\varphi\frac{|\vec{d}|}{\sqrt{d_1^2 + d_2^2}}\begin{pmatrix} -d_2 \\ d_1 \\ 0 \end{pmatrix} + \sin\theta\cos\varphi\frac{1}{\sqrt{d_1^2 + d_2^2}}\begin{pmatrix} -d_1 d_3 \\ d_2 d_3 \\ 1 \end{pmatrix}, \tag{10.7}$$

if $d_1^2 + d_2^2 > 0$ and

$$\vec{x}' = \vec{x} + \cos\theta\vec{d} + \sin\theta\sin\varphi\frac{|\vec{d}|}{\sqrt{d_1^2 + d_2^2}}\begin{pmatrix} d_3 \\ 0 \\ -d_1 \end{pmatrix} + \sin\theta\cos\varphi\frac{1}{\sqrt{d_1^2 + d_2^2}}\begin{pmatrix} -d_1 d_2 \\ 1 \\ -d_2 d_3 \end{pmatrix} \tag{10.8}$$

otherwise. The conditional computation of $\vec{x}'$ is necessary due to numerical problems arising if $d_1 \approx d_2 \approx 0$. After the rotation all following monomers are shifted by $\vec{x} - \vec{x}'$, therefore their relative position to $\vec{x}$ do not change during the move.

As the rotational move, the spherical move fulfills detailed balance and ergodicity, it also touches several monomers at once, but in contrast to the rotational move the maximal displacement of each single monomer is much smaller and does not increase with the number of monomers. The downside of this move is that, although on average $N/2$ monomers are moved, only two bending angles are changed in opposite direction which leads to less effective sampling of bent conformations.

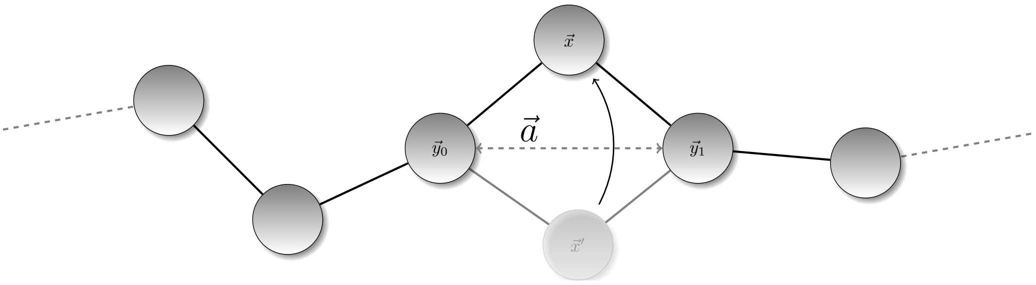

Figure 10.3.: Sketch of the crank-shaft move. The first two monomers $\vec{y}_0$ and $\vec{y}_1$ which are next-nearest neighbors are randomly chosen. Their connecting bond is used as axis for the rotation of the monomer $\vec{x}$ in the middle.

10.0.3. Semi-local Pivot / Crank-Shaft Move

The idea of the semi-local pivot or crank-shaft move is originated form lattice polymer simulations and extended to off-lattice systems. For a model with fixed bond lengths the crank-shaft move is the only possibility to change the position of only one monomer. One picks two next-nearest neighboring monomers at random and then rotate the monomer between them around the bond connecting them, see Figure 10.3. The new position of the monomer is given by equation (10.4), where the rotation axis $\vec{a}$ is defined by the bond connecting the two outer monomers. Only one random number α equally distributed in $[0, \alpha_{\max}]$ have to be drawn for this update. The maximal rotation angle $\alpha_{\max}$ is chosen from $(0, \pi]$ and can be much larger than the update ranges of the rotational or spherical move.

Since both termini of the polymer cannot change their position by this move, it is not ergodic on its own and has to be combined with either the rotational or the spherical update.

10.0.4. Bridge Moves

Bridging moves were first introduced for lattice systems [70] and later successfully extended to off-lattice systems [57, 81]. This class of moves do not change the actual position of any monomer, but rewire the backbone of the polymer. Often they are used in polydispers polymer melts where one have to be less careful on how the rewiring of different polymers should be done, but they can be also implemented for monodispers polymer melts or single polymers. These bridging moves are very helpful for very dense melts or polymers near the ground state conformation. For example, in a lattice polymer simulation where all or almost all lattice sites are occupied by the polymer, moves which change the position of a monomer are either not possible or very rare and bridging moves are the only moves which are able to generate an equilibrated conformation. Although in off-lattice system one can always move each monomer, double-bridging moves are useful to equilibrate dense conformations.

Since the polymers simulated in this work have a fixed bond length, all bridging moves for off-lattice systems given in literature will not work, because they change the

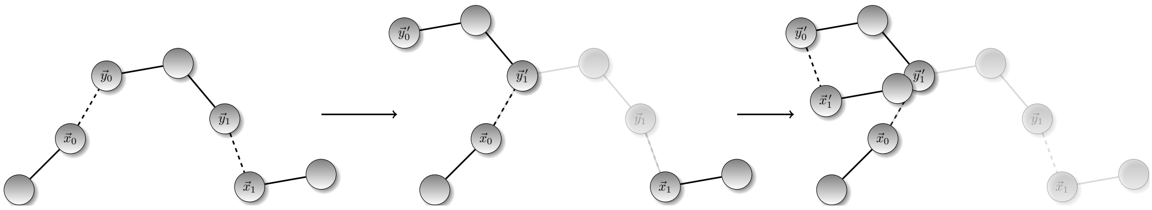

Figure 10.4.: Sketch of the double-bridging move, split in three steps. First, two random bonds $\overline{\vec{x}_0\vec{y}_0}$ and $\overline{\vec{x}_1\vec{y}_1}$ are chosen such that the polymer is divided in three parts. Then the two dangling parts of the monomer are moved, such that they are attached to the opposite monomers of the middle part and the bond length constraint is satisfied. This move substantially change the inner structure of the polymer.

bond length of the polymer. The probability to rewire the backbone of the polymer and not change a single bond length is almost zero. Therefore, the rewiring strategy has to be combined with a movement of monomers such that all bond length stay constant.

10.0.4.1. Double-Bridging Move

The idea of the double bridging move is to rewire the backbone of the polymer by exchanging two bonds. First, one chose two of them and delete them, thereby the polymer falls into three parts. These three parts are now connected by two new bonds. If there would be no bond length constraint, that would be everything one has to do. The fixed bond length implies a bit more work. Two of the separated parts of the polymer have to move such that all bonds retain constant length. It is done in the following way to ensure detailed balance, which is not quite obvious for these kinds of updates. One starts by randomly choosing two bonds given by $\overline{\vec{x}_0\vec{y}_0}$ and $\overline{\vec{x}_1\vec{y}_1}$ and delete them. Thus, the polymer fall into three parts, the first from one terminus to $\vec{x}_0$, the middle part from $\vec{y}_0$ to $\vec{y}_1$, and the last form $\vec{x}_1$ to the remaining terminus. Now, all monomers of the polymer are shifted by the same vector $\vec{d}$, such that the new position of the monomer $\vec{y}_1$ is the old position of monomer $\vec{y}_0$

$$\vec{y}_1' = \vec{y}_0 \quad \left(\vec{d} = \vec{y}_0 - \vec{y}_1\right). \tag{10.9}$$

All monomers of the dangling end, beginning with $\vec{x}_1$, are shifted by $2\vec{d}$, which means that after the move $\overline{\vec{y}_0'\vec{x}_1'}$ has the same orientation and length as $\overline{\vec{y}_0\vec{x}_0}$ before the move. A sketch of this move is given in Figure 10.4. If one applies this move twice with the same bonds, it will revert itself, therefore the detailed balance condition (8.11) is fulfilled. Although, many monomers are touched by this move, I observed a relative high acceptance probability even for the low temperature states. The move is able to change the inner structure of the polymer in one step. This is necessary if the application of many successive local moves is not sufficient to create a topological different conformation, because the probability to accept the intermediate conformations of many successive moves is very low (close to zero). For example, this is the case in a knotted conformation which first have to be untied to create another knotted conformation. The double-bridging move can do this in one move.

10.0.5. Acceptance Ratio Method

In most update moves used in Monte Carlo simulations one can adjust the update range δ which crucially influence the performance of the move. For example, setting δ to a fixed value the average energy change ΔE induced by this move is also constant. Therefore, the acceptance ratio P_{acc} goes to 0 when T approaches 0 ($P_{\text{acc}} \propto \exp(-\beta\Delta E)$). To compensate for that the update range is adjusted such that the resulting acceptance ratio is something between 20% and 50%. Often this is done manually, but employing a parallel tempering simulation with a lot of different temperatures, it is cumbersome and not very efficient to do so.

A very simple but effective approach to adjust δ is the acceptance-ratio method (ARM) described in Reference [17]. The ARM method is able to change δ on the fly, such that one can tune P to a desired value. To ensure detailed balance I use this method only during the thermalization process of the replica-exchange algorithm and keep δ fixed afterwards. I start with some initial update range δ_{old} and iteratively change it after an adequate amount of sweeps which is necessary to calculate a stable value for the current acceptance ratio $P_{\text{acc}}^{\text{old}}$ by

$$\delta_{\text{old}} = \delta_{\text{old}} \frac{\ln(aP_{\text{acc}}^{i} + b)}{\ln(aP_{\text{acc}}^{\text{old}} + b)}, \tag{10.10}$$

where P_{acc}^{i} is the desired acceptance ration and a and b are chosen such δ_{old} multiplied/divided by a factor between 5 and 10 whenever P_{acc} is 0 or 1. Often only a few iterations are necessary to achieve update ranges which gives acceptable acceptance ratios. In Figure 10.5 the acceptance ratios of the spherical move (10.0.2) after a full parallel tempering simulation of a 42mer at $\kappa = 3.0$ for different temperatures are shown. The update ranges δ are adjusted during the first 4/5 of the thermalization procedure where I try to achieve $P_{\text{acc}}^{i} = 0.3$.

10.0.6. Biased Move

The ARM method is not very suitable for a generalized ensemble simulation, since such simulations typically span a large energy range and a fixed update range δ can not be ideal for all energies. At low energies a smaller update range is necessary than for high energies to get an acceptable acceptance ratio for all energies. ARM would result in an average acceptance ratio over all energies, resulting in a too low acceptance ratio for low energies for an optimal performance. In particular, if one wants to approach very low temperatures, and thus very low energies, one needs very low update ranges at low energies. This can be achieved by making the update range energy dependent $\delta \to \delta(E)$ and chosen such that at each energy bin the update is

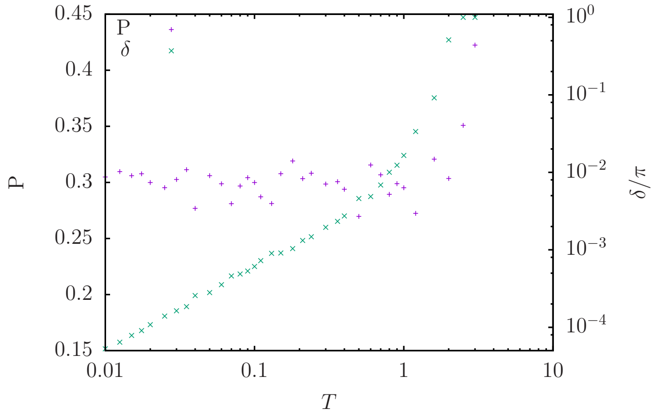

Figure 10.5.: Acceptance ratio P_{acc} and update range δ for different temperatures of a 42mer at $\kappa = 3.0$. For high temperatures the maximal possible update angle for the spherical move is reached, therefore the achieved acceptance ratio is higher than P^i_{acc}

accepted with probability 2/3, see [94]. This means the update ranges $\delta(E)$ have to be adjusted within the simulation. For generalized ensemble simulation one can tune $\delta(E)$ within the convergence procedure for the generalized simulation weights $W(E)$. After each move $\delta(E)$ will be modified by

$$\delta^{\text{new}}_{\text{max}}(E_i) = \begin{cases} (1-\epsilon)\delta_{\text{max}}(E_i) & \text{if } E_\nu \leqslant E_\mu \\ (1+2\epsilon)\delta_{\text{max}}(E_i) & \text{if } E_\nu > E_\mu \end{cases}, \tag{10.11}$$

where ν denotes the state before the update and μ the state after the update. This scheme violates the detailed balance condition (8.11), which can be easily corrected by modifying the update probability with:

$$\begin{aligned} W_{\nu\to\mu} &= \min\left(1, \frac{p(\{S_\mu\})}{p(\{S_\nu\})}\right) \to \\ W_{\nu\to\mu} &= \begin{cases} \min\left(1, \frac{p(\{S_\mu\})V_{\text{max}}(\{S_\nu\})}{p(\{S_\nu\})V_{\text{max}}(\{S_\mu\})}\right) & \text{, if } r < r_{\text{max}} \\ 0 & \text{, else} \end{cases} \end{aligned} \tag{10.12}$$

where $p(\{S_\nu\})$ is the equilibrium probability of state $\{S_\nu\}$ ($p(\{S_\nu\}) = W(E)$ for a generalized ensemble simulation), $V_{\text{max}}(\{S_\mu\})$ denotes the maximal proposed volume which depends on the used move, see Table 10.1. For all moves involving a rotation $V_{\text{max}}(\{S_\mu\})$ depends on the maximal possible opening angle $\alpha(E)$, see Figure 10.6 for $\alpha(E)$ obtained from a multicanonical simulation of a 28mer at $\kappa = 0$.

Table 10.1.: List of maximal proposed volumes for different update moves.

move	$V_{\max}(E)$
spherical move	$1-\cos(\alpha(E))$
rotational move	$\alpha(E)$
crank-shaft move	$\alpha(E)$

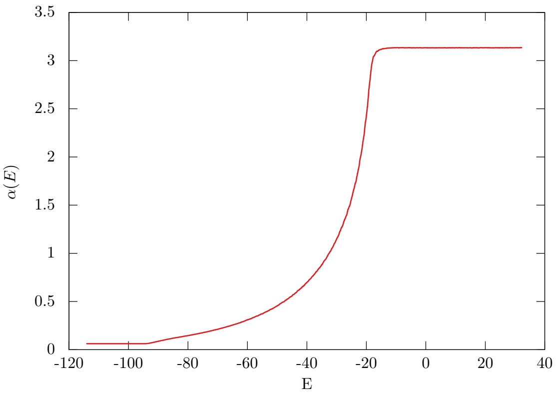

Figure 10.6.: The maximal possible update angle $\delta(E)$ for the crank-shaft move taken from a multicanonical simulation of a 28mer at $\kappa = 0$. The very small update range at low energies ensures a good acceptance rate for low energy conformations.

11. Principal Design Guidelines

As mentioned before, the variety of different MCMC algorithms and the possibility to adjust them to very different problems, from the relative simple Ising model to chemical realistic simulations of proteins, makes it nearly impossible to cover all the possibilities in a single program. The main idea of the framework is to provide a basis on which single programs can be rapidly implemented. One program for every single physical problem. Here “rapid” means both, the program should not need too much time to implement and should run as fast as possible. This is achieved, by separating the simulation in several basic building blocks with well-defined interfaces, such that different blocks can be combined to create different simulations. All MCMC simulations have three parts in common.

- The physical systems itself, which means the structure and the Hamiltonian of the system. $\mathcal{H}(\{S_\mu\}) \equiv E_\mu$, with H the Hamiltonian, S_μ a microstate and E_μ the energy of that microstate.
- The update moves, which define how to create a new state from an old one $S_\mu \to S_\nu$.
- The MCMC algorithm itself, which in the easiest case define the update probability of a suggested update move $P(S_\mu \to S_\nu)$.

These three parts correspond to three different building blocks in the framework. Each block could be exchanged with another block of the same type. For example one can test if a parallel tempering simulation yield the same results as a multicanonical without much effort. The principle to separate the simulation in well-defined blocks, does not stop at this level. For example the systems provided by the framework are composed themselves of different building blocks. One can easily change the kind of boundary condition or the used potentials or even geometrical constraints in which the system is confined to. The whole framework is written in the C++ computer programming language, which is ideal to ensures that the modularity does come with an additional cost in terms of time the program needs to run.

11.1. Implementation Details

The following section contains some implementation details and is considered for the technically interested readers. It does not contain any connection with the rest of this work and can be skipped without missing anything but technical details.

Nevertheless, I want to give a brief introduction into these details. On the one hand it is necessary to understand how the design goals were achieved, on the other hand it is also necessary to understand these techniques to use the framework itself, at least on a basic level.

The C++ programming language offers a wide variety of different programming techniques. Maybe it is the most comprehensive of all programming languages, but for sure it is one of the most complex languages. Here we only want to give an introduction in one subsection of C++, namely the template programming. These technique makes it possible to separate the framework into different building blocks without introducing any runtime overhead.

11.1.1. C++ Templates

This section briefly explain how C++ templates work. C++ templates were introduced into the language as technique to implement generic algorithms without any runtime overhead. Later it has been shown that C++ templates can be treated as own Turing-complete functional language inside C++ which is completely evaluated by the compiler during compile-time. First I will show how useful templates are to implement a generic sorting routine. If we want to sort a sequence of doubles[1], a possible function could look like the following, where the sequence of an array starting with the pointer [2] *begin and ending at *(end-1) is sorted

```
void sort(double *begin, double *end){
  \\ sort every element in [*begin, *end[
  \\ the used sorting algorithm (quicksort, bubblesort, etc.
  \\ does not matter)
  while(end != begin){
    double* new_end = begin;
    for(double* i = begin; i+1 != end; ++i){
      if(*(i+1) < *i){
        double tmp = *i;
        *i = *(i+1);
        *(i+1) = tmp;
        new_end = (i+1)
      }
      end = new_end;
    }
  }
```

---

[1] A double is a specific representation of floating point numbers on a computer.

[2] A pointer is something in a computer program which refers to (points to) a specific point in memory where something is stored. For example a pointer to a number gives the address in memory where the number is saved. Dereferencing the pointer would result in the current value of the number. A sequence of number is usually saved in continuous memory, so if we have a pointer to the first element of the sequence we can increment this pointer to reach all other elements.

```
}
```

The sort function 11.1.1 is only capable of sorting doubles in ascending order, although sorting different things would require exactly the same steps as in 11.1.1. We can generalize our sorting function to arbitrary types, as long as we know what it means that one element is smaller than the other.

```
  template <class T>
  void sort(T* begin, T* end){
    \\ T must not be a pointer to an underlying array,
    \\ it can be anything which acts like a pointer,
    \\ usually one calls T an iterator
    while(end != begin){
    T* new_end = begin;
    for(T* i = begin; i+1 != end; ++i){
      if(*(i+1) < *i){
        T tmp = *i;
        *i = *(i+1);
        *(i+1) = tmp;
        new_end = (i+1)
      }
      end = new_end;
    }
  }
}
```

Here template <class T> introduce a generic type T, which means that T can be of any type. T can be an integer number, a floating point number, or something more complex like a word or dates, as long as all operations on T are defined. The ability to sort generic data does not introduce any runtime overhead, because the compiler will an own instance of the sorting function for every requested type. Thus, the resulting compiled machine code will be the same as if one had written different sort function for every type. This is in contrast to other programming language which uses runtime polymorphism to distinguish the type of the object at the moment it is being sorted. This may not sound like a considerable issue, but if this happens in an inner loop of a function the impact, in terms of additional runtime, can be quite big. Additionally, the knowledge of the sorted type at compile time enables the compiler to optimize the resulting machine code. Summarizing, the sorting function 11.1.1 can now sort any kind of data, as long as it is defined what it means that one element is smaller than the other. We can make 11.1.1 even more generic and generalize the sorting criteria.

```
template <class T1, class T2>
void sort(T1* begin, T1* end, T2 func = less){
\\ func is a function taking two arguments of type T1
while(end != begin){
```

```
    T1* new_end = begin;
    for(T1* i = begin; i+1 != end; ++i){
      if(func(*(i+1), *i)){
        T tmp = *i;
        *i = *(i+1);
        *(i+1) = tmp;
        new_end = (i+1)
      }
      end = new_end;
    }
  }
  }
```

This sorting function can now sort any data with an arbitrary sorting criteria. For example, we can sort objects representing things like cars, geometrical shapes or operators, we just have to define what it means that one is less than the other.

11.1.2. A generic example

Our framework uses the template programming technique to provide the three basic building blocks, namely the MCMC algorithm, the system, and the MCMC moves, in a reusable way. All of them are implemented as classes, which is a way in C++ to aggregate different data and code into one addressable object. Using an instance of a system class, of an algorithm class, and at least one move class one could write a complete MCMC simulation.

```
int main(){

  PhysicalSystem System(...);
  MCMove         Move(...);
  MCAlgorithm MC(...);

  for(int i = 0; i < NumberSweeps; ++i){
    for(int j = 0; j < NumberParticles; ++j){
      MC.update(Move, /* some parameter necessary for the move */);
    }
    // measure desired observables
  }
}
```

The listing 11.1.2 could represent a complete MCMC simulation within the framework, although in a real program the for loops could look typically more complicated. Since a design goal of the framework is to be generic, one should be able to exchange every of the three basic parts without touching the two others. This set up different requirements for the individual parts. The system class needs to expose an interface to calculate the energy of the current state and to access the structure of the physical system. The listing 11.1.2 do not give a complete implementation of a system, it only gives the definition of the smallest possible interface.

```
class SimpleParticleSystem{
  public:
  // returns an iterator to the first constituent of the system
  template <class T>
  T begin();
  // returns an iterator to the last+1 constituent of the system
  template <class T>
  T end();
  // this function calculates the complete
  // energy of the current state
  double calc_energy_total();
  // this function calculates the energy change
  // if one change a particular subset of the system
  double calc_energy_subset(subset);
};
```

This interface is sufficient to implement a move class which uses the exposed interface to change the system in some way, then trigger the energy calculation which needs the less amount of work. The move itself has to expose the energy change induced by the move and a possibility to revert the move. Of course the kind of system and the move have to fit together in some way. A move designed for lattice system can not be combined with an off-lattice system. Apart from that the code given in listing 11.1.2 is agnostic to the used system, which means that for example the spherical move given in Sec. 10.0.2 for a bead-stick system could be applied to all kind of polymers.

```
template <class TSystem>
class SimpleMove{
  TSystem PointerToSystem;

  public:

  // change the system and calculating energy change
  void move(\* some parameter which defines what to move*\ );

  // will be called from the MCMC algorithm
  // if the last move was accepted
  void fix();

  // will be called form the MCMC algorithm
  // if the last move was not accpeted
  void undo();
```

```
    // returns the energy change induced by the last move
    double get_energy_change();
};
```

What's missing is a class implementing the desired algorithm. Basically the algorithm has to trigger a move and used the induced energy change to decide if this move is accepted or rejected.

```
class SimpleAlgorithm{
  public:

  template <class TMove, class ...Targs>
  void update(TMove &move, Targs... args){
    // first trigger the move
    move.move(args...);
    // get the energy change
    double energy_change = move.get_energy_change();
    // now accept or reject the move
    if ( accepted ){
      move.fix();
    }else{
      move.undo();
    }
  }
};
```

If everything is set up as in the listings 11.1.2, 11.1.2, 11.1.2 the initial goal is reached. The individual parts are decoupled and implemented in a reusable way. Of course the real implementations look more complex. For example, the more advanced algorithms uses a variety of different parameters which is recovered in a more complex interface, but the principal idea stays the same.

12. Summary

This thesis centers around three major topics: the phase-diagram of a free semi-flexible homopolymer, the effects of spherical confinement on a single semi-flexible homopolymer, and how to formalize the simulation techniques used to simulate the former two problems into a reusable framework from which new simulations can be build on.

For the majority of the simulations a coarse-grained polymer model is used, the so called bead-stick polymer. Coarse-grained means that the constituents of this model neglect many chemical details, every monomer is modeled as a single bead connected by fixed bonds to its neighbors. The stiffness is modeled via a bending potential acting on the whole backbone. On the one hand this neglects all chemical details, but on the other hand makes it achievable to simulate the polymer over a large parameter range, as it was done in this thesis.

Free semiflexible polymer: The results starts by a recap of the behavior of the free flexible homopolymer modelled via the bead-stick polymer. In case of a completely flexible polymer one observes thee different phases:

- The swollen phase (good solvent case); similar to a gas
- The globular phase (bad solvent case); similar to a liquid
- The frozen phase; similar to a solid

As expected, the collapse transition scales as was shown for other flexible polymer models as:

$$T_\Theta(N) - T_\Theta = -\frac{a_1}{\sqrt{N}} + \frac{a_2}{N}. \tag{12.1}$$

The frozen phase turns out to be very model dependent and made up of many sub-phases and metastable states. All have in common that the monomers tries to minimize the intra-polymer distance. This phase reminiscent on a glass like behavior. Due to the fixed bond length, it is not possible for the monomers to fall into the crystal like ground state usually induced by a Lennard-Jones potential.

The main topic of this chapter was a complete overview of the pseudo-phase diagram of the semiflexible bead-stick polymer consisting of 14, 28, and 42 monomers. The results are obtained by replica-exchange simulations running in parallel over the complete temperature (T) and stiffness (κ) range. Thus, more than 1000 replicas per simulation were necessary. By employing the two-dimensional histogram reweighing method it is possible to calculate canonical mean values for every parameter pair (T, κ) within the parameter range. Also, the derivative with respect to T and κ can be calculated to identify the different pseudo-phases.

The pseudo-phases found in the flexible case persists also for low stiffness in the semiflexible polymer model. For intermediate κ one find knotted pseudo-phases and for larger values of κ multiple linear strands, hairpins, and toroidal states arise. Most of these pseudo-phases can be divided in sub-phases; while lowering the temperature at constant κ the polymer contracts and thereby starts to twist a bit.

Maybe the most interesting part of this rich pseudo-phase diagram is where knotted polymers form. In the mathematical definition all closed curves which are transformable into each other via the so called Reidemeister moves have the same knot type. With the help of a properly constructed closure, I was able to apply a technique to identify the knotted conformations in the simulation. In contrast to knots found in the swollen and globular phase in former works, the knots found in this thesis are thermodynamically stable. Which means that in theses "knotted" pseudo-phases almost all conformations of the polymer are of one and the same knot type, thermal fluctuations does not change it. The pseudo-phase transition into these knotted conformation are very fascinating. Although neither the probability distribution nor the microcanonical analysis gives hint for a first-order-like phase transition, it is one. Employing the two-dimensional probability distribution one can observe two phases. In the two-dimensional probability distribution the non-knotted and the knotted pseudo-phase are clearly separated by two peaks. These peaks are located in the two-dimensional probability distribution in a way that they perfectly align in the projection to the total energy, and hence are not visible in the normal probability distribution. At the pseudo-phase transition the bending energy and the Lennard-Jones energy are transformed into each other without a change of the total energy. Therefore, no latent heat is observable.

Semiflexible Polymer inside a Sphere: The second part of this thesis was concerned with the influence of a spherical confinement on a semiflexible polymer.

For these investigations the coarse-grained model of the first part of this thesis is used. It is put into a spherical confinement with a fixed radius. The steric sphere is somewhat a first order approximation to a real obstacle the polymer is confined to. Real confinements would be much more complicated, however, the intention is to concentrate on the effects induced by the confinement itself. Using a flexible polymer the simulation shows that the collapse transition shifts to lower temperatures when lowering the radius of the spherical confinement. The shift increase with decreasing radius of the sphere until the difference of the globule and extended phase vanishes. Apart from that, all three phases observed for the free flexible polymer persists also inside the sphere. Of course, the typical elongation of the polymer in the extended phase depends on the sphere radius. The other two phases are barely influenced. The same is true for the temperature of the freezing transition, which shows no systematically dependence on the size of the sphere.

This gives rise to the question of why the effect is different for so many proteins compared to a flexible homopolymer. It has been shown that confined proteins are stabilized compared to their free counter-part. Of course, a simple polymer and a very complex protein differs in many ways. The results show that the stiffness could be one explanation. While the stiffness increases the strength of the shift lowers until for some κ, depending on the size of the polymer, the collapse transition temperature is barely influenced by the confinement. For even larger values of κ the effect goes into the opposite direction. The collapse transition temperature shifts to higher temperatures as soon as the polymer is enclosed in a sphere. This change of the effect is related to the order of transition. For low κ the collapse transition is of second-order kind. For higher values κ the collapse is a transition from an unstructured into a structured (bent) phase and of first-order kind. The two cases, the stabilizing and destabilizing, can be quantitatively explained by the same power-law. Only the sign of the scaling exponents differs.

Metropolis Monte Carlos Framework: The third part of this thesis gives an overview of the used Metropolis Monte Carlo algorithm and how they are tied into a framework for generic use. Beside modern standard techniques, e.g parallel tempering, or multicanonical sampling, the focus of the last chapter lies in extensions of these techniques.

The parallel multicanonical sampling (PMUCA) employs the architecture of modern high performance computer systems with its many CPU cores, by distributing the iteration process onto many cores. Although this technique cannot be parallelized onto an arbitrary amount of CPUs, it its possible to use several hundreds of them and reduce the wall-clock time from weeks down to several hours. In the same direction goes the two-dimensional replica-exchange method. By simulating replicas in parallel with different temperatures and stiffnesses, it is even possible to employ thousands of CPU cores. However, the key point of this technique is not the utilization of many CPU cores. The two-dimensional parameter space should help to overcome barriers which hinder the flow of the replicas if they would be constrained to one parameter dimension. In principle, the replica-exchange method can be extended to arbitrary dimensions and does not depend on the underlying simulation technique. Therefore, for a few simulations done in the first part of this thesis, the replica-exchange method was combined with PMUCA, which means several parallel PMUCA runs each running with a different value for κ and exchanging their states. The microcanonical analysis done for cross-checking the results are easier to obtain from multicanonical simulations.

All these algorithms are packed into one framework, which splits up the basic parts of a Metropolis Monte Carlo simulation in three building blocks: the physical system, the update moves, and the algorithm which propagates the system. To implement a new simulation these three basic building blocks can be combined, for example to treat the same problem with a different algorithm, alter the physical problem, or to change the move set. It is designed in a way, that by exchanging one part one do not have to touch the others.

While working on these topics, many new questions arised and could not be answered in this thesis. Simulating the bent and even more the knotted pseudo-phases turned out to be complicated and time-consuming. Even with the help of the two-dimensional replica-exchange algorithm or PMUCA the simulation of the longer polymers where quite complicated. With simpler simulation techniques it was even not possible to equilibrate the larger systems. Unfortunately, I had not the time to use a technique from which I now think it could solve the problem. A possible solution would be to run a replica-exchange in temperature combined with a multicanonical simulation which flattens the bending energy histogram instead of the histogram of the total energy. This technique is implemented within the framework, but was not well tested on larger system sizes. However, this is a technical question, from the physical point of view the observed knots maybe much more interesting.

First of all: could such knots be observed in real polymers? It is quite complicated to investigate such small structures of a free polymer within an experiment. But if one can show that the knots persists if the polymer is grafted onto a surface, it could be possible to investigate such structures via STM or similar techniques. However, first one have to find or design a candidate polymer which may form stable knots. From the theoretical point of view the phase separation of the knotting transition is exciting. A comparison of the surface tension of other first-order-like phase transition of the polymer could reveal conclusions about the stability of these knots. The knotted structure could be much more stable due to its topological nature.

Bibliography

[1] H. Abe and N. Gō.
Noninteracting local-structure model of folding and unfolding transition in globular proteins. II. Application to two-dimensional lattice proteins.
Biopolymers, 20(5):1013, 1981.

[2] J. W. Alexander.
Topological invariants of knots and links.
T. Am. Math. Soc., 30(2):275, 1928.

[3] J. W. Alexander and G. B. Briggs.
On types of knotted curves.
Ann. Math., 28(1/4):562, 1926.

[4] P. Arosio, T. CT Michaels, S. Linse, C. Månsson, C. Emanuelsson, J. Presto, J. Johansson, M. Vendruscolo, C. M. Dobson, and T. PJ Knowles.
Kinetic analysis reveals the diversity of microscopic mechanisms through which molecular chaperones suppress amyloid formation.
Nature Comm., 7, 2016.

[5] J. Arsuaga, M. Vazquez, P. McGuirk, S. Trigueros, J. Roca, et al.
DNA knots reveal a chiral organization of DNA in phage capsids.
PNAS, 102(26):9165, 2005.

[6] J. Arsuaga, M. Vázquez, S. Trigueros, J. Roca, et al.
Knotting probability of DNA molecules confined in restricted volumes: DNA knotting in phage capsids.
PNAS, 99(8):5373, 2002.

[7] A. Azari and K. K. Müller-Nedebock.
Entropic competition in polymeric systems under geometrical confinement.
Europhys. Lett., 110(6):68004, 2015.

[8] M. Bachmann, H. Arkın, and W. Janke.
Multicanonical study of coarse-grained off-lattice models for folding heteropolymers.
Phys. Rev. E, 71(3):031906, 2005.

[9] U. Bastolla and P. Grassberger.
Phase transitions of single semistiff polymer chains.
J. Stat. Phys., 89(5):1061, 1997.

[10] B. M. Baysal and F. E. Karasz.
Coil-Globule Collapse in Flexible Macromolecules.
Macromol. Theory Simul., 12(9):627, 2003.

[11] B. A. Berg and T. Neuhaus.
Multicanonical algorithms for first order phase transitions.
Phys. Lett. B, 267(2):249, 1991.

[12] B. A. Berg and T. Neuhaus.
Multicanonical ensemble: A new approach to simulate first-order phase transitions.
Phys. Rev. Lett., 68(1):9, 1992.

[13] H. M. Berman, J. Westbrook, Z. Feng, G. Gilliland, T. N. Bhat, H. Weissig, Ilya N. Shindyalov, and Philip E. Bourne.
The Protein Data Bank.
Nucleic Acids Res., 28(1):235, 2000.

[14] E. Bittner, A. Nußbaumer, and W. Janke.
Make life simple: Unleash the full power of the parallel tempering algorithm.
Phys. Rev. Lett., 101(13):130603, 2008.

[15] C. Borgs and W. Janke.
An explicit formula for the interface tension of the 2D Potts model.
J. Phys. I, 2(11):2011, 1992.

[16] C. Borgs and W. Janke.
New method to determine first-order transition points from finite-size data.
Phys. Rev. Lett., 68(11):1738, 1992.

[17] D. Bouzida, S. Kumar, and R. H. Swendsen.
Efficient Monte Carlo methods for the computer simulation of biological molecules.
Phys. Rev. A, 45(12):8894, 1992.

[18] C. G. Broyden.
A class of methods for solving nonlinear simultaneous equations.
Math. Comp., 19(92):577, 1965.

[19] A. Cacciuto and E. Luijten.
Self-avoiding flexible polymers under spherical confinement.
Nano Letters, 6(5):901, 2006.

[20] Q. Cao and M. Bachmann.
Dynamics and Limitations of spontaneous Polyelectrolyte Intrusion into a charged Nanocavity.
Phys. Rev. E, 90(6):060601, 2014.

[21] Q. Cao and M. Bachmann.
Impact of surface charge density and motor force upon polyelectrolyte packaging in viral capsids.
J. Polym. Sci. Pol. Phys., 54(11):1054, 2016.

[22] A. Daanoun, C. F. Tejero, and M. Baus.
Van der Waals theory for solids.
Phys. Rev. E, 50(4):2913, 1994.

[23] P.-G. de Gennes.
Scaling concepts in polymer physics.
Cornell university press, 1979.

[24] T. Deguchi and K. Tsurusaki.
Universality of random knotting.
Phys. Rev. E, 55:6245, 1997.

[25] S. Doniach, T. Garel, and H. Orland.
Phase diagram of a semiflexible polymer chain in a θ solvent: Application to protein folding.
J. Chem. Phys., 105(4):1601, 1996.

[26] B. Efron and C. Stein.
The jackknife estimate of variance.
The Annals of Statistics, 9(3):586, 1981.

[27] M. K. Fenwick.
A direct multiple histogram reweighting method for optimal computation of the density of states.
J. Chem. Phys., 129(12):125106, 2008.

[28] A. M. Ferrenberg and R. H. Swendsen.
New Monte Carlo technique for studying phase transitions.
Phys. Rev. Lett., 61(December):2635, 1988.

[29] A. M. Ferrenberg and R. H. Swendsen.
Optimized Monte Carlo Data Analysis.
Phys. Rev. Lett., 63(12):1195, 1989.

[30] P. J. Flory.
Principles of polymer chemistry.
Cornell University Press, 1953.

[31] C. Forrey and M. Muthukumar.
Langevin dynamics simulations of genome packing in bacteriophage.
Biophys. J., 91(1):25, 2006.

[32] S. Förster, E. Kohl, M. Ivanov, J. Gross, W. Widdra, and W. Janke.
Polymer adsorption on reconstructed Au(001): A statistical description of P3HT by scanning tunneling microscopy and coarse-grained Monte Carlo simulations.
J. Chem. Phys., 141(16):164701, 2014.

[33] S. Förster and W. Widdra.
Structure of single polythiophene molecules on Au(001) prepared by in situ UHV electrospray deposition.
J. Chem. Phys., 141(5):054713, 2014.

[34] M. D. Frank-Kamenetskii, A. V. Lukashin, and A. V. Vologodskii.
Statistical mechanics and topology of polymer chains.
Nature, 258:398, 1975.

[35] M. Friedel, D. J. Sheeler, and J.-E. Shea.
Effects of confinement and crowding on the thermodynamics and kinetics of folding of a minimalist β-barrel protein.
J. Chem. Phys., 118(17):8106, 2003.

[36] C. J. Geyer.
Markov chain Monte Carlo maximum likelihood.
Comput. Sci. Stat. Proc. 23rd Symp. Interface, page 156, 1991.

[37] N. Gō and H. Abe.
Noninteracting local-structure model of folding and unfolding transition in globular proteins. I. Formulation.
Biopolymers, 20(5):991, 1981.

[38] P. Grassberger and R. Hegger.
Simulations of three-dimensional θ polymers.
J. Chem Phys., 102(17):6881, 1995.

[39] D. H. E. Gross.
Microcanonical Thermodynamics: Phase transitions in "small" systems.
World Scientific, Singapore, 2001.

[40] B.-Y. Ha and Y. Jung.
Polymers under confinement: single polymers, how they interact, and as model chromosomes.
Soft Matter, 11(12):2333, 2015.

[41] F. U. Hartl, A. Bracher, and M. Hayer-Hartl.
Molecular chaperones in protein folding and proteostasis.
Nature, 475(7356):324, 2011.

[42] F. U. Hartl and M. Hayer-Hartl.
Molecular chaperones in the cytosol: from nascent chain to folded protein.
Science, 295(5561):1852, 2002.

[43] W. K. Hastings.
Monte Carlo sampling methods using Markov chains and their applications.
Biometrika, 57(1):97, 1970.

[44] T. X. Hoang, A. Giacometti, R. Podgornik, N. T. T. Nguyen, J. R. Banavar, and A. Maritan.
From toroidal to rod-like condensates of semiflexible polymers.
J. Chem. Phys., 140(6):064902, 2014.

[45] H.-P. Hsu and P. Grassberger.
The coil–globule transition of confined polymers.
J. Stat. Mech. Theor. Exp., 2005(01):P01007, 2005.

[46] H.-P. Hsu, V. Mehra, and P. Grassberger.
Structure optimization in an off-lattice protein model.
Phys. Rev. E., 68(3):037703, 2003.

[47] H.-P. Hsu, W. Paul, and K. Binder.
Polymer chain stiffness versus excluded volume: A Monte Carlo study of the crossover towards the wormlike chain model.
Europhys. Lett., 92:28003, 2010.

[48] Y. Hu, R. Zandi, A. Anavitarte, C. M Knobler, and W. M. Gelbart.
Packaging of a polymer by a viral capsid: the interplay between polymer length and capsid size.
Biophys. J., 94(4):1428, 2008.

[49] K. Hukushima and K Nemoto.
Exchange Monte Carlo method and application to spin glass simulations.
J. Phys. Soc. Japan, 65(6):1604, 1996.

[50] A. Irbäck, C. Peterson, F. Potthast, and O. Sommelius.
Local interactions and protein folding: A three-dimensional off-lattice approach.
J. Chem. Phys., 107(1):273, 1997.

[51] V. A. Ivanov, J. A. Martemyanova, M. Müller, W. Paul, and K. Binder.
Conformational changes of a single semiflexible macromolecule near an adsorbing surface: A Monte Carlo simulation.
J. Phys. Chem. B, 113(12):3653, 2009.

[52] M. Jamroz, W. Niemyska, E. J.w Rawdon, A. Stasiak, K. C. Millett, P. Sułkowski, and J. I. Sulkowska.

KnotProt: a database of proteins with knots and slipknots.
Nucleic Acids Res., 43:D306, 2014.

[53] W. Janke.
Multicanonical Monte Carlo simulations.
Physica A, 254(1-2):164, 1998.

[54] S. Jun and B. Mulder.
Entropy-driven spatial organization of highly confined polymers: lessons for the bacterial chromosome.
PNAS, 103(33):12388, 2006.

[55] C. Junghans, M. Bachmann, and W. Janke.
Microcanonical analyses of peptide aggregation processes.
Phys. Rew. Lett., 97(21):218103, 2006.

[56] C. Junghans, M. Bachmann, and Janke W.
Thermodynamics of peptide aggregation processes: An analysis from perspectives of three statistical ensembles.
J. Chem. Phys., 128(8):085103, 2008.

[57] N. Ch. Karayiannis, V. G. Mavrantzas, and D. N. Theodorou.
A novel Monte Carlo scheme for the rapid equilibration of atomistic model polymer systems of precisely defined molecular architecture.
Phys. Rev. Lett., 88(10):105503, 2002.

[58] H. G. Katzgraber, S. Trebst, D. A. Huse, and M. Troyer.
Feedback-optimized parallel tempering Monte Carlo.
J. Stat. Mech. Theor. Exp., 2006(03):P03018, 2006.

[59] L. H. Kauffman.
Knots and Physics, Third Edition.
World Scientific, 2001.

[60] B. Kaufman.
Crystal statistics. II. Partition function evaluated by spinor analysis.
Phys. Rev., 76(8):1232, 1949.

[61] E.-G. Kim and M. L. Klein.
Unknotting of a polymer strand in a melt.
Macromolecules, 37(5):1674, 2004.

[62] D. K. Klimov, D. Newfield, and D. Thirumalai.
Simulations of β-hairpin folding confined to spherical pores using distributed computing.
PNAS, 99(12):8019, 2002.

[63] K. Koniaris and M. Muthukumar.
Knottedness in ring polymers.
Phys. Rev. Lett., 66(17):2211, 1991.

[64] K. Koniaris and M. Muthukumar.
Self-entanglement in ring polymers.
J. Chem Phys., 95(4):2873, 1991.

[65] O. Kratky and G. Porod.
Röntgenuntersuchung gelöster fadenmoleküle.
Recl. Trav. Chim. Pays-Bas, 68(12):1106, 1949.

[66] S. Kumar, J. M. Rosenberg, D. Bouzida, R. H. Swendsen, and P. A. Kollman.
The weighted histogram analysis method for free-energy calculations on biomolecules. I. The method.
J. Comp. Chem., 13(8):1011, 1992.

[67] R. Lua, A. L. Borovinskiy, and A. Y. Grosberg.
Fractal and statistical properties of large compact polymers: a computational study.
Polymer, 45(2):717, 2004.

[68] R. C. Lua and A. Y. Grosberg.
Statistics of knots, geometry of conformations, and evolution of proteins.
PLoS Comput. Biol., 2(5):e45, 2006.

[69] D. Lucent, V. Vishal, and V. S. Pande.
Protein folding under confinement: a role for solvent.
PNAS, 104(25):10430, 2007.

[70] M. L. Mansfield.
Monte Carlo studies of polymer chain dimensions in the melt.
J. Chem. Phys., 77(3):1554, 1982.

[71] M. L. Mansfield.
Are there knots in proteins?
Nat. Struct. Biol., 1(4):213, 1994.

[72] M. Marenz and W. Janke.
Knots as a topological order parameter for semiflexible polymers.
Phys. Rev. Lett., 116(12):128301, 2016.

[73] M. Marenz, J. Zierenberg, and W. Janke.
Simple flexible polymers in a spherical cage.
Condens. Matter Phys., 15(4):43008, 2012.

[74] A Maritan, C. Micheletti, A. Trovato, and J. R. Banavar.
Optimal shapes of compact strings.
Nature, 406(6793):287, 2000.

[75] N. Metropolis, A. W. Rosenbluth, M. N. Rosenbluth, A. H. Teller, and E. Teller.
Equation of State Calculations by Fast Computing Machines.
J. Chem. Phys., 21(6):1087, 1953.

[76] J. Mittal and R. B. Best.
Thermodynamics and kinetics of protein folding under confinement.
Proc. Natl. Acad. Sci., 105(51):20233, 2008.

[77] M. Mueller, W. Janke, and D. A. Johnston.
Nonstandard Finite-Size Scaling at First-Order Phase Transitions.
Phys. Rev. Lett., 112(20):200601, 2014.

[78] M. Muthukumar.
Mechanism of DNA transport through pores.
Annu. Rev. Biophys. Biomol. Struct., 36:435, 2007.

[79] H. Noguchi and K. Yoshikawa.
First-order phase transition in a stiff polymer chain.
Chem. Phys. Lett., 278:184, 1997.

[80] Theo Odijk.
Scaling theory of DNA confined in nanochannels and nanoslits.
Phys. Rev. E, 77(6):060901, 2008.

[81] P. V. K. Pant and D. N. Theodorou.
Variable connectivity method for the atomistic Monte Carlo simulation of polydisperse polymer melts.
Macromolecules, 28(21):7224, 1995.

[82] D. F. Parsons and D. R. M. Williams.
An off-lattice Wang-Landau study of the coil-globule and melting transitions of a flexible homopolymer.
J. Chem. Phys., 124(22):221103, 2006.

[83] S. Plimpton.
Fast parallel algorithms for short-range molecular dynamics.
J. Chem. Phys., 117(1):1, 1995.

[84] S. Pronk, S. Páll, R. Schulz, P. Larsson, P. Bjelkmar, R. Apostolov, M. R. Shirts, J. C. Smith, P. M. Kasson, D. van der Spoel, B. Hess, and E. Lindahl.
GROMACS 4.5: a high-throughput and highly parallel open source molecular simulation toolkit.
Bioinformatics, 29(7):845, 2013.

[85] F. Rampf, W. Paul, and K. Binder.
On the first-order collapse transition of a three-dimensional, flexible homopolymer chain model.
Europhys. Lett., 70(5):628, 2007.

[86] N. Rathore, T. A. Knotts, and J. J. de Pablo.
Confinement effects on the thermodynamics of protein folding: Monte Carlo simulations.
Biophys. J., 90(5):1767, 2006.

[87] D. Reith, P. Cifra, A. Stasiak, and P. Virnau.
Effective stiffening of DNA due to nematic ordering causes DNA molecules packed in phage capsids to preferentially form torus knots.
Nucleic Acids Rec., 40(11):5129, 2012.

[88] M. Rubinstein and R. H. Colby.
Polymer Physics.
Oxford University Press, Oxford, 2003.

[89] A. M. Saitta, P. D. Soper, E. Wasserman, and M. L. Klein.
Influence of a knot on the strength of a polymer strand.
Nature, 399(6731):46, 1999.

[90] T. Sakaue.
Semiflexible polymer confined in closed spaces.
Macromolecules, 40(14):5206, 2007.

[91] T. Sakaue and E. Raphael.
Polymer chains in confined spaces and flow-injection problems: some remarks.
Macromolecules, 3(2):2621, 2006.

[92] Z. W. Salzburg, J. D. Jacobson, W. Fickett, and W. W. Wood.
Application of the Monte Carlo method to the lattice-gas model.
J. Chem. Phys., 30:65, 1959.

[93] S. Schnabel, M. Bachmann, and W. Janke.
Elastic Lennard-Jones polymers meet clusters: differences and similarities.
J. Chem. Phys., 131(12):124904, 2009.

[94] S. Schnabel, W. Janke, and M. Bachmann.
Simulating the all-order strong coupling expansion I: Ising model demo.
J. Comput. Phys., 810(3):491, 2009.

[95] S. Schnabel, D. T. Seaton, D. P. Landau, and M. Bachmann.
Microcanonical entropy inflection points: Key to systematic understanding of transitions in finite systems.
Phys. Rev. E, 84(1):011127, 2011.

[96] S. Schnabel, T. Vogel, M. Bachmann, and W. Janke.
Surface effects in the crystallization process of elastic flexible polymers.
Chem. Phys. Lett., 476(4-6):201, 2009.

[97] D. T. Seaton, S. Schnabel, D. P. Landau, and M. Bachmann.
From Flexible to Stiff: Systematic Analysis of Structural Phases for Single Semiflexible Polymers.
Phys. Rev. Lett., 110(2):028103, 2013.

[98] D. T. Seaton, T. Wüst, and D. P. Landau.
A Wang-Landau study of the phase transitions in a flexible homopolymer.
Comput. Phys. Commun., 180(4):587, 2009.

[99] D. T. Seaton, T. Wüst, and D. P. Landau.
Collapse transitions in a flexible homopolymer chain: Application of the Wang-Landau algorithm.
Phys. Rev. E, 81(1):011802, 2010.

[100] H. Staudinger.
Über polymerisation.
Eur. J. Inorg. Chem., 53(6):1073, 1920.

[101] F. H. Stillinger and T. Head-Gordon.
Collective aspects of protein folding illustrated by a toy model.
Phys. Rev. E, 52(3):2872, 1995.

[102] F. H. Stillinger, T. Head-Gordon, and C. L. Hirshfeld.
Toy model for protein folding.
Phys. Rev. E, 48(2):1469, 1993.

[103] Y. Sugita, A. Kitao, and Y. Okamoto.
Multidimensional replica-exchange method for free-energy calculations.
J. Chem. Phys., 113(15):6042, 2000.

[104] Baeckkyoung Sung, Amélie Leforestier, and Françoise Livolant.
Coexistence of coil and globule domains within a single confined DNA chain.
Nucleic Acids Res., 44(3):1421, 2016.

[105] R. H. Swendsen and J.-S. Wang.
Replica Monte Carlo simulation of spin-glasses.
Phys. Rev. Lett., 57(21):2607, 1986.

[106] F. Takagi, N. Koga, and S. Takada.
How protein thermodynamics and folding mechanisms are altered by the chaperonin cage: molecular simulations.
PNAS, 100(20):11367, 2003.

[107] M. P. Taylor, W. Paul, and K. Binder.
All-or-none proteinlike folding transition of a flexible homopolymer chain.
Phys. Rev. E, 79(5):050801, 2009.

[108] W. R. Taylor.
A deeply knotted protein structure and how it might fold.
Nature, 406(6798):916, 2000.

[109] B. Trefz, J. Siebert, and P. Virnau.
How molecular knots can pass through each other.
PNAS, 111(22):7948, 2014.

[110] P. Virnau.
Detection and visualization of physical knots in macromolecules.
Phys. Procedia, 6:117, 2010.

[111] P. Virnau, Y. Kantor, and M. Kardar.
Knots in globule and coil phases of a model polyethylene.
J. Am. Chem. Soc., 127(43):15102, 2005.

[112] P. Virnau, L. A. Mirny, and .. Kardar.
Intricate Knots in Proteins: Function and Evolution.
PLoS Comput. Biol., 2(9):1–6, 09 2006.

[113] T. Vogel, M. Bachmann, and W. Janke.
Freezing and collapse of flexible polymers on regular lattices in three dimensions.
Phys. Rev. E, 76(6):061803, 2007.

[114] T. Vogel, T. Neuhaus, M. Bachmann, and W. Janke.
Ground-state properties of tubelike flexible polymers.
Eur. Phys. J. E, 30(1):7, 2009.

[115] T. Vogel, T. Neuhaus, M. Bachmann, and W. Janke.
Thickness-dependent secondary structure formation of tubelike polymers.
Europhys. Lett., 85:10003, 2009.

[116] F. Wang and D. P. Landau.
Efficient, multiple-range random walk algorithm to calculate the density of states.
Phys. Rev. Lett., 86(10):2050, 2001.

[117] J.-S. Wang and R. H. Swendsen.
Replica Monte Carlo Simulation (Revisited).
Prog. Theor. Phys. Suppl., 157(157):317, 2005.

[118] U. Wolff.
Comparison between cluster Monte Carlo algorithms in the Ising model.
Phys. Lett. B, 228(3):379, 1989.

[119] T. Wüst, D. Reith, and P. Virnau.
Sequence Determines Degree of Knottedness in a Coarse-Grained Protein Model.
Phys. Rev. Lett., 114(2):028102, 2015.

[120] J. C. Young, V. R. Agashe, K. Siegers, and F. U. Hartl.
Pathways of chaperone-mediated protein folding in the cytosol.
Nat. Rev. Mol. Cell Bio., 5(10):781, 2004.

[121] H.-X. Zhou and K. A. Dill.
New Concepts Stabilization of Proteins in Confined Spaces.
Biochemistry, 40(38):1, 2001.

[122] J. Zierenberg and W. Janke.
From amorphous aggregates to polymer bundles: The role of stiffness on structural phases in polymer aggregation.
Europhys. Lett., 109(2):28002, 2015.

[123] J. Zierenberg, M. Marenz, and W. Janke.
Scaling properties of a parallel implementation of the multicanonical algorithm.
Comput. Phys. Commun., 184(4):1155, 2013.

[124] J. Zierenberg, M. Marenz, and W. Janke.
Scaling properties of parallelized multicanonical simulations.
Phys. Proc., (53):55, 2014.

[125] J. Zierenberg, M. Marenz, and W. Janke.
Dilute Semiflexible Polymers with Attraction: Collapse, Folding and Aggregation.
Polymers, 8(9):333, 2016.

[126] J. Zierenberg, M. Mueller, P. Schierz, M. Marenz, and W. Janke.
Aggregation of theta-polymers in spherical confinement.
J. Chem. Phys., 141(11):114908, 2014.

Danksagung

Ich möchte mich zu vorerst bei meinem betreuenden Professor Wolfhard Janke für die Unterstützung bei der Durchführung und Fertigstellung meiner Dissertation bedanken, für die stetigen Anregungen, Ideen und die zahlreichen Diskussionen rund um alle Bereiche meiner Dissertation und darüber hinaus. Für die fruchtbaren Diskussionen und die kollegiale Stimmung möchte ich mich bei meinen Kollegen aus dem ITP Martin Treffkorn, Philipp Schierz, Stefan Schnabel, Hanes Nagel und Marco Müller bedanken. Bei Hannes Nagel möchte ich mich daneben auch für die Zusammenarbeit bei der Administration der Rechner und Computecluster des ITPs bedanken, in der Zeit im ITP haben wir beide sicherlich viel voneinander gelernt. Besonderen Dank gilt auch Niklas Fricke mit dem ich im ITP ein Bürozimmer geteilt habe, insbesondere für die Hilfe bei der Indentifizierung von Knoten mit allen zur Verfügung stehenden Hilfsmitteln. Auf fachlicher Ebene habe ich sicherlich Johannes Zierenberg am meißten zu Danken, für viele Diskussion, den unentwegten Versuch die auftretenden Probleme physikalisch zu verstehen und den Antrieb meine Dissertation zu beenden. Mit ihm zusammen habe ich den Großteil der Algorithmen entwickelt, oder zumindestens tiefgreifend diskutiert und ein Verständniss für diese entwickelt. Den allergrößten Dank gebührt allerdings meiner Frau, ohne deren Unterstützung ich diese Arbeit nicht hätte fertigstellen können, für die großzügige Geduld und die Fürsorge unserer Kinder an Abenden an denen ich meine Dissertation geschrieben habe.

Academic Curriculum Vitae

Personal Details:

Name	Martin Marenz
Date of birth	August 05, 1984
Nationality	German

Education:

09/1997 - 06/2004	Gymnasium Bertolt Brecht, Bard Freienwalde, *Abitur*
10/2005 - 12/2010	Diploma Physics, Unitversiät Leipzig
04/2011 - 03/2016	Ph.D. thesis in Theoretical Physics, Universität Leipzig within the Graduate School “BuildMoNa”
10/2011-10/2014	Research stays at Coventry University, England (2 weeks total) and Nancy Université, France (2 weeks total)

Publications:

- M. Marenz, J. Zierenberg, H. Arkın, and W. Janke, *Simple Flexible Polymers in a Spherical Cage*, Condens. Matter Phys. **15**, 43008 (2012).

- J. Zierenberg, M. Marenz, and W. Janke, *Scaling Properties of a Parallel Implementation of the Multicanonical Algorithm*, Comput. Phys. Comm. **184**, 1155 (2013).

- J. Zierenberg, M. Marenz, and W. Janke, *Scaling Properties of Parallelized Multicanonical Simulations*, in: *Computer Simulation Studies in Condensed-Matter Physics XXVI*, eds. D.P. Landau, M. Backmann, S.P. Lewis, and H.-B. Schüttler, Physics Procedia **53**, 55 (2014)

- M. Marenz and W. Janke, *Effect of Bending Stiffness on a Homopolymer Inside a Spherical Cage*, in: *Computer Simulation Studies in Condensed-Matter Physics XXVI*, eds. D.P. Landau, M. Backmann, S.P. Lewis, and H.-B. Schüttler, Physics Procedia **57**, 53, (2014)

- J. Zierenberg, M. Mueller, P. Schierz, M.Marenz, and W. Janke, *Aggregation of Theta-Polymers in Spherical Confinement*, J. Chem. Phys. **141**, 114908 (2014)

- M. Mueller, J. Zierenberg, M. Marenz, P. Schierz, and W. Janke, *Probing the Effect of Density on the Aggregation Temperature of Semi-Flexible Polymers in Spherical Confinement*, in: *Computer Simulation Studies in Condensed-Matter Physics XXVIII*, eds. D.P. Landau, H.-B. Schüttler, S. Lewis, and M. Bachmann, Physics Procedia **68**, 95 (2015.

- M. Marenz and W. Janke, *Knots as a Topological Order Parameter of Semiflexible Polymers*, Phys. Rev. Lett. **116**, 128301 (2016)

- W. Janke and M. Marenz, *Stable Knots in the Phase DIagram of Semiflexible Polymers: A Topological Order Parameter?*, in: *Computer Simulation Studies in Condensed-Matter Physics XXVIII*, eds. D.P. Landau, M. Backmann, S.P. Lewis, and H.-B. Schüttler, J. Phys.: Conf. Ser. **750**, 012006 (2016)

- J. Zierenberg, M. Marenz, and W. Janke, *Dilute Semiflexible Polymers with Attraction: Collapse, Folding and Aggregation (invited review)*, Polymers **8**, 33 (2016)

- N. Fricke, J. Zierenberg, M. Marenz, F.P. Spitzner, V. Blavatska, and W. Janke, *Scaling Laws of Random Walks in Long-Range Correlated Disorder Media*, Condens. Matter Phys. **20**, 13004 (2017)

- J. Zierenberg, N. Fricke, M. Marenz, F.P. Spitzner, V. Blavatska, and W. Janke, *Percolation Thresholds and Fractal Dimensions for Square and Cubic Lattices with Long-Range Correlated Defects*, Göttingen/Leipzig/Lviv preprint (August 2017), arXiv:1708.02296 (cond-mat.stat-mech).

Bibliographische Beschreibung:

Marenz, Martin

Morphologies of Semiflexible Polymers on Bulk and Spherical Confinement

Universität Leipzig, Dissertation
121 S., 126 Lit., 59 Abb., 3 Tabellen

Referat:

Diese Dissertation befasst sich mit dem Verhalten eines generischen semiflexiblen Polymermodells. Insbesondere untersucht es den Einfluss von Steifigkeit auf die unterschiedlichen thermodynamisch stabilen Konformationen. Es wird erläutert wie durch die Steifigkeit des Polymers verschiedene strukturierte Phasen induziert werden. Insbesondere wird dabei auf die stabilen verknoteten Phasen eingegangen. Der zweite Teil der Dissertation beschäftigt sich dann mit dem Einfluss einer kugelförmigen Einsperrung auf das Phasendiagramm des selben Polymermodells. Es wird gezeigt wie in Abhängigkeit der Ordnung des Phasenüberganges die Einsperrung entweder zu einem stabilisierenden oder destabilisierenden Effekt führt. Im dritten Teil der Dissertation werden dann die komplexen Monte-Carlo Simulationen erläutert die für die Simulation der physikalischen Systeme genutzt wurde. Diese Algorithmen wurden in ein Framework integriert, so dass diese wieder verwendet werden können.